5-2012

Using Stereo Particle Image Velocimetry to Quantify and Optimize Mixing in an Algae Raceway Using Delta Wings

Blake W. Lance
Utah State University

USING STEREO PARTICLE IMAGE VELOCIMETRY TO QUANTIFY AND OPTIMIZE MIXING IN AN ALGAE RACEWAY USING DELTA WINGS

by

Blake W. Lance

A thesis submitted in partial fulfillment
of the requirements for the degree

of

MASTER OF SCIENCE

in

Mechanical Engineering

Approved:

Dr. Byard Wood Co-Major Professor	Dr. Barton L. Smith Co-Major Professor
Dr. Heng Ban Committee Member	Dr. Mark R. McLellan Vice President for Research and Dean of the School of Graduate Studies

UTAH STATE UNIVERSITY
Logan, Utah

2012

Abstract

Using Stereo Particle Image Velocimetry to Quantify and Optimize Mixing in an Algae Raceway Using Delta Wings

by

Blake W. Lance, Master of Science

Utah State University, 2012

Co-Major Professor: Dr. Byard Wood
Co-Major Professor: Dr. Barton L. Smith
Department: Mechanical and Aerospace Engineering

Of the potential feedstocks for biofuels, microalgae is the most promising, and raceway ponds are the most cost-effective method for growing mircoalgal biomass. Nevertheless, biofuel production from algae must be more efficient to be competitive with traditional fuels. Previous studies using arrays of airfoils, triangles, and squares at high angles of attack show an increase in mixing in raceways and can improve productivity by up to a factor of 2.2. Some researchers say increasing mixing increases growth due to the flashing light effect while others claim it is the decrease in the fluid boundary layer of the cells that increases mass transfer. Whatever the reason, increasing growth by increasing mixing is a repeatable effect that is desirable to both reduce operation costs and increase production.

An experimental raceway is constructed to test the effect of a delta wing (DW) on raceway hydraulics in the laboratory using fresh-water. The DW is an isosceles triangle made of plate material that is placed at a high angle of attack in the circulating raceway flow. Results from this investigation can be scaled to larger growth facilities use arrays of DWs. Two vortices are found downstream of the DW when used in this way and create significant vertical fluid circulation. Stereo particle image velocimetry (PIV) is used to

quantify and optimize the use of delta wings as a means to increase fluid mixing. Stereo PIV gives three components of velocity in a measurement plane at an instant. Three studies are performed to determine the optimal paddle-wheel speed, angle of attack, and DW spacing in the raceway based on mixing. Two new mixing quantities are defined. The first is the Vertical Mixing Index (VMI) that is based on the vertical velocity magnitude, and the second is the Cycle Time required for an algal cell to complete a cycle from the bottom to the top and back again in the raceway.

The power required to circulate the flow is considered in all results. The Paddle-wheel Speed Study shows that the VMI is not a function of streamwise velocity, which makes it very useful for comparison. The Cycle Time decreases quickly with streamwise velocity then levels out, revealing a practical speed for operation that is lower than typically used and consumes only half the power. The angle of 40° is optimal from the results of the Angle of Attack Study for both VMI and Cycle Time. The third study is the Vortex Dissipation Study and is used to measure the distance downstream before the vortices dissipate. This information is used to optimize the DW spacing for profit considering the additional costs of adding DWs.

(118 pages)

Public Abstract

Using Stereo Particle Image Velocimetry to Quantify and Optimize Mixing in an Algae Raceway Using Delta Wings

by

Blake W. Lance, Master of Science

Utah State University, 2012

Co-Major Professor: Dr. Byard Wood
Co-Major Professor: Dr. Barton L. Smith
Department: Mechanical and Aerospace Engineering

Biofuel research has been continually growing over the past six decades. Of the potential sources for biofuels, microalgae is the most promising, and circulating (raceway) ponds are the most cost-effective method for growing microalgae in abundance. Nevertheless, biofuel production from algae must be more efficient to be competitive with traditional fuels. Previous studies using several airfoils, triangles, and squares at high angles to the flow direction (angle of attack) show an increase in mixing in raceways and can improve productivity by up to a factor of 2.2. Researchers show that increasing growth by increasing mixing is a repeatable effect that is desirable to both reduce operation costs and increase production.

An experimental raceway of similar shape to commercial facilities is constructed to test the effect of a delta wing (DW) on fluid motion in the laboratory using fresh-water. The DW is a triangle made of plate material that is placed in the circulating flow creating significant fluid circulation. Results from this investigation can be scaled to larger growth facilities use arrays of DWs. Stereo particle image velocimetry (PIV) is used to measure and optimize the use of DWs as a means to increase fluid mixing. Three studies are performed to determine

the best fluid speed, angle of attack, and DW spacing in the raceway based on mixing. Two new mixing quantities are defined to reduce results for optimization. These studies result in the optimal use of DWs in raceway ponds to increase mixing and are expected to increase growth.

Acknowledgments

This work would not have been possible without the help of many. Dr. Wood was the guiding influence and the instigator in the work. Dr. Smith was always willing to answer questions about measurement techniques, data analysis, and writing. Dr. Cripps guided the power measurement. My family has been very supportive, especially my wife for taking good care of our son the many evenings and weekends I was in the lab.

The USU BioEnergy Center and the US Department of Energy (Grant Number DE-EE0003114) deserve thanks for their financial and facility support. I am very grateful for Ram Voleti and Jayson Pemberton who designed and built the experimental raceway and for having the forethought to have transparent sides for optical access. Ram and Aaron Godfrey gave me the background I needed to start in this new and unfamiliar area of research. Justin Hunt provided time-saving mounting structures for the PIV system that saved significant amounts of time.

Blake W. Lance

Contents

List of Tables

List of Figures

Acronyms

ADV	acoustic doppler velocimeter
CCD	charge-coupled device
CFD	computational fluid dynamics
DAQ	data acquisition device
DW	delta wing
FLE	flashing light effect
Nd-YAG	neodymium-doped yttrium aluminum garnet
PIV	particle image velocimetry
RMS	root mean square
SD	standard deviation
TKE	turbulence kinetic energy
VFD	variable frequency drive
VMI	vertical mixing index

Chapter 1

Introduction

1.1 Background

Research on microalgal-based biofuels began around 1960, but little was invested until the 1970s. This research has grown recently as crude oil prices, energy demand, and concern about environmental issues have all increased [1]. Of the types of feedstock for biofuels, microalgae has shown exceptional production rates for land use. To replace half of the transport fuel in the United States with biodiesel, microalgae would need to be grown on 1-3% of the existing cropping area compared to the 846% of land required if corn were to be used [2]. Despite the superior growth rates, Batan *et al.* [3] found microalgal biodiesel requires 93% of the reclaimed energy for production compared to 19% for conventional diesel. They also found that biodiesel has one significant advantage: its growth consumes significant amounts of greenhouse gas whereas conventional fuels produce it.

Algae grow best when exposed to sunlight intensities that are only a portion of the maximum intensity incident at the earth's surface. In fact, it has been shown that growth rates decrease when exposed to high intensities in a phenomenon termed *photoinhibition*. One proposed solution for increased biomass production is to periodically shade the algae once they have been exposed to high levels of light intensity [4]. One proposed method is to increase the depth of raceway ponds and ensure that the algal culture is turned-over so the cells are exposed to light then experience a period of shading.

The two common types of algal growth facilities are open raceway ponds and photobioreactors. Raceway ponds have been used since the 1950s and are circulating channels open to the atmosphere, typically around 0.3 m deep, that are built from concrete or compacted earth and circulated by a paddlewheel as seen in Fig. 1.1. Photobioreactors are a newer concept that use closed tubes or varying shape with a two-phase mixture that are

pumped in the circulation path or sparged with CO_2 [2]. An example of one of the several types of photobioreactors is shown in Fig. 1.2. Photobioreactors produce biomass at much higher concentrations using less land, but these advantages come with higher cost. In 2011 Davis *et al.* found that production-scale biodiesel cost from a raceway is \$9.84/gal while that from photobioreactors is \$20.53/gal [5].

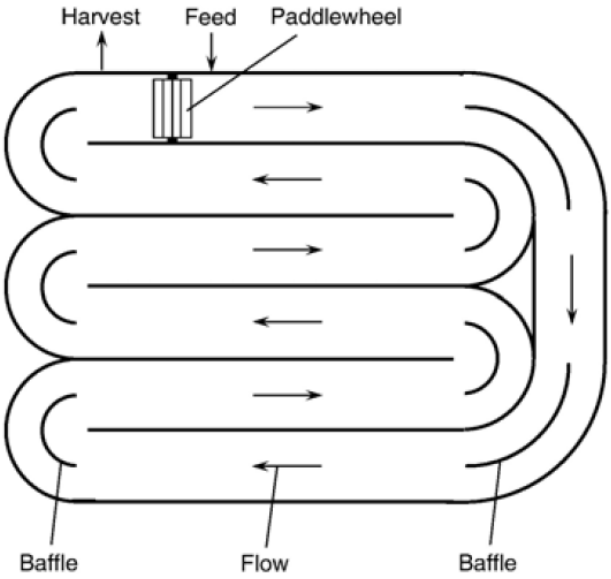

Fig. 1.1: Sketch of an open raceway pond. Figure from [2] and used with permission.

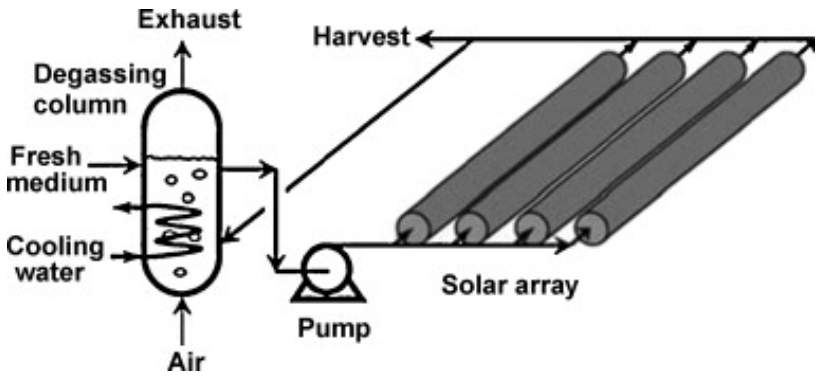

Fig. 1.2: An example of a Photobioreactor. Figure from [6] and used with permission.

1.2 Literature Review

Flashing Light Effect (FLE) is a term that describes exposing cells to alternating periods of light and dark and has been shown to increase photosynthetic efficiency of algal growth [7]. Mixing the algal growth culture is one method of introducing the FLE because the light attenuation decays exponentially in algal cultures by what is commonly called the Beer-Lambert Law [8]. Therefore the light penetration depths are typically between $1-2$ inches. After completing an experimental study on the effect of the FLE on growth rates of the common algal strain Chlorella, Phillips and Myers [9] stated in 1954,

> A dense culture growing under sunlight will experience a significant increase in growth if cells are moved in and out of the high intensity of the front surface at such a rate as to give flash times between 0.001 and 0.1 second. It is also clear that the culture should be thick enough or dense enough so that almost all the light will be absorbed in the first 10% and the dark time will be about ten times as long as the light flash. These considerations lead to the conclusion that almost any attempt to grow algae in sunlight will experience some gain by turbulence. The feasibility of increasing the turbulence will depend upon the extent of the gain in growth as compared to the increased power requirement of stirring or pumping the suspension. (p. 160)

This quote is a practical conclusion to a comprehensive work and motivates facilities with high mixing levels if high algal density is used for increased growth rates. The research of others shows that optimal flashing periods are between 0.1-10 s, but they do not distinguish between flashing time and dark time [10].

Miller *et al.* studied the effect of mixing on the efficiency of algal photosynthesis [11]. Algae were grown in an annulus with a rotating inner cylinder. Taylor vortices in the annulus caused a regular mixing pattern for the algal culture. They found that FLE, not increased mass transfer, is the dominant enhancer of algal growth where regular mixing is found. They concluded "Utilization of the flashing light effect for improvement of photosynthetic efficiency of optically dense algal cultures requires a nonrandom mixing pattern–one in which cells are exposed to regular sequences of light and darkness...." It can be concluded that the relatively small scales of turbulent mixing may be less beneficial to algal growth than large-scale, regular mixing.

Other studies have been performed that show the improved effect of mixing on algal growth. In an article describing a numerical study with biological, environmental, and hydraulic considerations; Scott and Boriah [12] found that the 180° bends found in open raceways are beneficial to mixing and algal growth. They observed a helical flow downstream of the bends that invert the growth culture several times, but these effects are quickly dissipated and so are the benefits.

Another study discussed adding mixing enhancers to the straight sections of a raceway to promote mixing. Experiments by Laws *et al.* show that using the FLE can reduce photoinhibition and increase photosynthetic efficiency by a factor of 2.2. This effect was achieved in a raceway by arrays of airfoils, similar to those used for airplane wings, at high angles of attack that created trailing vortices [13]. This study took advantage of the increased, regular mixing concept from Miller *et al.* but with a much simpler design that has no moving parts and should require much less energy for circulation. The pressure differential from the top to the bottom of the airfoil creates tip vortices that are common yet undesirable on aircraft but that can improve mixing in algal raceways. The airfoils were arranged as shown in Fig. 1.3. The spacing regular spacing was used to reduce negative interaction of adjacent vortices by keeping the airfoil width and spacing the same as the water depth (D in the figure).

In addition to measuring the increased biomass after the growth period, Laws *et al.* measured the fluid by a simple cylinder approximately 5 cm in diameter with eight zero-pitch blades meant to follow the fluid rotation. The size of the device causes significant averaging for the vortex angular velocity measurement and could cause disruption of the flow. With today's improved fluid measuring techniques, these problems can be alleviated with high resolution and non-intrusive devices.

The results from the study show an optimal angle of attack of approximately 23°, but only three angles were tested. With a bulk velocity of 30 cm/s and water depth of 7.5 cm they used streamwise spacing of the airfoil arrays of 1.2 m and observed vortex structures throughout that length. Despite this spacing, the vortex rotation at the optimum

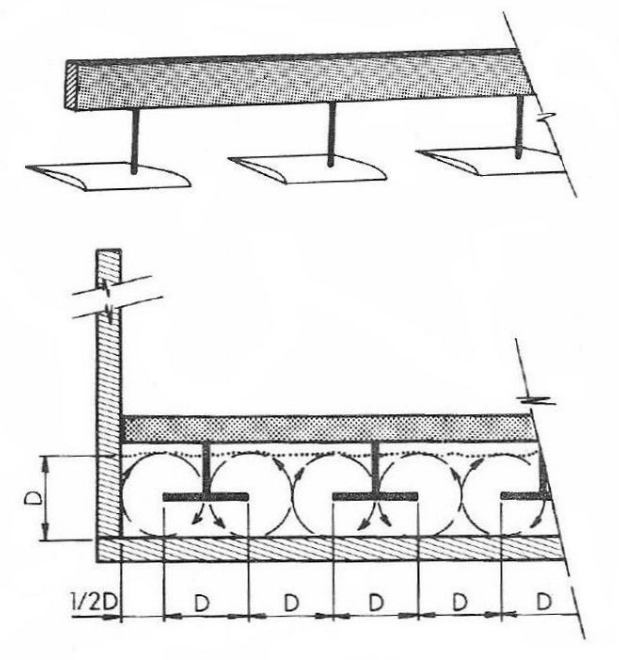

Fig. 1.3: Arrangement of airfoils in cross section of raceway with the water depth represented by D. Figure from [13] and used with permission.

angle of attack reduced quickly to half of that observed directly behind the airfoils within approximately 40 cm.

Other than airfoils, flat wings have been used to increase mixing. In one study, Biswas *et al.* attached them to the walls in heat exchangers to augment the heat transfer [14]. The wings create streamwise longitudinal vortices that significantly improve both downstream mixing and the heat transfer. They noted that adding the vortex generators increases pressure drop, so care must be exercised to optimize the heat transfer with respect to the increased pumping power from the addition of the wings.

In 1995 Cheng and Dugan produced one of the latest but often overlooked publications on mixing enhancement in open channel raceways [15]. They placed arrays of triangle and square shapes in the flow at angles of attack of 10° and 20°. The velocity sensor was simply a pressure transducer that may have been used as a rudimentary pitot probe to sense the streamwise component of velocity. Their channel was a shallow 10 cm and had a streamwise velocity around 0.3m/s. They took point measurements at differing depths and distances

downstream and calculated the Turbulence Intensity. They found the 20° angle to be much more effective at creating turbulence and increasing mixing than 10°. They also studied the spacing of the shapes in the transverse direction to the bulk flow. The square and triangle shapes were all 100 mm on a side, and they found that spacing them 300 mm apart to created as much turbulence as the 200 mm spacing with lower power and capital costs. The shapes added very little added power consumption with significant mixing enhancement.

Grobbelaar found that increased mixing can nearly double algal growth in a lab environment, but attributes the effect to be a decrease in boundary layer thickness and not the FLE [16]. To support this, he performed growth experiments with artificial light that was cycled at periods between 3 and 135 s. No trend was seen in the growth rate under this large range. A second experiment was performed with the same light patterns but increased the culture stirring speed with a significant increase in growth rates. He states:

> Mixing decreases the boundary layer and thus enhances the exchange rate for metabolites and nutrients between the cell and its environment, and as a consequence of this, utilizes light more efficiently giving the impression that mixing results in a better utilization of light energy, and hence growth. (p. 191)

He later suggests that researchers distinguish between the effect of light and turbulent mixing on algal cultures. The current work does not investigate whether light effects or a change in boundary layer thickness is the reason for significant growth increases from mixing, just that it occurs and can be used to grow algae with increased efficiency and at a lower cost.

1.3 Hypothesis

Increasing fluid mixing in raceway ponds should improve the growth rates that have previously been observed in standard depth ponds and allow for deeper ponds with higher production rates per land use as the algae will have more frequent exposure to the water surface and will experience increased nutrient homogeneity. The increased mixing can be realized with the addition of a Delta Wing (DW) at an angle of attack to the flow. A DW is an isosceles triangle made from sheet material and can create vortices similar to those on airfoils as studied by Laws *et al.*, but is much easier to manufacture. Cheng and Dugan

performed a study with the first publicized use of the DW to increase mixing in raceways, but did not call it such [15]. They pointed the tip down while it is predicted that having the tip up will produce vortices with more even spacing. The DW produces longitudinal line vortices that should significantly increase mixing and be sustained for significant lengths downstream. This effect is simulated by the animation (click to play) from a simple Computational Fluid Dynamics (CFD) model computed with Star-CCM+ as seen in Fig. 1.4. When used in commercial raceways, it is expected that the DW has the potential to increase algal growth by up to a factor of two.

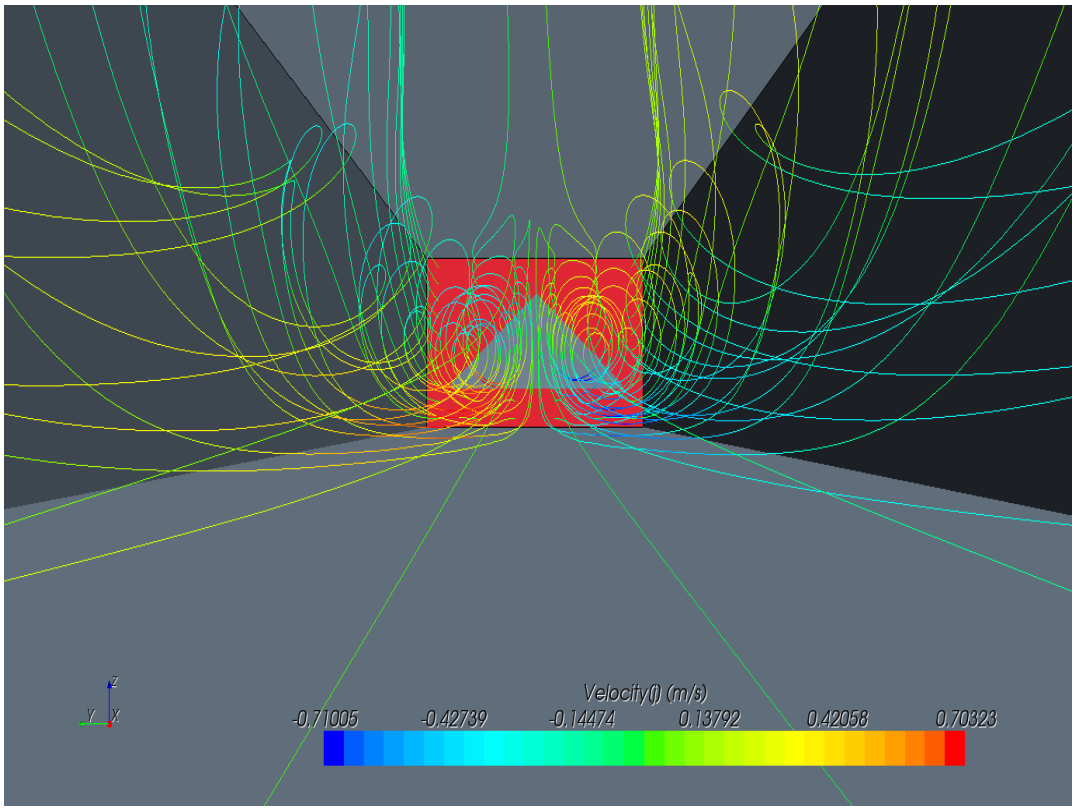

Fig. 1.4: Streamlines from a CFD simulation for a qualitative look at the circulating flow from the Delta Wing

Chapter 2

Objectives

The objectives for the work outlined herein are:

- Design experiment using Stereo Particle Image Velocimetry (PIV) to obtain three-component velocity data from experimental algal raceway
- Define mixing parameter to estimate level of mixing from DW using PIV data
- Determine optimal angle of attack for the DW
- Determine downstream length of enhanced mixing for wing spacing optimization
- Validate results by comparison with those of Acoustic Doppler Velocimeter for same flow conditions

Chapter 3

Methods

3.1 Experimental Raceway

An experimental algal raceway was built in the Sant Engineering Innovation Building at Utah State University with transparent acrylic sides for flow visualization and measurements (see Fig. 3.1). The Raceway is scaled from a $^1/_4$ acre production raceway to fit in the laboratory, but unlike production raceways, it contains only water. It uses a six-blade paddle-wheel to circulate the flow that is driven by a 1 hp, 1725 RPM, three-phase electric motor through a 60:1 gear reducer. The speed is controlled by a variable frequency drive (VFD) which can change the output continuously between no rotation to the motor's full speed. The VFD is an Emmerson Commander SK size B with single phase input power.

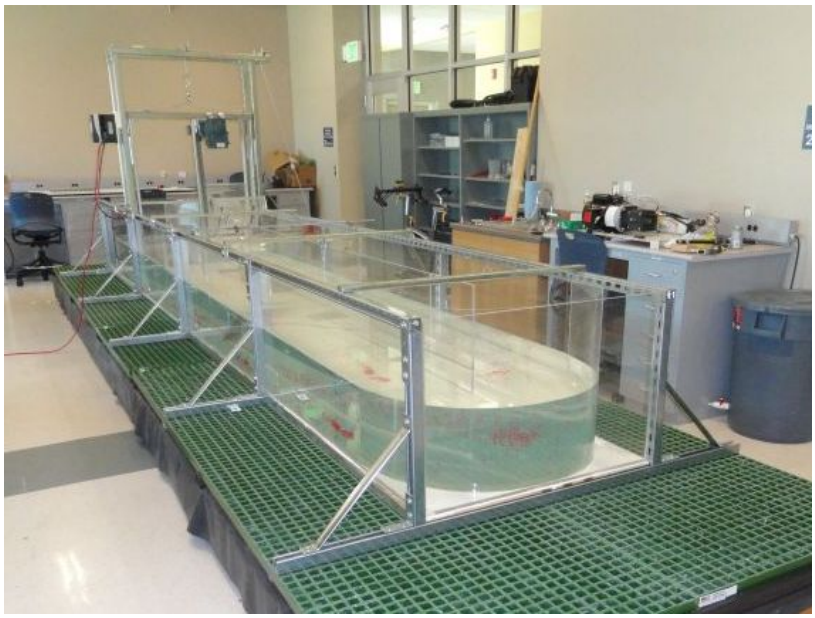

Fig. 3.1: Model Raceway constructed for fluid measurements

The raceway is twenty feet long and three feet wide with eighteen inch wide channels. The sides and center divider are made of half inch clear acrylic and the supporting structure is made of Unistrut® channel. The raceway can handle water depths up to eighteen inches, but all experiments outlined herein were performed at either eight or ten inches. The DW is an isosceles triangle 14.5 inches on each side whose mounting rod is located at the centroid. Flow conditioning is used, consisting of thin honeycomb material that is four inches thick with holes of approximately $^1/_4$ inch diameter. Tests showed that the flow conditioning makes the flow significantly more one-directional, but does not change the sizable recirculation zone from the 180° bend immediately downstream. A scaled drawing of the raceway geometry is shown in Fig. 3.2 showing the major components in the flow.

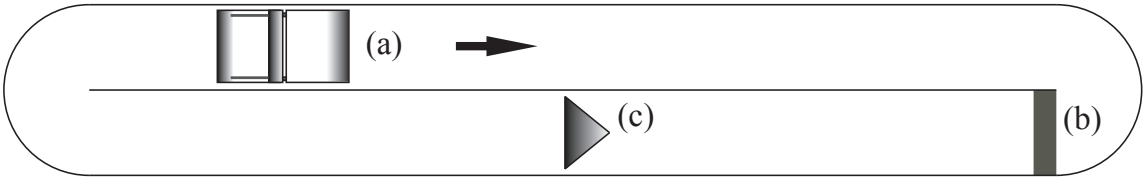

Fig. 3.2: Scaled sketch of experimental raceway with (a) paddle-wheel, (b) flow conditioning, and (c) delta wing

3.2 Power Measurement

The electric power was measured between the VFD and the motor by the use of a hall effect sensor, voltage divider, data acquisition device (DAQ), and computer. The hall effect sensor was model L18P003 made by Tamura whose voltage output was proportional to the current flowing through it. The voltage divider was made of 1% precision resistors and was required to reduce the high voltage signal by two orders of magnitude so as to be appropriate for the DAQ. The gain factor for the voltage divider used the measured resistance values instead of the nominal ones. The DAQ was model NI 9215 made by National Instruments and was a four-channel, 16 bit voltage reader with a ±10 V range.

Electric power P in a three phase AC circuit is commonly calculated by

$$P = 3V_\phi I_\phi \cos\theta \tag{3.1}$$

where V_ϕ and I_ϕ are the RMS components of the phase to neutral voltage and current respectively. The phase wire is one of the three physical wires carrying the power and is denoted by ϕ. The phase delay between the voltage and current in this wire is θ and will be between zero and ninety degrees when used with an induction motor.

The power in each phase can temporarily go negative due to the contributions of the reactive power to the real power. The real power is the useful power that does work, is always positive, and is the quantity that we wish to measure. Reactive power is the power that pulsates up and down the line that does no useful work, has an average of zero, and causes the magnitude of the phase power to go negative [17]. Even though the phase power can be negative, the cumulative power in the three phases of a balanced circuit is a constant with a magnitude three times the real power in each phase (see Fig. 3.3).

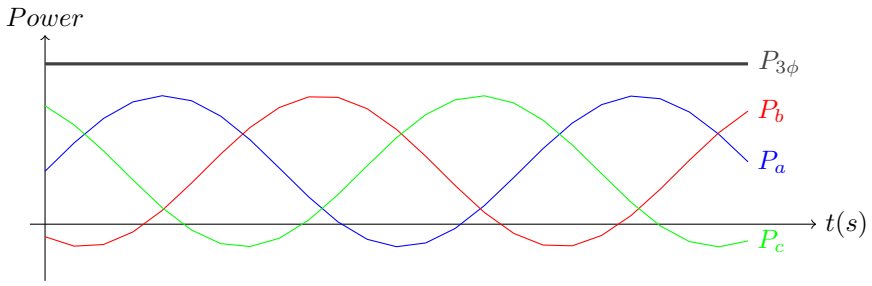

Fig. 3.3: Three Phase Power, adapted from [17]

Because the cumulative power can be found as stated above, only a single phase needs to be measured if the load is balanced. An equivalent method for measuring this power is to take instantaneous measurements of voltage and current and take the average of their product in the measurement interval as represented by

$$P = 3\sum_i V_{\phi,i} I_{\phi,i}/N \tag{3.2}$$

where N is the number of samples. The real power is obtained by averaging over many wavelengths since the reactive power is removed from the data (average of zero). This second equation is used in this work with the assumption that the three phases are balanced.

The VFD output signal is not a true sign wave but is made of relatively small amplitude pulses at frequencies in the kilohertz range. The VFD also outputs a large-scale, low frequency that causes the motor to see an apparent sine wave between 0 and 60 Hz. The current and voltage sensors were capable of passing the high frequency signals and were sampled at 50 kHz to capture the effect of the small pulses and distinguish the frequencies present by use of a fourier transform.

Once the signals were acquired by the computer, a low-pass Butterworth filter with cutoff frequency of 1 kHz was used for both signals. To calculate power, the filtered, instantaneous voltage and current were multiplied then averaged over a period sufficient to provide a converged estimate of the true power. Data were taken for a period of 10 minutes to cause the precision uncertainty to always be less than 0.75%.

An uncertainty analysis for the power measurement was performed based on expected results. The Taylor Series Method for Uncertainty Propagation was used on the data reduction equation for instantaneous power

$$P = 3\,VI \tag{3.3}$$

to give the expansion of

$$U_P = \sqrt{\left(\frac{\partial P}{\partial V}\right)^2 U_V^2 + \left(\frac{\partial P}{\partial I}\right)^2 U_I^2 + P_P^2} \tag{3.4}$$

where U_P is the overall uncertainty in power, U_V is the uncertainty of the voltage, U_I is the uncertainty of the current, and P_P is the precision uncertainty of power. This equation is normalized by power as

$$\frac{U_P}{P} = \sqrt{\left(\frac{U_V}{V}\right)^2 + \left(\frac{U_I}{I}\right)^2 + \left(\frac{P_P}{P}\right)^2} \tag{3.5}$$

The uncertainty of voltage depends on the uncertainty in the gain factor of the voltage divider. The gain factor is

$$V = V_0 \left(\frac{R_H + R_L}{R_L} \right) \tag{3.6}$$

where V_0 is the measured voltage, R_H is the high value resistor, and R_L is the low value resistor. A high accuracy multimeter, Hewlett Packard 34401A, was used measure the resistance values. The uncertainty in resistance takes on that of the meter whose specifications were found in the user manual; these uncertainty values were small compared to that inherent in the hall effect sensor. An uncertainty analysis for the current measurement was performed from the information on the hall effect sensor's data sheet with the result at 5% of the nominal magnitude expected. The current sensor's output was checked by the multimeter by wiring them in serial and driving a DC current through both. As seen in Fig. 3.4, the measured error was 2.5% of reading maximum. In total, the uncertainty in the power measurement was bounded by 5% of reading, and this value is used for all power measurements herein.

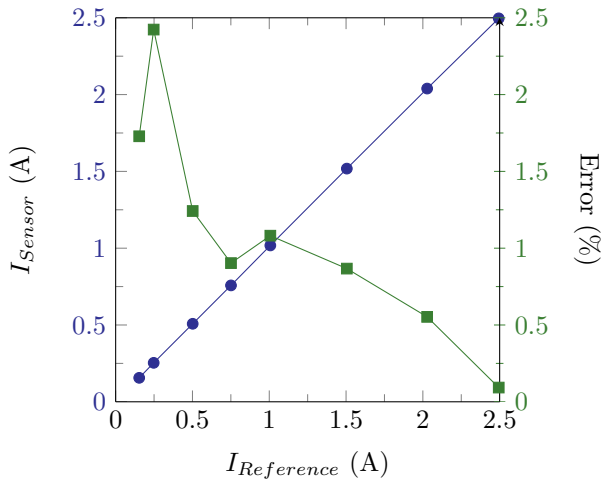

Fig. 3.4: Results from calibration of current sensor

The VFD has a basic, internal power sensor that is read from software; however, it has a minimum resolution of 10 W. Since the nominal load required about 60 W, this poor resolution motivated this additional power measurement. The VFD's converged average

was compared to that of this measurement with a maximum error of 5% with 2% typical. This provided excellent validation to our measurement and was within the uncertainty of the two methods.

3.3 Stereo PIV

An animation of the concept behind two-component PIV is shown in Fig. 3.5 (click to play) and shows the chronological process for acquiring PIV data. First the flow must be seeded with small particles that follow the fluid. These particles are illuminated by a laser sheet while images are simultaneously captured by the CCD camera. The image pairs are acquired close in time. They are analyzed in a cross-correlation computer algorithm that determines the direction and distance groups of particles have moved with the velocity vector field result. PIV will reveal much more about the flow than was previously found by all researchers on this topic by giving nearly 10,000 velocity vectors in the plane.

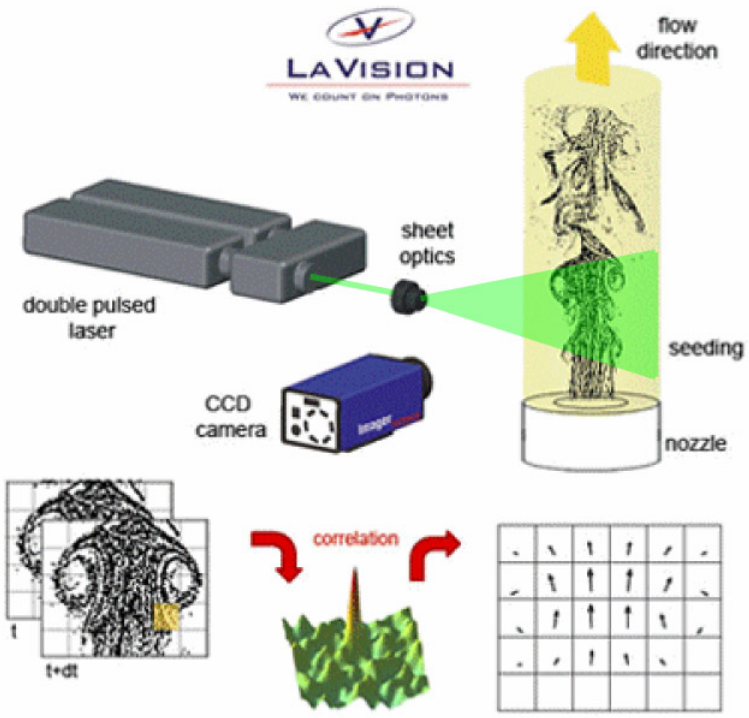

Fig. 3.5: Particle Image Velocity principles. Figure from [18] and used with permission.

A Stereo Particle Image Velocimetry (PIV) system from LaVision, Inc. was used to measure three components of instantaneous velocity in a plane normal to the direction of the flow. The increased difficulty of stereo measurements over two-component PIV is significant, but this method is necessary to resolve three components of velocity. Open channel flows are largely three-dimensional [19]. The cameras in the system are Imager Intense 12-bit CCD cameras made by PCO and sold by LaVision. The laser is a double pulse, 95 mJ Nd-YAG made by New Wave Research. The seed used in the raceway is hollow glass microspheres with an average diameter of 10 µm and density of 1.10 g/cc made by Potters Industries LLC (product 110P8). Both the seed diameter and density are very near that of algal cells, which allows the experiments to use clean water and apply the results to algal cultures without significant error.

The Stereo PIV arrangement for measurements at the model raceway can be seen in Fig. 3.6. In contrast to the two-component PIV in the animation above, Stereo PIV requires two cameras. These cameras are pictured in blue in the upper and lower portions of the picture while the laser pair is at the left-center of the image. The model raceway is in the upper-right portion in the image. The seed is illuminated green by the laser.

Because the cameras view the object plane at an angle with Stereo PIV, the entire plane can not be in focus at once with typical methods. To compensate for this, special Scheimpflug lens mounts are used. The Scheimpflug principle and device were patented in 1904 and, when used, allow the entire plane to be in focus by aligning the image plane, lens plane, and object plane for both cameras to intersect on a common line [20, 21].

Stereo PIV requires the use of a calibration plate with known geometry. The plate typically has two layers and two sides and is covered in marks; the geometry needs to be precise so the software knows how the object plane is mapped onto the image plane. LaVision, Inc. sells calibration plates for their PIV systems, but one of the proper size was not available to fill most of the model raceway. A new calibration plate was designed and fabricated and is seen in Fig. 3.7. The new plate was based on a commercial design but the marks were through-holes drilled in a painted black surface instead of the laser-etched on

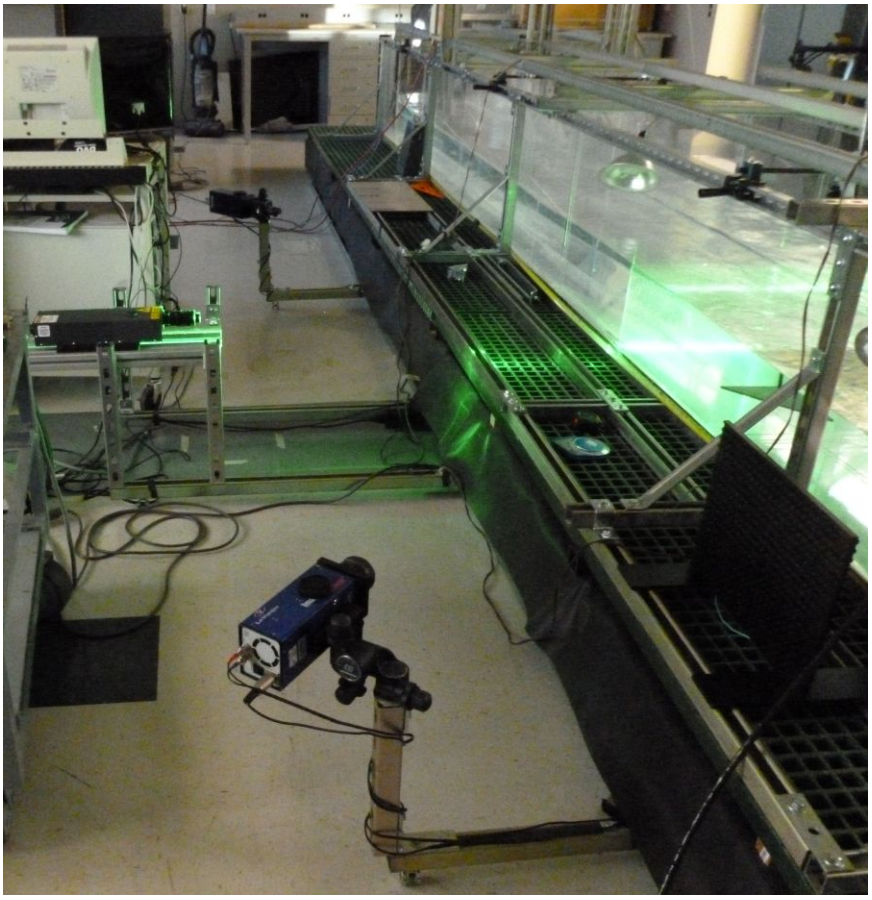

Fig. 3.6: Acquiring Stereo PIV measurements at model raceway

an anodized surface.

The PIV data were acquired and processed with DaVis 7.2 software from LaVision. All acquired images in a data set were averaged; this average was subtracted from each image to remove the negative effects of stationary background objects on the PIV cross-correlation. A mask was applied during the image processing to limit the resulting velocity vectors to the fluid area. Stereo cross-correlation was used for the PIV processing starting with 128×128 pixel interrogation regions with 50% overlap and ending with 32×32 pixel regions with the same overlap. The typical dewarped image has a size of 2200×1400 pixels resulting in a vector result with an approximate count of 138×88. The area inside the mask typically consisted of 128×72 vector results. The post-processing consisted of three steps: removing vectors if the Q ratio (the relative maximum correlation peak height to the

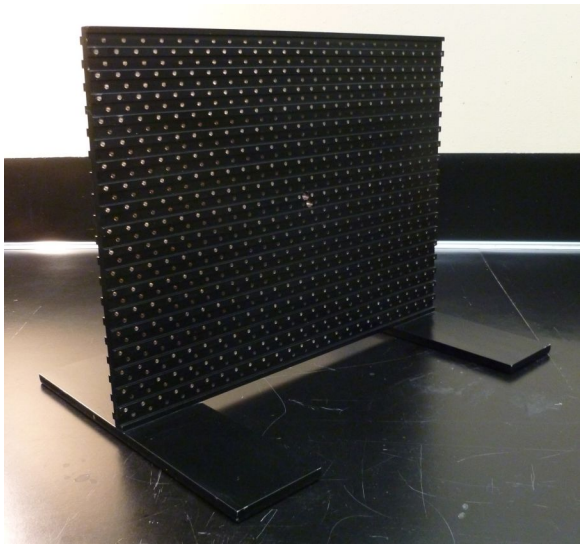

Fig. 3.7: Custom Calibration Plate for Stereo PIV

second highest) was less than 1.3, removing and replacing vectors if the difference is greater than 1.75×RMS of neighbors and less than 2.5×RMS of neighbors, and interpolating single empty spaces. The final step in processing was to calculate the average and RMS fields of the instantaneous data set through time.

After processing, the velocity data were exported to Tecplot® format files. These files were read by a personal Fortran code that would reorganize the data into three new files with the original geometry, each corresponding to one velocity component; this code is shown in Appendix A. These new files were read into a personal Matlab code that would calculate the Quantities of Interest and make plots in the fluid area that was not masked (see Appendices B & C).

A traversing system was built so the PIV system can slide along the Raceway while maintaining relative distances between the cameras, laser, and raceway; it is the metal structure linking these components in Fig. 3.6. This structure helped in consistency and reduced set-up time between measurement locations.

3.4 Quantities of Interest

3.4.1 Reynolds Number for Channel Flows

The Reynolds number Re for channel flow is

$$\mathrm{Re} = \frac{\bar{w} R_h}{\nu} \tag{3.7}$$

where $\bar{w}$ is the streamwise velocity, R_h the hydraulic radius, and ν the kinematic viscosity. The hydraulic radius is

$$R_h = \frac{A_c}{p} \tag{3.8}$$

where A_c is the cross-sectional area of the flow and p is the wetted perimeter [19]. The cross-sectional area is $A_c = DW$ where W is the raceway width (17.75 inches) and D is the water depth (10 inches). The wetted perimeter is $p = 2D + W$. The kinematic viscosity for water at 20°C is 1.0040E^{-6} m^2/s.

3.4.2 Standard Deviation

Several other quantities that will be useful to quantify the flow include the sample standard deviation, turbulence kinetic energy (TKE), and turbulence intensity. The sample standard deviation s is a measure of how far from the mean the typical value is found in a data set or is considered a measure of the fluctuation magnitude of the sample. The sample standard deviation of fluid velocity is

$$s_{\bar{v}_i} = \sqrt{\frac{1}{N-1} \sum_{j=1}^{N} (v_j - \bar{v}_i)^2} \tag{3.9}$$

where $s_{\bar{v}_i}$ is the sample standard deviation for each velocity component i, N is the number of samples, v_j is an instantaneous velocity measurement, and $\bar{v}$ is the mean velocity of the sample [22]. Because the parent population standard deviation can not known by discrete measurements, only the sample standard deviation s will be used in discussion. Here it must be noted that the components of velocity in the x, y, and z directions are referred to

as u, v, and w respectively. The standard deviation for each velocity component is u', v', and w'. Turbulent flows are typified by having fluctuating flow structures at many different length scales while laminar flows do not; therefore, u', v', and w' are often used to measure flow turbulence levels.

3.4.3 Turbulence Kinetic Energy

Turbulence Kinetic Energy $\bar{k}$ is another measure of flow unsteadiness [23] and is defined as

$$\bar{k} = \frac{1}{2}\left(\overline{u'u' + v'v' + w'w'}\right) \tag{3.10}$$

where $u'u' = (u')^2$, $v'v' = (v')^2$, and $w'w' = (w')^2$. The Turbulence Kinetic Energy will provide a single value to represent the fluctuation levels of all velocity components for each point. Again, the PIV results yield planes of data, so the TKE can be calculated over the entire domain.

3.4.4 Turbulence Intensity

A final method for quantifying the turbulence levels is to calculate the non-dimensional turbulence intensity by

$$Tu = \frac{\sqrt{\frac{1}{3}\left(\overline{u'u' + v'v' + w'w'}\right)}}{\bar{V}} = \frac{\sqrt{\frac{2}{3}\bar{k}}}{\bar{V}} \tag{3.11}$$

where Tu is the turbulence intensity and $\bar{V}$ is the average velocity magnitude. Turbulence intensity is often represented in percentage, with low values being around 1% and high values around 15-20% [23].

3.4.5 Precision Uncertainty

The precision uncertainty can be calculated to bound the random portion of uncertainty based on

$$U_i = t_{95}\, s_{\bar{v}_i}/\sqrt{N} \tag{3.12}$$

where U_i is the precision uncertainty of the mean velocity for each component i, t_{95} is the confidence level factor that is set to 1.96 for large samples and a 95% confidence level, and N is the number of valid vectors in the data set [22]. Since each velocity vector has three components, Equation 3.12 is applied to each independently. The root-sum-squared value of uncertainty U at each vector location is then calculated by

$$U = \sqrt{U_u^2 + U_v^2 + U_w^2} \tag{3.13}$$

where U_u, U_v, and U_w are the uncertainty of velocity in the x, y, and z directions respectively.

The relative precision uncertainty $U_{rel,i}$, in percentage, is calculated for each velocity component i by

$$U_{rel,i} = 100\, U_i/\bar{w}. \tag{3.14}$$

The normalizing is typically not done by the component velocities v_i because some are found to be near-zero in most flows, causing the relative uncertainties to diverge. Using $\bar{w}$ is common to address this issue. These component relative uncertainties are considered in the root-sum-squared expression

$$U_{rel} = \sqrt{U_{rel,u}^2 + U_{rel,v}^2 + U_{rel,w}^2} \tag{3.15}$$

to give the local relative precision uncertainty value for each vector location.

3.4.6 Vertical Mixing Index

No suitable method of quantifying mixing based on PIV data could be found in the literature; therefore, a new quantity was defined [24]. The Vertical Mixing Index (VMI) aims to reflect the amount of vertical mixing by considering the absolute value of the vertical component of velocity normalized by the planar average streamwise velocity $\bar{w}$ as

$$VMI = \frac{\sum_i^N \mid v_i \mid /N}{\bar{w}}. \tag{3.16}$$

The absolute value of vertical velocity is used because using v alone would result in a value near zero–the fluid volume rising must have a corresponding amount falling for the incompressible liquid. Fig. 3.8 shows a case with a relatively low VMI due to the absence of a DW. Compare this to a flow with significantly higher VMI from a DW at 40° angle of attack shown in Fig. 3.9. The vectors in these plots use the same scale to show the drastic difference the DW has on in-plane velocity.

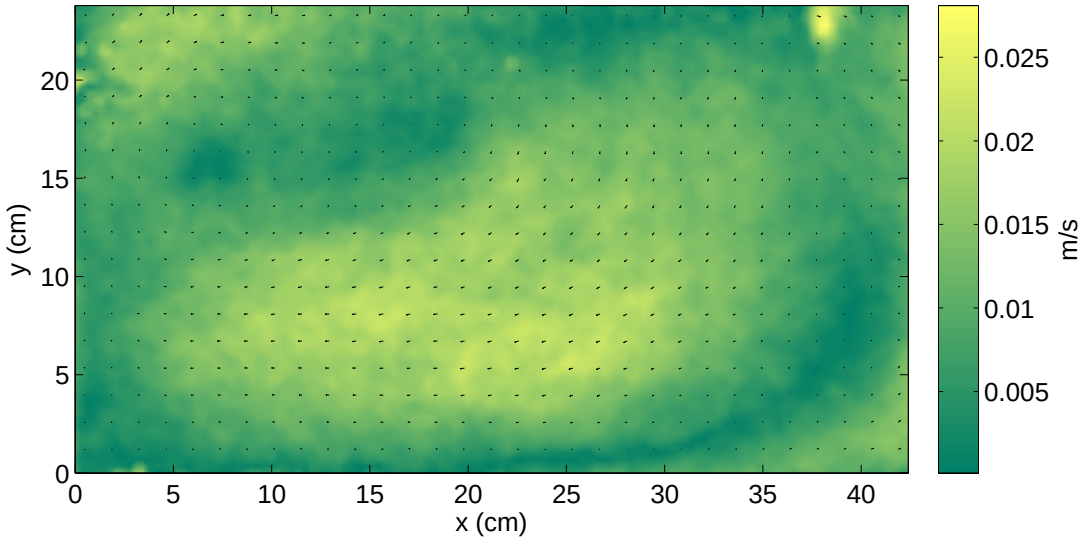

Fig. 3.8: In plane velocity without DW

3.4.7 Cycle Time

Much of the reviewed literature stressed the importance of the FLE to increased algal productivity, even though the ideal frequency of the light-dark cycles had a large range. Noting that the VMI has no consideration for the time required for the algae to experience these cycles, a new quantity was defined. Consider a basic equation for velocity $v = \Delta s/\Delta t$, or the average velocity is a change in position divided by a change in time. We can rearrange

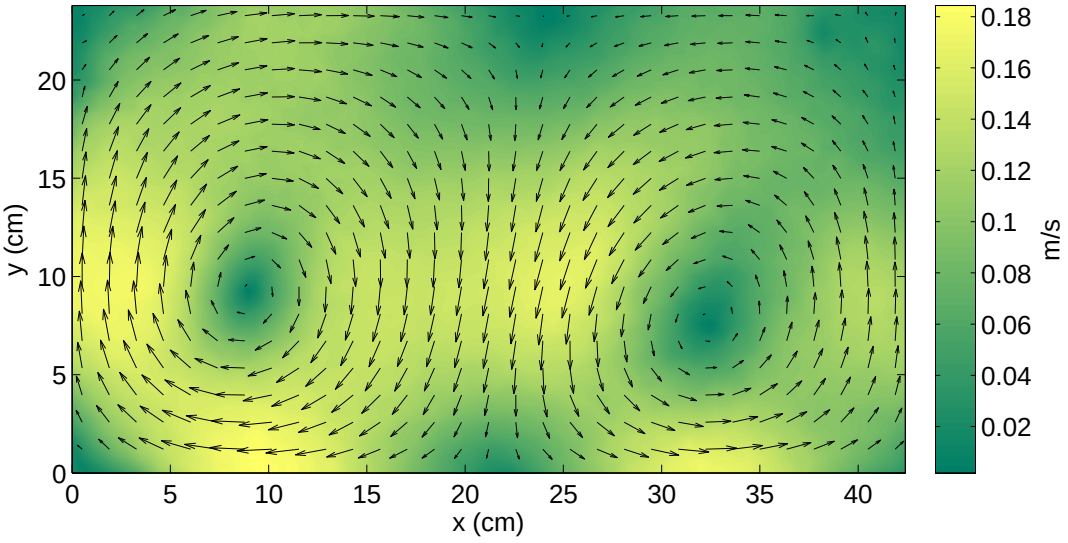

Fig. 3.9: In plane velocity with DW at 40° angle of attack

to solve for velocity and obtain the basis for the Cycle Time (Δt) definition

$$\Delta t = \frac{2D}{\sum_i^N \mid v_i \mid /N} \tag{3.17}$$

where D is the water depth as shown in Fig. 3.10. The algae cells have to cycle from the bottom to the top (or within the first 1-2 inches to absorb photons from the incident radiation), and back down again to complete their cycle. The distance traveled is therefore $2D$ and the average velocity is $\sum_i^N \mid v_i \mid /N$. All Quantities of Interest are computed from the PIV data in a Matlab code found in Appendix B.

3.5 Experimental Outline

The experiments in the experimental raceway comprise three separate studies: the Paddle-wheel Speed Study, the Angle of Attack Study, and the Vortex Dissipation Study. Stereo PIV and power data were acquired for all experiments. If power was neglected, it is expected that the highest paddle-wheel speeds and highest angles of attack would produce

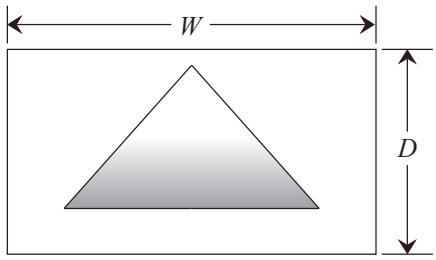

Fig. 3.10: Raceway cross-section with geometric definitions

the best results, but they both come at a price. The measured power is comprised of two parts: the first is that which is required to overcome fluid losses and maintain circulation while the second, termed "no-load," is that which is lost due to the inefficiencies of the motor, gear reducer, and chain. In other words

$$P_{measured} = P_{fluid\ load} + P_{no-load}. \tag{3.18}$$

To find the no-load power, the raceway was drained and power measurements were made with the paddle-wheel turning at the speeds used in the three studies. This power could then be subtracted from the measured power with fluid included, resulting in only the power to circulate the fluid, herein referred to as the Fluid Load. The Fluid Load would allow better comparison with CFD simulation results and raceways with different types of drives and motors. Since increased paddle-wheel speed and angle of attack are expected to increase power, this approach will normalize the higher mixing results from these cases.

Further considerations must be made to allow for direct comparison of results between the experimental raceway and much larger commercial raceways. For instance, if the VMI was simply normalized by the Fluid Load, the larger raceways would appear inferior due to larger loads. Normalizing must therefore be done by a non-dimensional power quantity that scales on size, fluid density, and streamwise velocity. The normalized power is defined as

$$P_{norm} = \frac{P_{fluid\ load}}{\rho A_c \bar{w}^3} \tag{3.19}$$

where $P_{fluid\ load}$ is the Fluid Load power, ρ is fluid density, and A_c is flow cross-sectional area. The normalized power term should be roughly equivalent in all expected configurations. This definition holds since $P_{fluid\ load}$ scales linearly with ρ, A_c, and $\bar{w}^3$.

For the Paddle-wheel Speed Study, the DW centroid was set at the center of the raceway in the channel opposite the paddle-wheel and four inches from the bottom with a 30° angle of attack and ten inches of water. The paddle-wheel turned at speeds between 2.40 and 14.38 RPM. The VMI and Cycle Time were calculated from the fluid data and normalized by the non-dimensional power P_{norm}.

For the Angle of Attack Study, the DW centroid was again set at the center of the raceway and four inches from the bottom as shown in Fig. 3.11. The water depth remained ten inches while the paddle-wheel rotated at 10.54 RPM. Eleven angles of attack were used between zero and fifty degrees inclusive. Again, the VMI and Cycle Time were determined and normalized by P_{norm}.

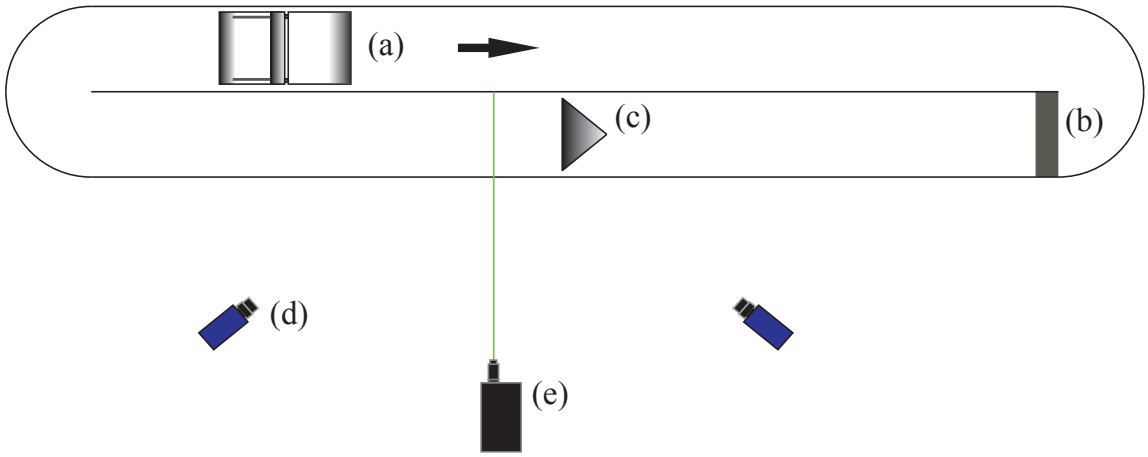

Fig. 3.11: Scaled sketch of experimental raceway with (a) paddle-wheel, (b) flow conditioning, (c) delta wing, (d) CCD cameras, and (e) Nd-YAG laser as configured for both the Paddle-wheel Speed Study and the Angle of Attack Study

The goal of the Vortex Dissipation Study was to measure the downstream length of vortex circulation. It used the results of the previous two experiments for the selection of

paddle-wheel speed and angles of attack. The DW centroid was positioned 48 inches from the end of the raceway and midway in water depth as seen in Fig. 3.12. Velocity data were obtained in twelve planes spaced twelve inches apart downstream of the DW. At every location, data without the DW and at five angles of attack were recorded. The VMI can be plotted over the length of vortex sustainment for each angle of attack to reveal the optimal angle. This study give the pertinent data to be used in an optimization study to determine spacing for the DWs in production raceways based on revenue.

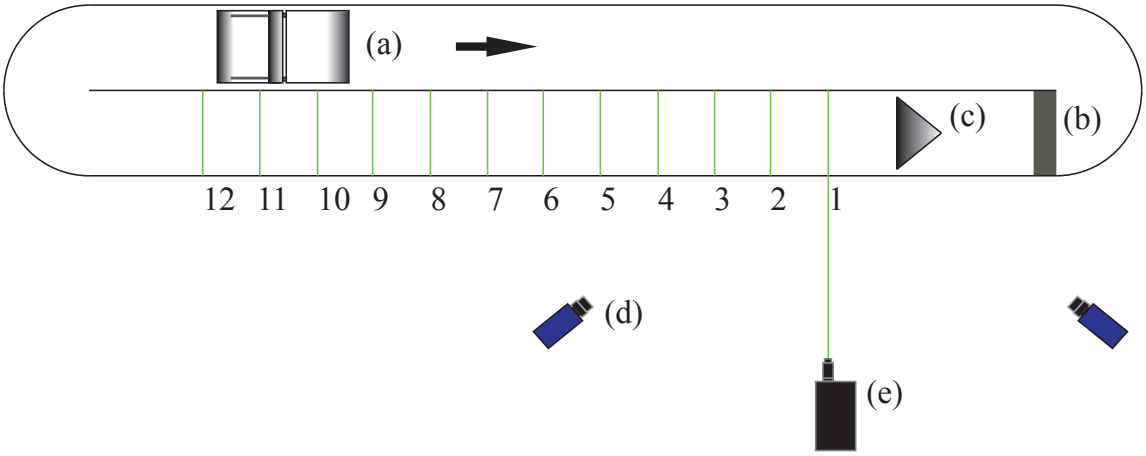

Fig. 3.12: Scaled sketch of experimental raceway with (a) paddle-wheel, (b) flow-straightener, (c) delta wing, (d) CCD cameras, and (e) Nd-YAG laser as configured for the Vortex Dissipation Study. The twelve green lines and numbers represent the twelve planes where data were taken as the laser and cameras were traversed along the raceway.

Data were acquired and compared with those from an Acoustic Doppler Velocimeter (ADV) from a previous study with matched flow parameters. The results of the two measuring techniques will be compared both qualitatively and quantitatively for increased data reliability. The ADV sensor is made by SonTek and is their 16 MHz MicroADV model that gives three component velocity measurements at a point. It was traversed through cross-sections of the flow in a 9×9 grid with higher spacial resolution near the bottom. The side and top boundaries have areas where data can not be obtained, so the PIV data were trimmed for better comparison.

Chapter 4

Results

4.1 Preliminary Results

Before considering the results for the VMI and Cycle Time, the input power to the paddle-wheel should be measured to normalize these quantities. It will be shown later that the power is a strong function of paddle-wheel speed, so the measured power and Fluid Load power results are shown in Fig. 4.1 as a function of this speed. The trend of the data is as expected since the paddle-wheel is similar to a centrifugal pump whose power is proportional to the speed or equally the velocity cubed [25]. The near-zero value for the Fluid Load power appears at the lowest speed due to the high-slip conditions at the paddle-wheel and/or could be the effect of measurement error.

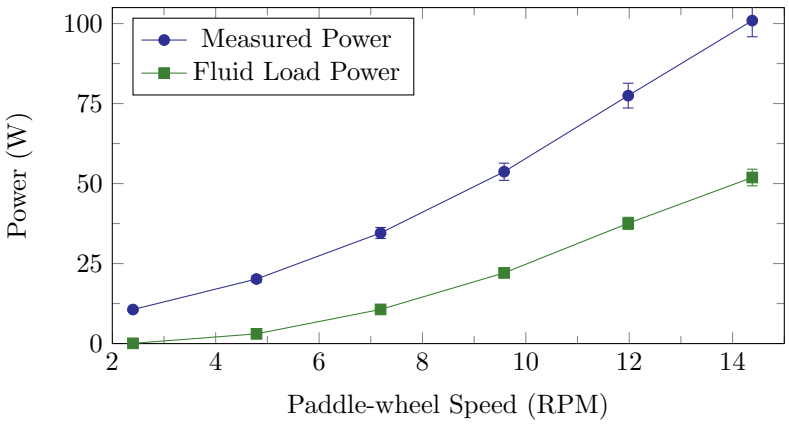

Fig. 4.1: Power considerations showing Measured Power and the Fluid Load Power as a function of paddle-wheel speed

Since paddle-wheel designs are different for each raceway, the streamwise velocities corresponding to these speeds are given in Table 4.1. This table also shows the relation to

the VFD frequency and paddle-wheel speed. Since the streamwise velocity is known, the Reynolds numbers can be calculated according to Equations 3.7 & 3.8 and are shown in the table.

Table 4.1: Paddle-wheel speed, streamwise velocity, and Reynolds number for the range of speeds tested

Variable Frequency Drive Speed (Hz)	Paddle-wheel Speed (RPM)	Streamwise Velocity (m/s)	Re
5	2.40	0.042	5640
10	4.79	0.087	11700
15	7.19	0.133	17800
20	9.58	0.180	24200
25	11.98	0.232	31100
30	14.38	0.275	36900

A convergence study was performed on the PIV data to determine how many images are required for a good estimate of the VMI. The results of the study are shown in Fig. 4.2 and show that 200 images are sufficient. All subsequent data sets were recorded using this number.

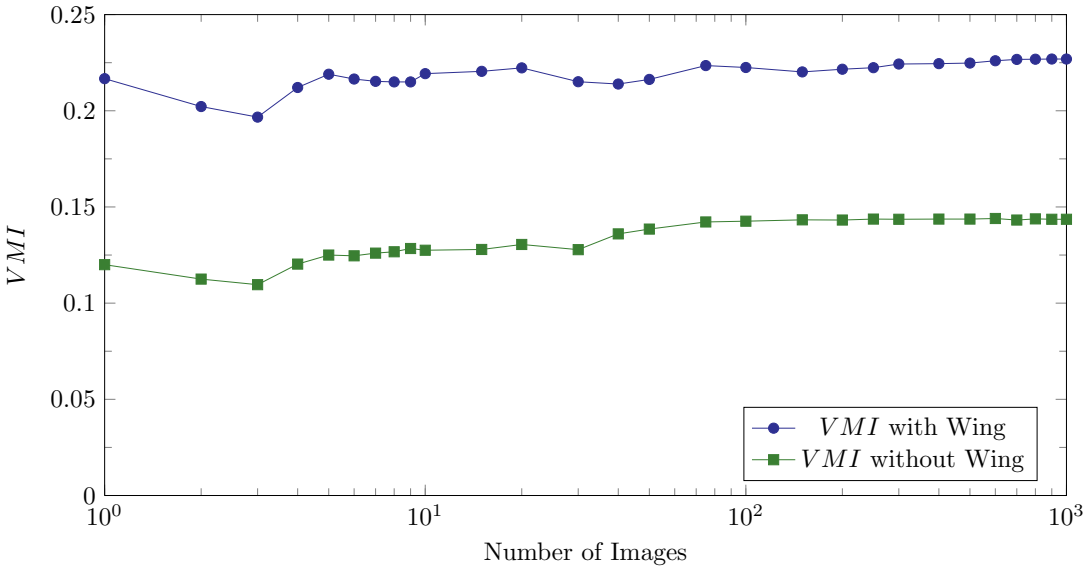

Fig. 4.2: Convergence study for PIV images

4.2 Paddle-wheel Speed Study

The Paddle-wheel Speed Study was performed with the DW at the center of the raceway at 30° angle of attack and ten inches of water. The results in Fig. 4.3 show that the VMI is independent of the paddle-wheel speed and thus the streamwise velocity. This effect ties back to the definition of VMI given in Equation 3.16 which has streamwise velocity in the denominator. This normalization was determined appropriate in order to make the VMI true to the typical usage of an index by removing any units. This effect has a distinct advantage of allowing direct comparisons between DW and other configurations without consideration to the streamwise velocity. The VMI normalized by the non-dimensional power is also shown in this plot. It appears that the lowest paddle-wheel speed is the best for this consideration, but the Cycle Time also needs to be considered before choosing a speed.

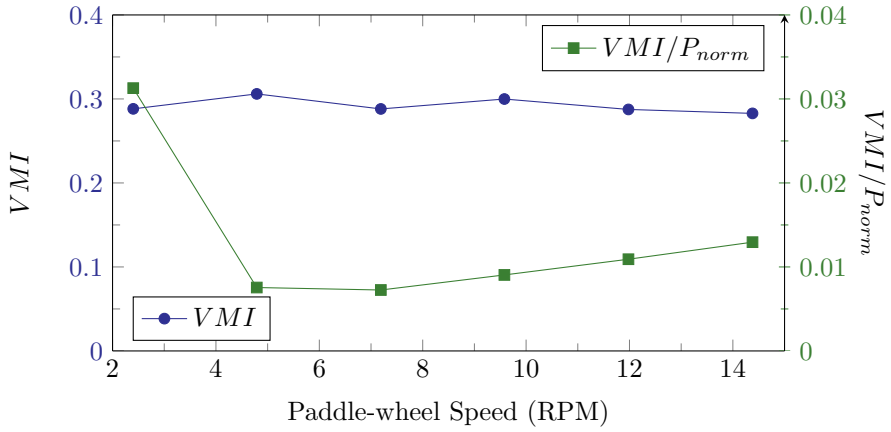

Fig. 4.3: Absolute and power-normalized VMI as a function of paddle-wheel speed

As well as considering VMI in the Paddle-wheel Speed Study, Cycle Time estimations were also made according to Equation 3.17. The results are shown in Fig. 4.4 and reveal that mixing times for algal cultures should decrease with bulk velocity in a nonlinear manner. These results also show that considering VMI alone to predict mixing is inappropriate. The plot also shows the Mixing Time normalized by the non-dimensional power, which suggests the highest speed to be optimal, opposite to the normalized VMI plot. Practicality must be

used to choose the best operating speed. Considering the nonlinear decrease of the Cycle Time allows us to choose a paddle-wheel speed that is low enough to save power (consider again Fig. 4.1) but high enough to mix sufficiently. The speed of 7.19 RPM (corresponding to 15 Hz on the VFD) is slightly lower than the mid-range tested and gives good mixing without the rapidly increasing cost of higher streamwise velocity. A speed of 9.58 RPM, which is 33% higher, requires more than double the power.

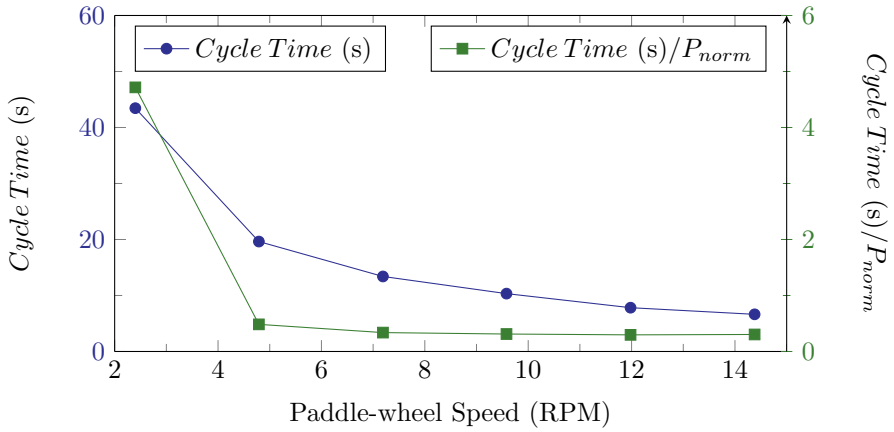

Fig. 4.4: Absolute and power-normalized Cycle Time as a function of paddle-wheel speed

The fluid velocity plot for the Speed Study at the chosen rate of 7.19 RPM is shown in Fig 4.5 for the entire measurement domain. The contour colors represent the velocity magnitude while the superimposed vectors show the in-plane velocity. This plot, as well as every remaining vector plot, has been down-sampled for easier reading. Each 4×4 vector group has been averaged to a single result for the in-plane velocity. Note the velocity magnitude is higher on the right half of domain. This is a remnant of the 180° bend upstream of the measurement location. The left portion experiences a sizable recirculation zone near the bend that causes the fluid in the right to move at higher velocity. This effect is still measured at this location ten feet downstream. The two vortices introduced by the DW are strong and fill the raceway cross-section. The opposite rotation directions are desirable so the velocity at their interface is flowing in the same direction instead of

opposite in direction.

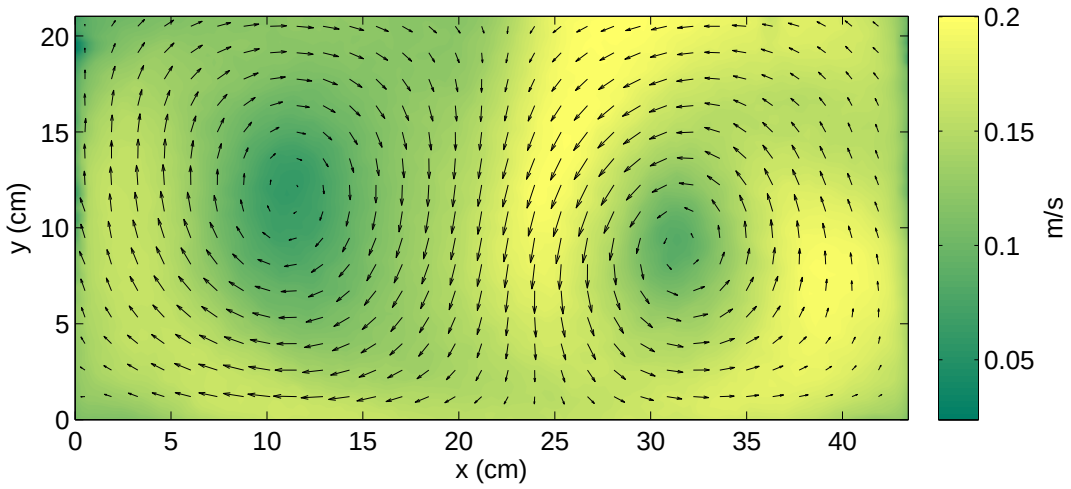

Fig. 4.5: Flow velocity for paddle-wheel speed of 7.19 RPM

Note that these quantities change significantly across the measurement domain, so considering a single value for any of them is inappropriate. The in-plane velocity in Fig. 4.6 shows the two strong, well-formed vortices clearly. The algae cells in a culture with this mixing structure would experience the desirable, nonrandom mixing structures recommended by Miller *et al.* [11].

The standard deviation result in Fig. 4.7 shows relatively large values, even close to the in-plane velocity, showing that the flow has significant fluctuations. The highest standard deviation is found in the centers of the vortices, showing local unsteadiness. The high values at the top center are where the fluid from each vortex meets and is highly unsteady also.

The precision uncertainty in Fig. 4.8 shows that local values change significantly over the measurement domain and that the measurements near the vortex centers have the highest uncertainty. The relative precision uncertainty of Fig. 4.9 gives the same result since it is normalized by the average streamwise velocity but shows that the uncertainty is less than 8% everywhere.

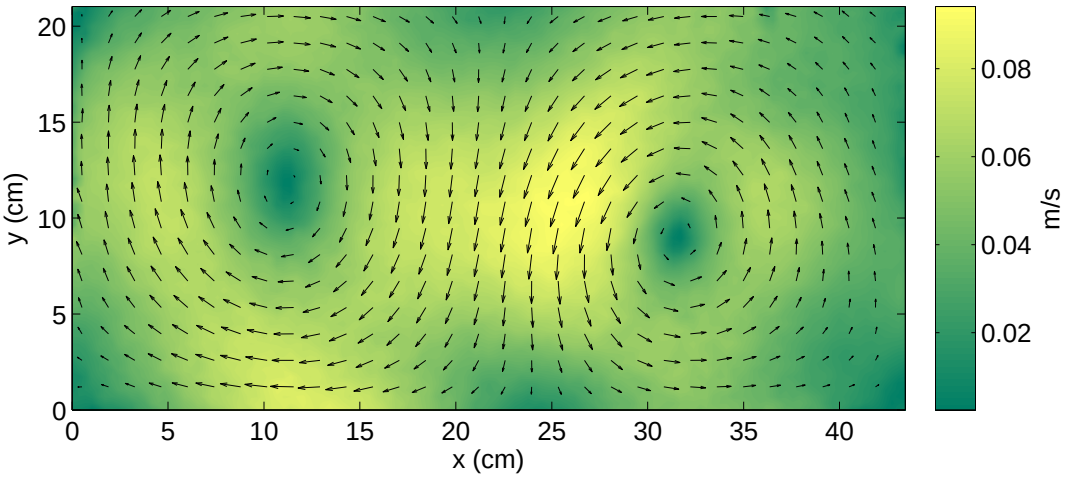

Fig. 4.6: In-plane flow velocity for paddle-wheel speed of 7.19 RPM

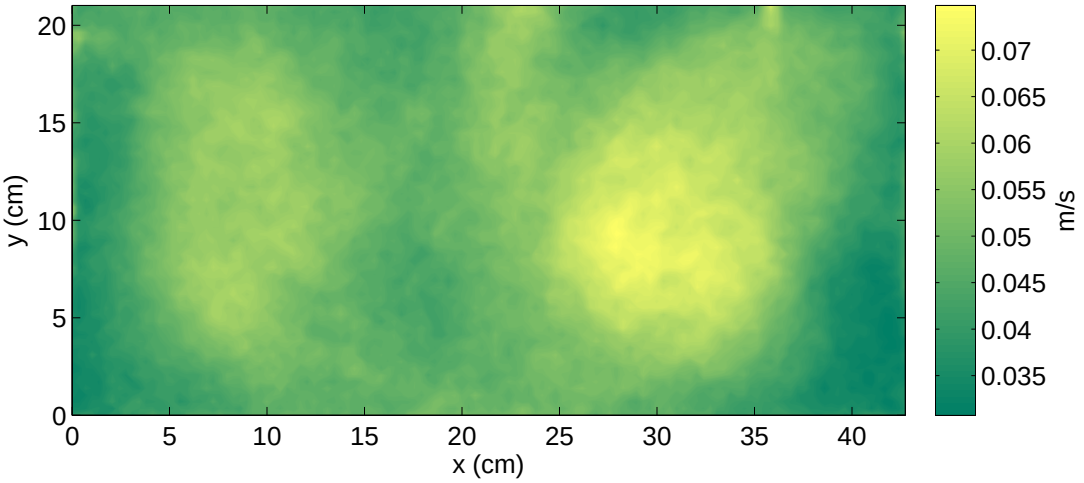

Fig. 4.7: Standard deviation of 200 instantaneous velocity fields for paddle-wheel speed of 7.19 RPM

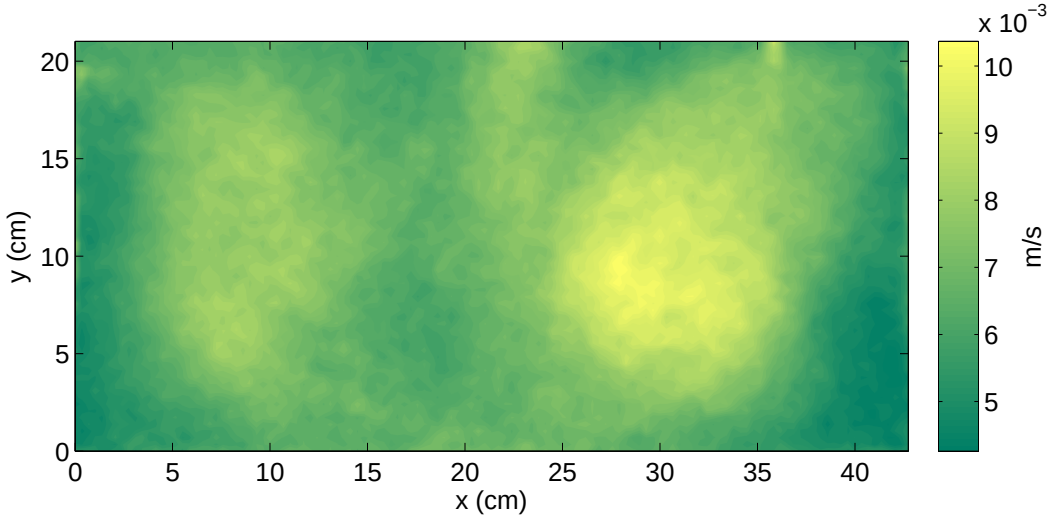

Fig. 4.8: Precision uncertainty of velocity for paddle-wheel speed of 7.19 RPM

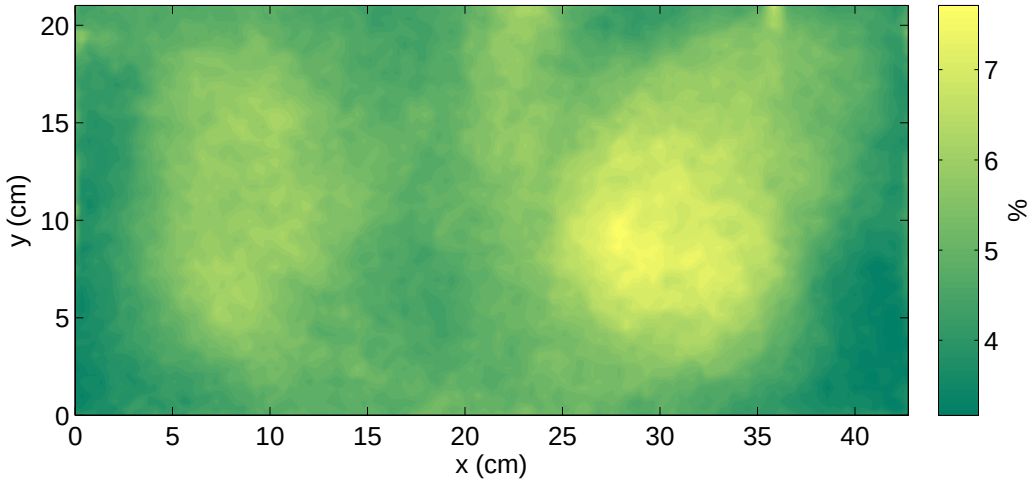

Fig. 4.9: Relative precision uncertainty of velocity for paddle-wheel speed of 7.19 RPM

The turbulence kinetic energy in Fig. 4.10 is very similar to the previous two plots but is displayed because this value is integral to the $k-\omega$ and $k-\epsilon$ turbulence model and is very useful in predicting other useful quantities.

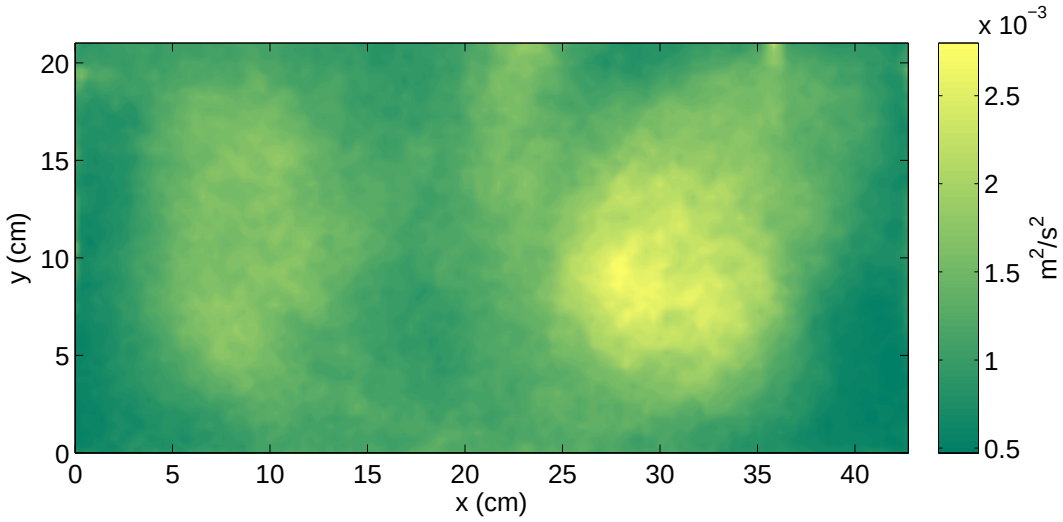

Fig. 4.10: Turbulence kinetic energy for paddle-wheel speed of 7.19 RPM

The turbulence intensity in Fig. 4.11 shows that much of the flow area has very high values, similar in intensity to combustion flow patterns [23]. The overall high turbulence intensity is a desirable effect described by Phillips and Myers when they said, "These considerations lead to the conclusion that almost any attempt to grow algae in sunlight will experience some gain by turbulence" [9].

4.3 Angle of Attack Study

For the Angle of Attack Study, the paddle-wheel was circulated at an arbitrary 10.54 RPM and the DW was again placed at the center of the raceway with ten inches of water. The DW centroid height was kept at four inches from the bottom to keep the tip from leaving the water. The angle of attack was varied from 0-50° with the power and fluid dynamics measured. The Fluid Load as a function of angle of attack is plotted in Fig. 4.12;

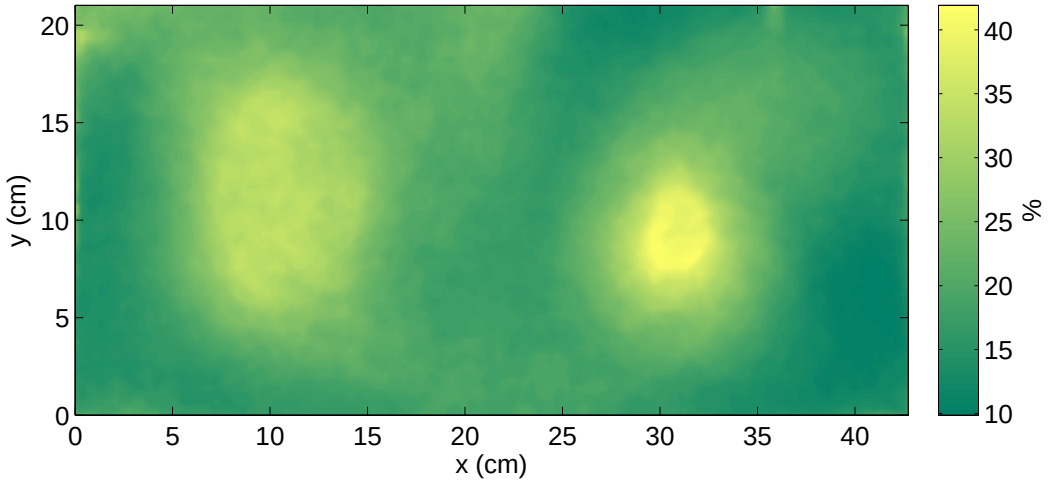

Fig. 4.11: Turbulence intensity for paddle-wheel speed of 7.19 RPM

and, as stated earlier, is not a strong function of the angle. There is a significant increase in Fluid Load at 50° and moderately so at 45° due to the blunt shape of the DW at these higher angles.

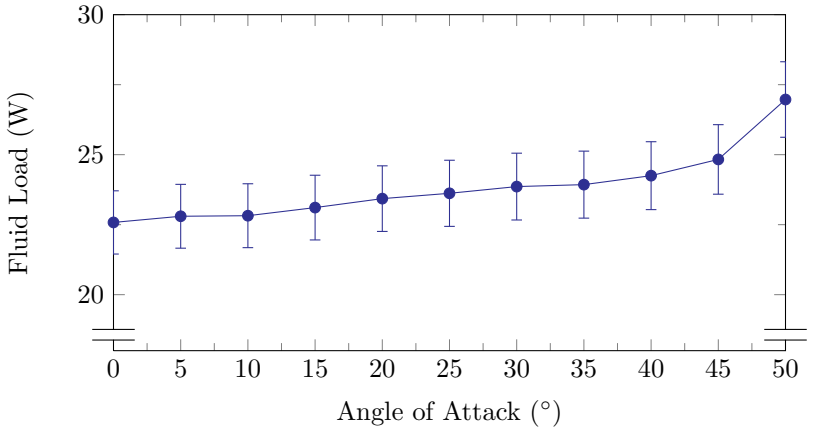

Fig. 4.12: Fluid power as a function of angle of attack

Even though Fluid Load is not a strong function of the angle of attack, both VMI and

Cycle Time results are. As shown in Fig. 4.13, there exists an optimal angle of attack of 40°, even for the power-normalized case. The angles lower than 40° produce vortices with lower strength. The vortex strength of those above the optimal is diminished since the DW is acting more as a blunt object in the flow instead of producing mixing. The optimal angle has never been studied this thoroughly or with such high-fidelity data. Laws *et al.* studied three angles, but their measurement system was comparatively rudimentary [13]. Cheng and Dugan studied only 10° and 20° angles, citing the results from 20° to be far superior [15]. This study covered a huge range of angles to reveal the optimal at 40°.

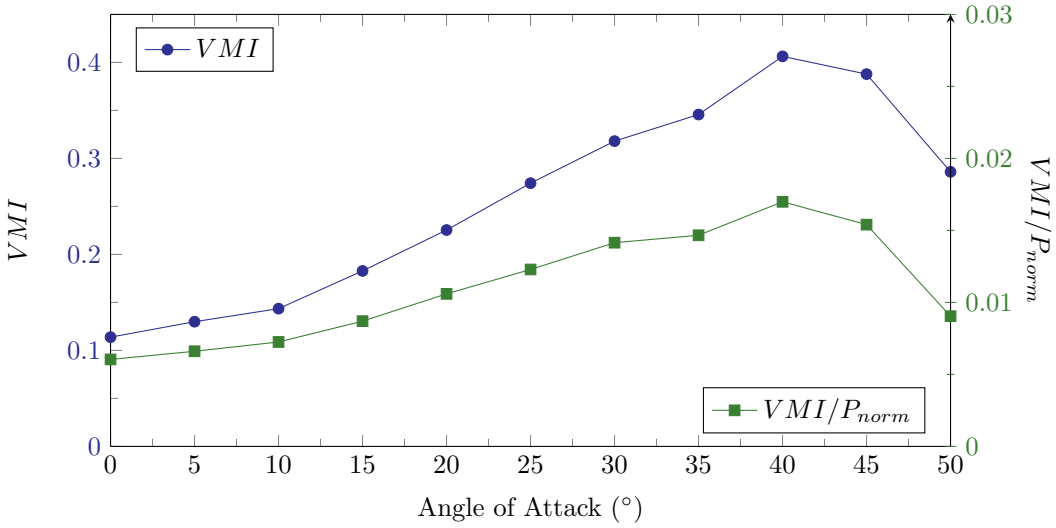

Fig. 4.13: VMI as a function of angle of attack. The y-axis on the left is absolute VMI where the y-axis on the right shows the power-normalized VMI. Because the Fluid Load is a weak function of angle of attack, the two trends are similar.

The Cycle Time also has an optimal angle of attack of 40° as seen in Fig. 4.14 where the lowest value is ideal. Again, one of the curves is normalized by the non-dimensional power, but the trend is only slightly changed. Thus, by both considerations, an angle of attack of 40° is optimal for the DW. The optimal Cycle Time value of around 10 s is at the upper range of the best periods to take advantage of the FLE. But this result is still encouraging because the DW significantly decreases the Cycle Time (compare around 22 s

from 0° to the approximate 7 s from 40°) with a device that is extremely simple to build and use and adds very little power.

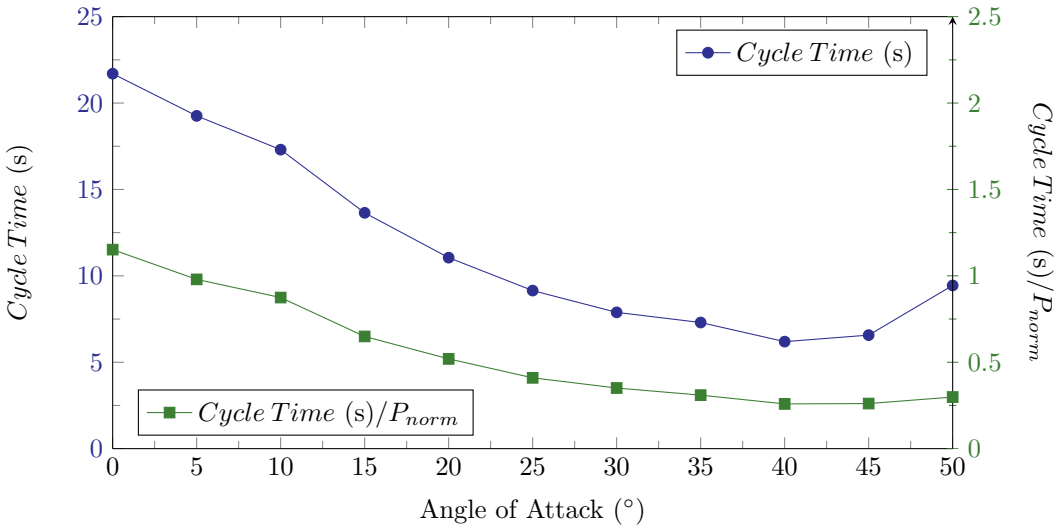

Fig. 4.14: Cycle Time as a function of angle of attack. The y-axis on the left is the absolute Cycle Time where the y-axis on the right shows the power-normalized Cycle Time. Because the Fluid Load is a weak function of angle of attack, the two trends are similar.

The Reynolds numbers in Table 4.1 show the flow is turbulent for all but the lowest paddle-wheel speed tested, so fluctuations in the flow are expected. As stated earlier, 200 images were acquired for every set giving 200 instantaneous vector fields and subsequent values for VMI and Cycle Time. The SDs for these quantities were calculated for each set in the Angle of Attack Study and are shown in Fig. 4.15 & 4.16. The SD values generally follow the trends of their nominal quantities, but have values around 20%, suggesting that the flow is highly unsteady. Even though the Cycle Time SD follows the trend for Cycle Time, that on the VMI plot does not. This suggests that higher angles of attack produce the vortex structures that are steadier through time, resulting in lower dissipation rates.

The fluid velocity for the optimal angle of 40° is shown in Fig. 4.17 with the contour colors representing velocity magnitude and the superimposed vectors showing the in-plane components of velocity. Notice how the vortex centers have shifted down from those in the

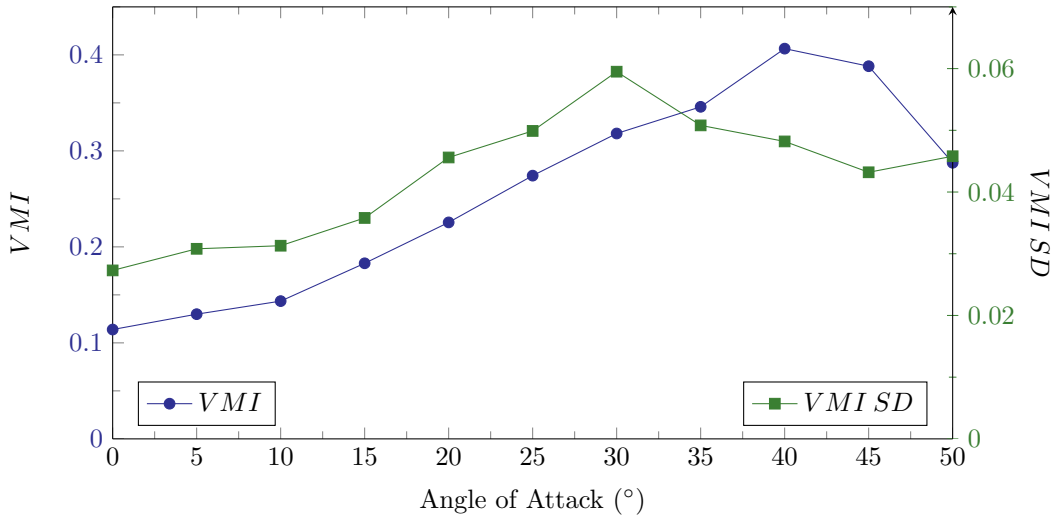

Fig. 4.15: VMI and VMI standard deviation as a function of the angle of attack

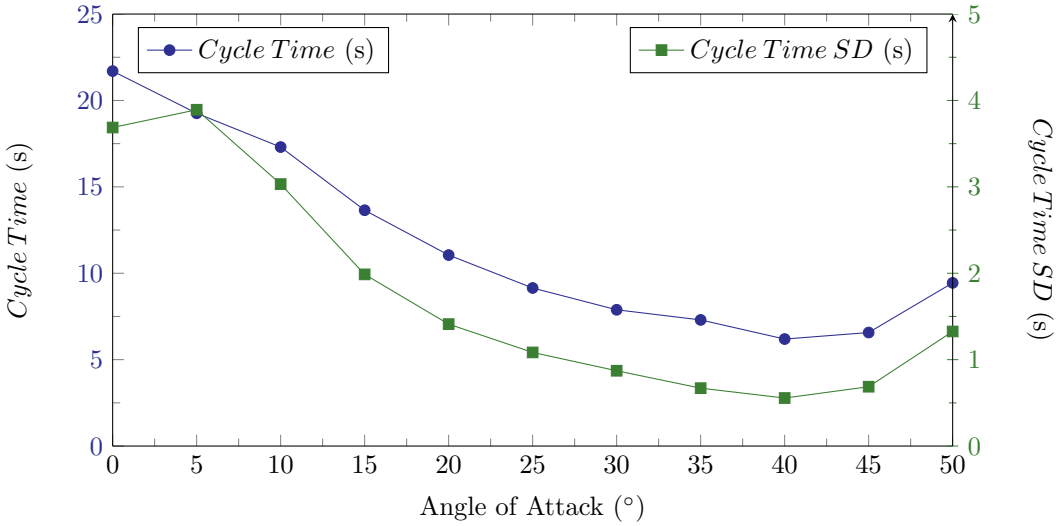

Fig. 4.16: Cycle Time and Cycle Time standard deviation as a function of the angle of attack

Paddle-wheel Speed Study even though the speed is the same (see Fig. 4.5). This is due to the change in angle of attack. The angle for the Speed Study was held constant at 30°, so an observed lowering of the vortex centers is due to this increase in angle. Having the vortex centers off of the mid-height line is undesirable because the circulating fluid structures are constrained to deform with each rotation, likely increasing the viscous dissipation. Care

was taken during the Vortex Dissipation Study to keep the DW centroid at mid-height to bring the vortex centers higher even though its tip would be above the water surface.

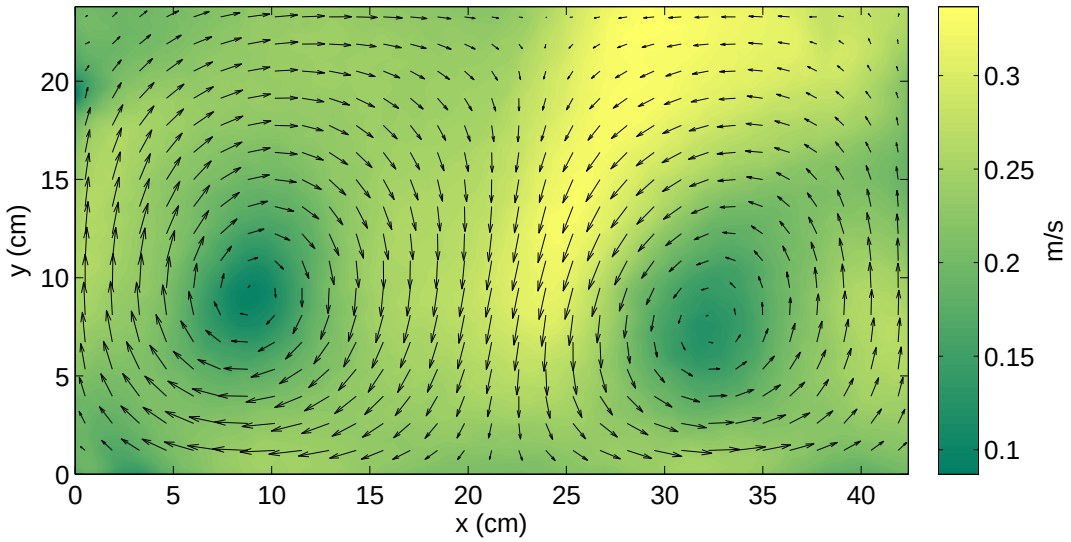

Fig. 4.17: Flow velocity for a 40° angle of attack

The in-plane velocity in Fig. 4.18 shows the two strong, well-formed vortices clearly. The maximum observed in-plane velocity is nearly twice that of the Speed Study due to the increase in angle of attack from 30° to 40° as well as inreasing the paddle-wheel speed.

The standard deviation result in Fig. 4.19 shows relatively large values, but not as high as the in-plane velocity, while the other aspects are similar to previous findings.

The precision uncertainty in Fig. 4.20 shows similar results as before with the highest values at the vortex centers. The relative precision uncertainty of Fig. 4.21 shows that the uncertainty is less than 11% everywhere. This result is higher than seen in the Speed Study, likely due to the increased unsteadiness from the higher angle of attack.

The turbulence kinetic energy in Fig. 4.22 is very similar to the previous two plots but is approximately three times that in the earlier study.

The turbulence intensity in Fig. 4.23 shows that much of the flow area has very high values with a maximum nearly three times the earlier study. This intensity is five times

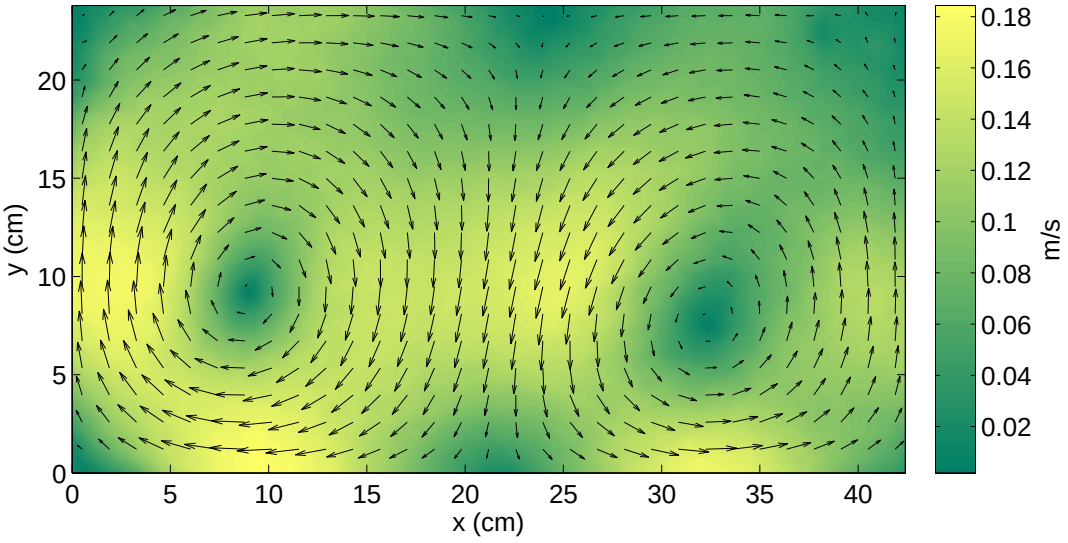

Fig. 4.18: In-plane flow velocity for 40° angle of attack

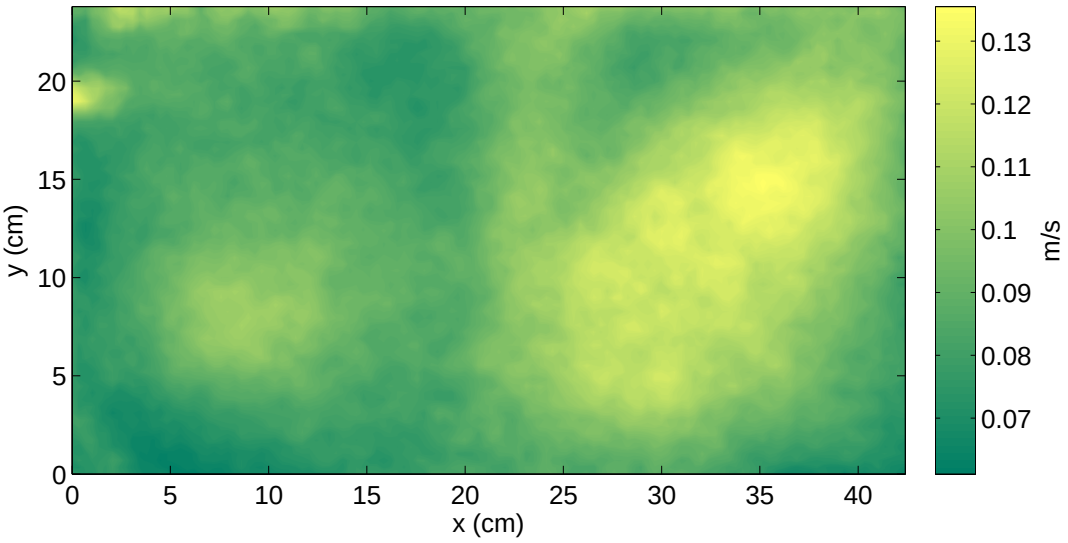

Fig. 4.19: Standard deviation of 200 instantaneous velocity fields for 40° angle of attack

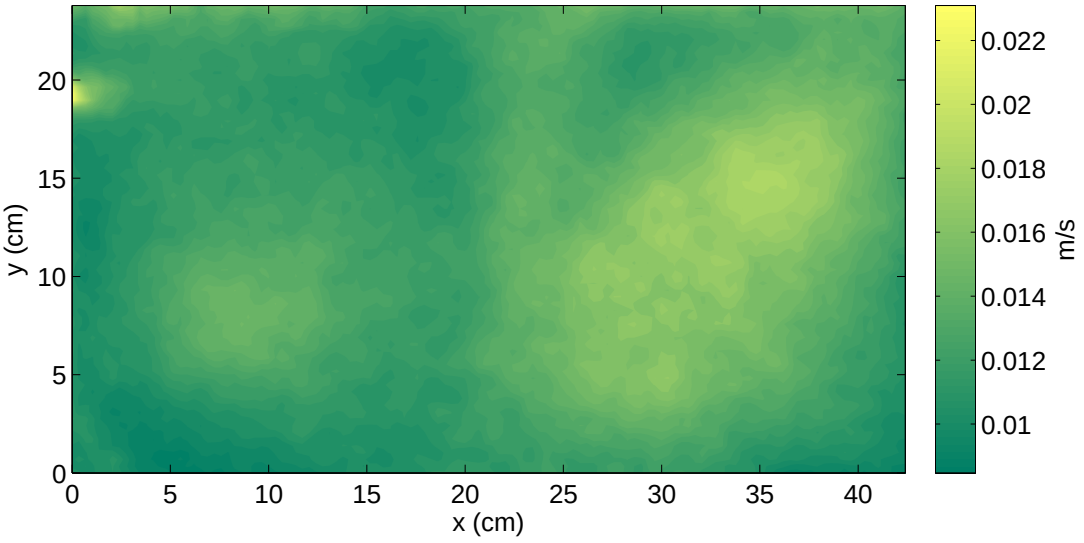

Fig. 4.20: Precision uncertainty of velocity for 40° angle of attack

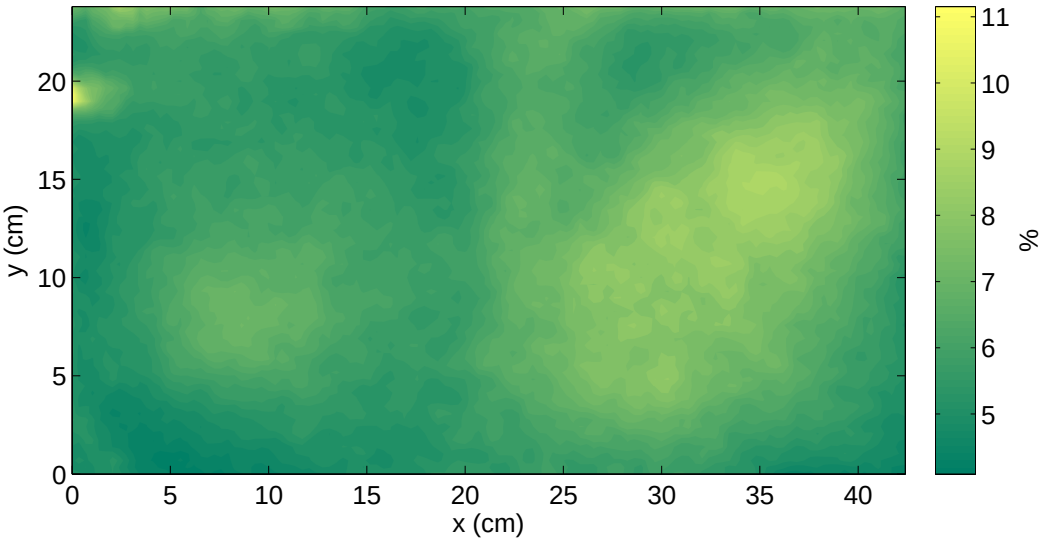

Fig. 4.21: Relative precision uncertainty of velocity for 40° angle of attack

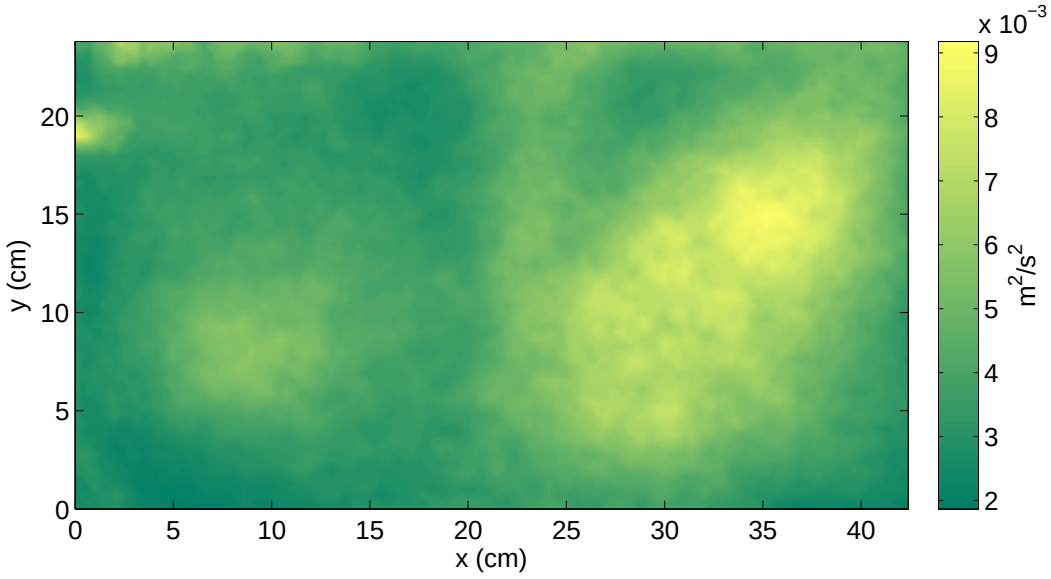

Fig. 4.22: Turbulence kinetic energy for 40° angle of attack

greater than that measured by Cheng and Dugan with lower streamwise velocity when they used plates at 20° angle of attack. When comparing their findings to the 20° angle from this study, it is still only one fifth the magnitude since changing the angle does not appear to drastically change the turbulent intensity. Since they used the DW with the tip down, it is likely the resulting vortex spacing would be uneven and would dissipate faster. It could also be that the PIV data, being susceptible to noise, could be over-predicting these values, but the factor of five overestimation is unlikely.

4.4 Vortex Dissipation Study

The final study was performed with the DW near the upstream end of the raceway to allow fluid measurements far downstream. The downstream data was used to determine the sustained length of increased mixing from the vortices. Again, ten inches of water were used with the DW centroid at mid-depth. The paddle-wheel speed was held constant at 7.19 RPM due to the results of the Paddle-wheel Speed Study. Fluid measurements were made as close to the DW as possible on the downstream side (fourteen inches) and

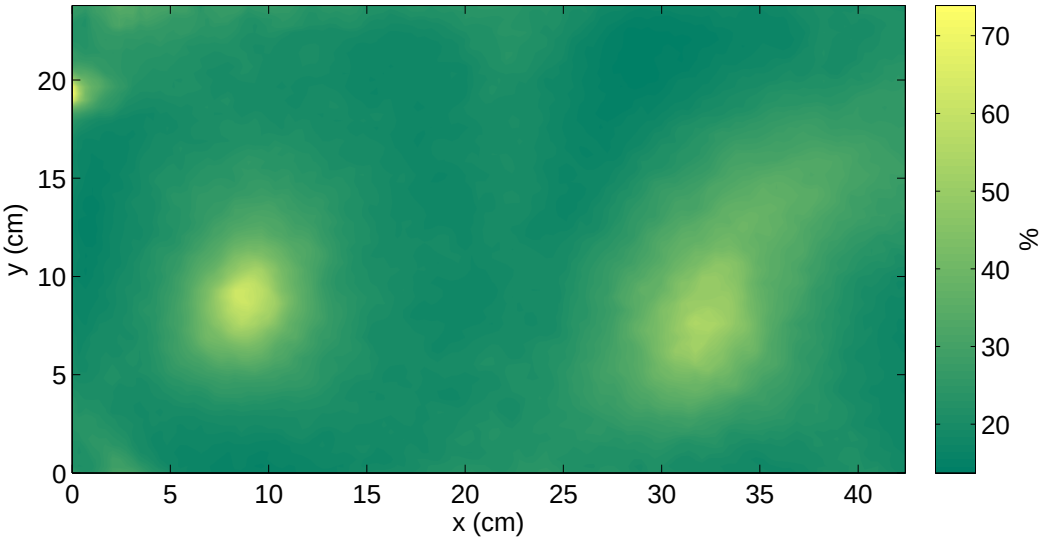

Fig. 4.23: Turbulence intensity for 40° angle of attack

repeated every twelve inches for twelve planes with five angles of attack (10-50°). The Fluid Load results are shown in Fig. 4.24 and have a similar trend as those for the Angle of Attack Study, but the magnitude is approximately half due to the lower paddle-wheel speed.

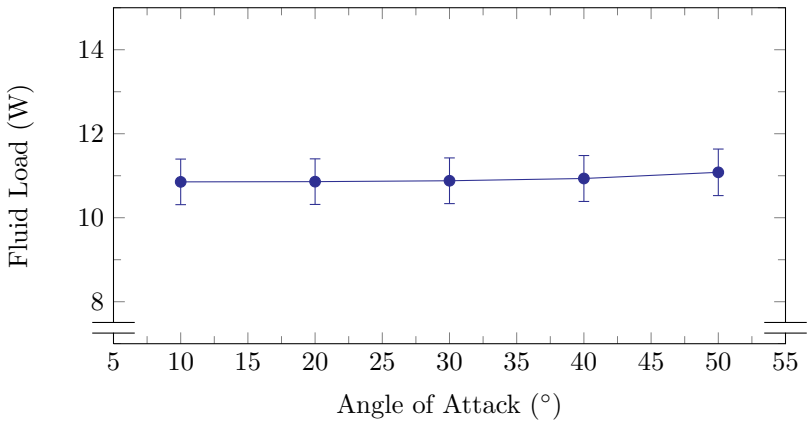

Fig. 4.24: Fluid Load as a function of angle of attack during the Vortex Dissipation Study

The results for the VMI show significant mixing from the delta wings over a sustained

period. As expected from the Angle of Attack Study, the angle of 40° is optimal for both VMI and Cycle Time. The result that was not clear before this study is which angle would prove best at sustained mixing downstream. The absolute VMI in Fig. 4.25 and the power-normalized VMI in Fig. 4.26 show that the 40° angle is best at nearly every point for the entire twelve feet measured. Like the Angle of Attack Study, both the 30° and 50° angles perform similarly, but the latter requires more power. The study from Laws *et al.* produced a similar plot in their study using airfoils, but only three angle were used and there was no baseline (without the airfoils). Nevertheless, they did find that the vortex rotation reduced to half of the initial value within about 16 inches and is expected to be unmeasurable in 40 inches. This rapid dissipation in their study is mainly due to their shallow three inch water depth, much smaller than our ten inch depth. The smaller water volume carries less momentum, so vortex structures would dissipate faster. The larger vortex structures in the experimental raceway can be measured out to twelve feet for the optimal angle.

Both the absolute and power-normalized Cycle Time plots reveal the same optimum as the VMI plot. The optimal angle is again 40° through the length of the area measured, with 30° and 50° equally secondary. These plots, shown in Fig. 4.27 and Fig. 4.28, appear to have more noise from one point to another on the x-axis. With the challenging Stereo PIV calibration attempting to compensate for significant optical refraction, calibration errors could appear with a changes in the distance from the DW. An error in VMI could be nullified by the normalization by streamwise velocity where Cycle Time does not have the same advantage. Also note the point where the 40° and 50° curves cross. This point is expected to have a bias error likely due to the optical disruption caused by the joint in acrylic panels on the side of the raceway.

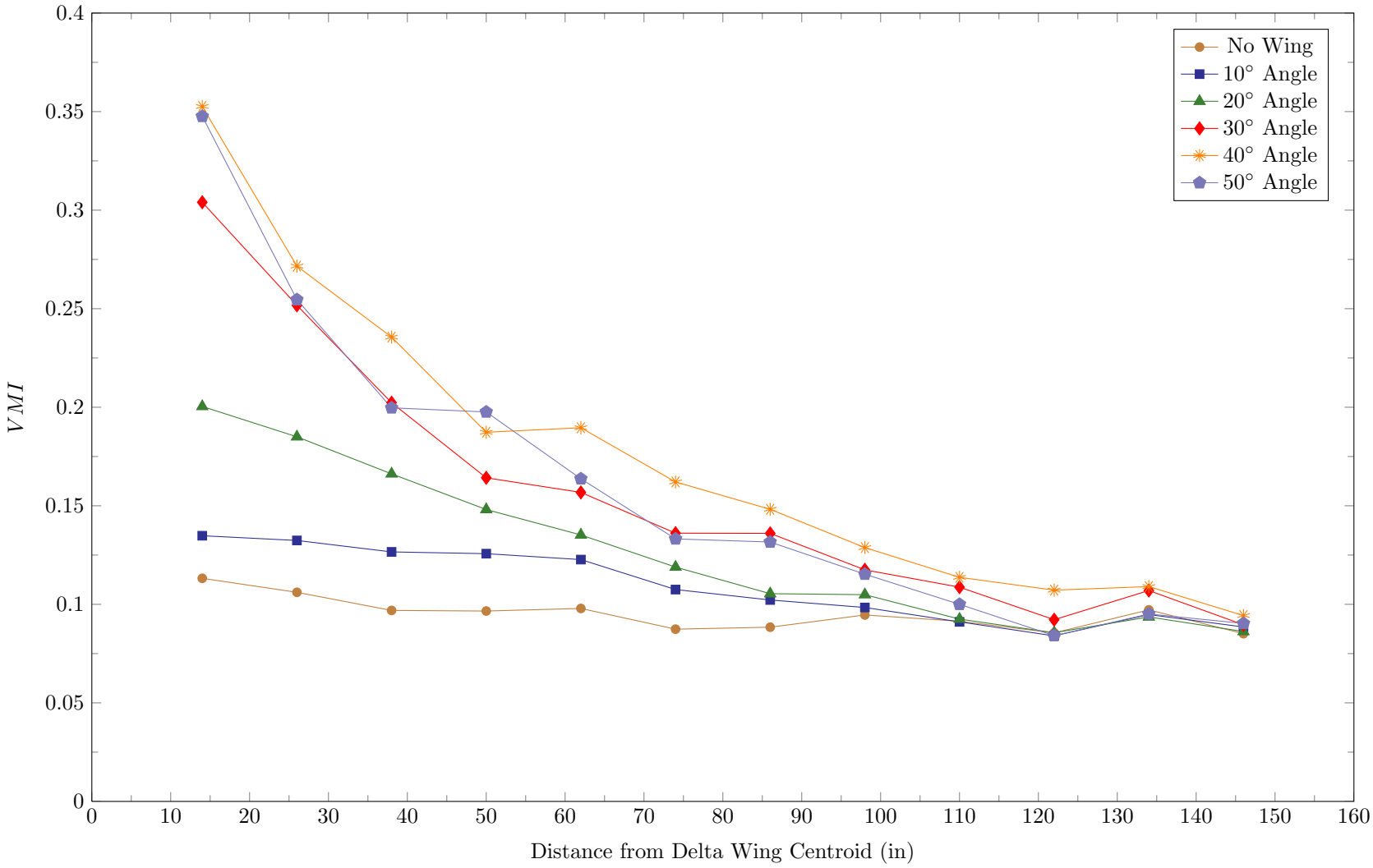

Fig. 4.25: Absolute VMI for five angles of attack and without Delta Wing as a function of distance from Delta Wing centroid location. The angle of 40° is optimal for sustained mixing up to twelve feet.

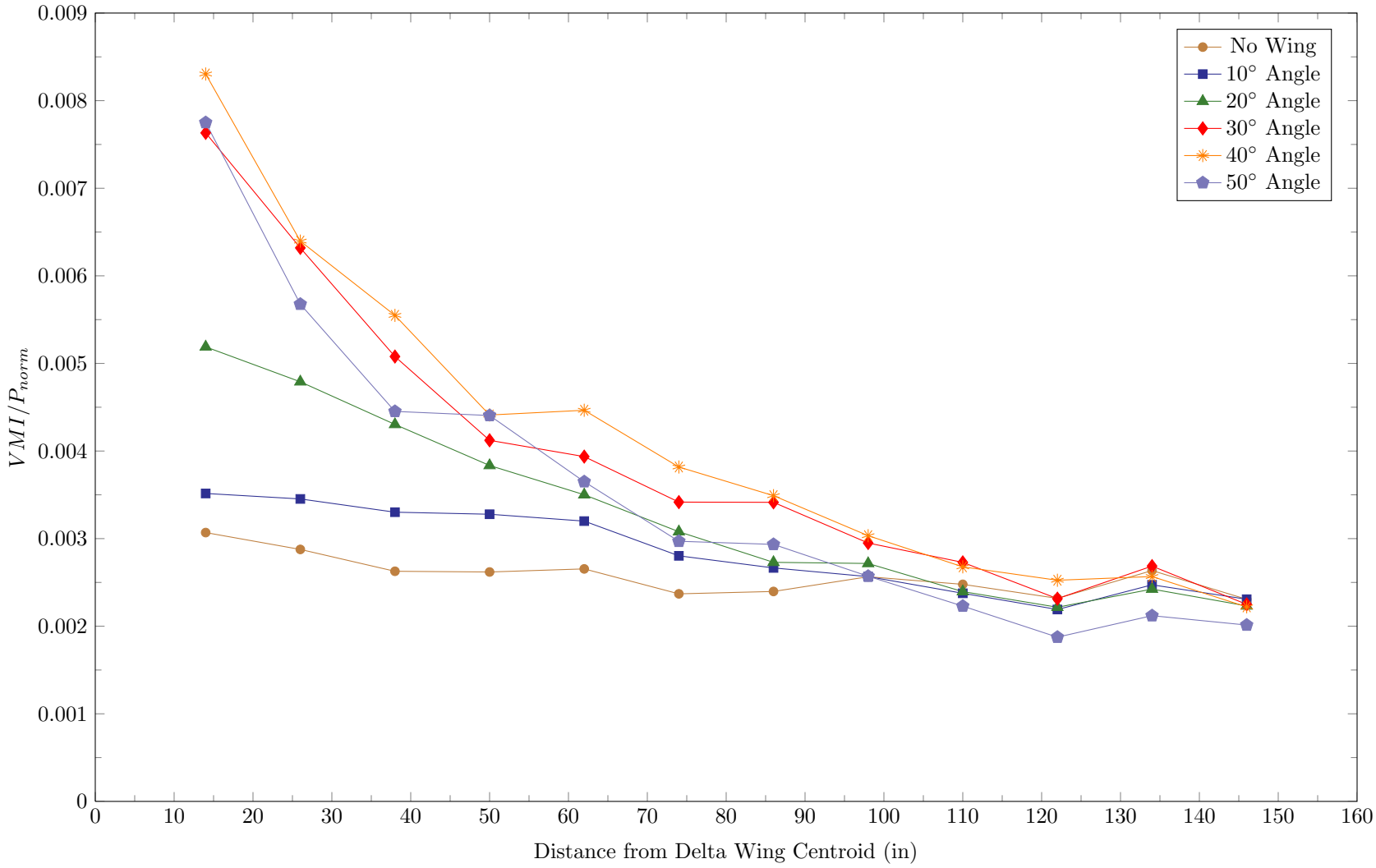

Fig. 4.26: Power-normalized VMI for five angles of attack and without Delta Wing as a function of distance from Delta Wing centroid location. Again, the angle of 40° is optimal for sustained mixing up to twelve feet.

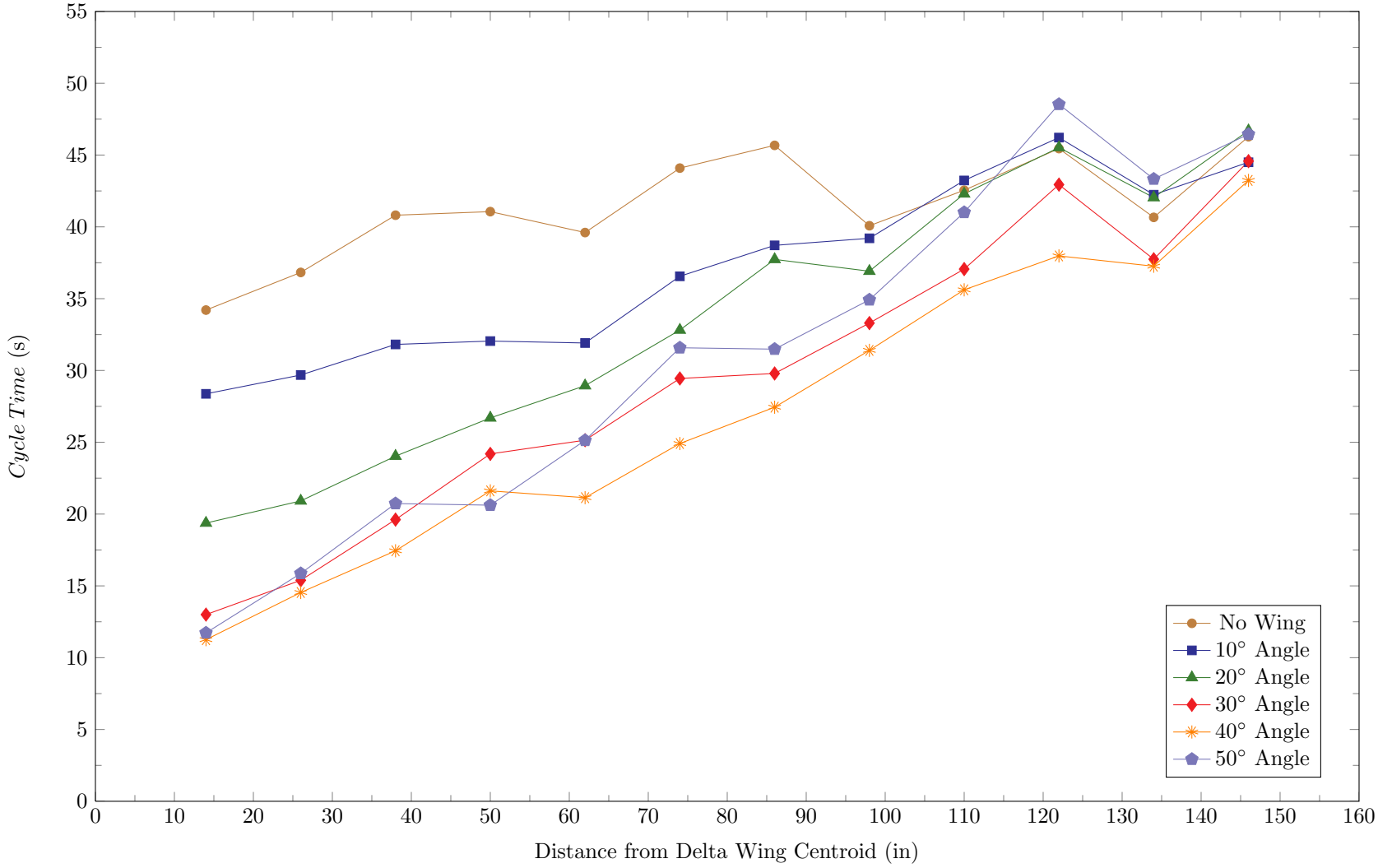

Fig. 4.27: Absolute Cycle Time for five angles of attack and without Delta Wing as a function of distance from Delta Wing centroid location. The 40° angle is optimal for the lowest Cycle Times.

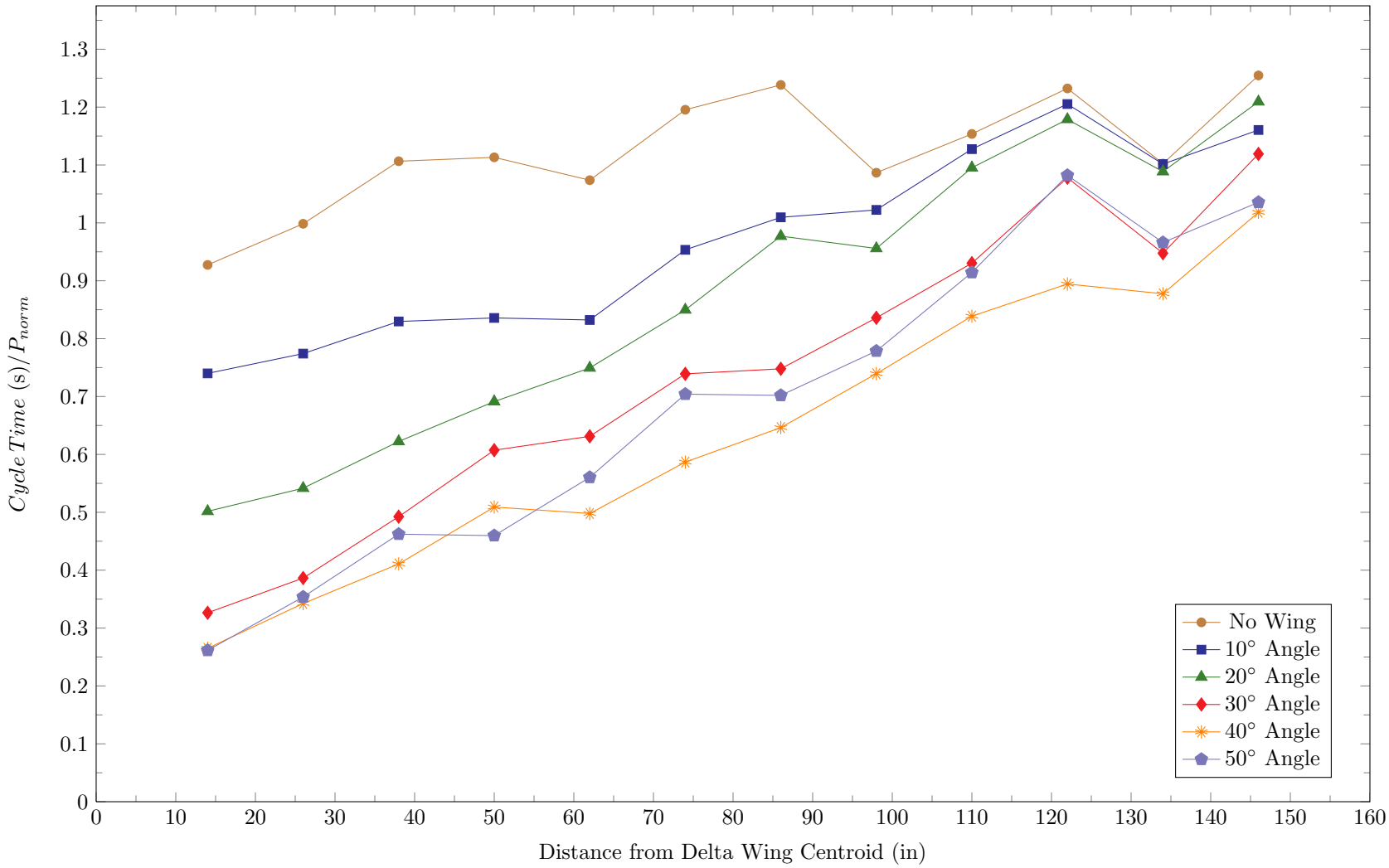

Fig. 4.28: Power-normalized Cycle Time for five angles of attack and without Delta Wing as a function of distance from Delta Wing centroid location. Again, the 40° angle is optimal for the lowest Cycle Times.

The flow velocity for the optimal 40° angle at the closest measurement location to the DW, Plane 1, is shown in Fig. 4.29. As with the equivalent plots in the previous two studies, the contour colors show velocity magnitude and the superimposed vectors show the in-plane velocity. Compared to the 40° result in the Angle of Attack Study, the vortex centers are at mid-height since the DW centroid was raised to mid-height. Raising the DW centroid raised the vortex centers as desired so the flow structures experience minimal deformation.

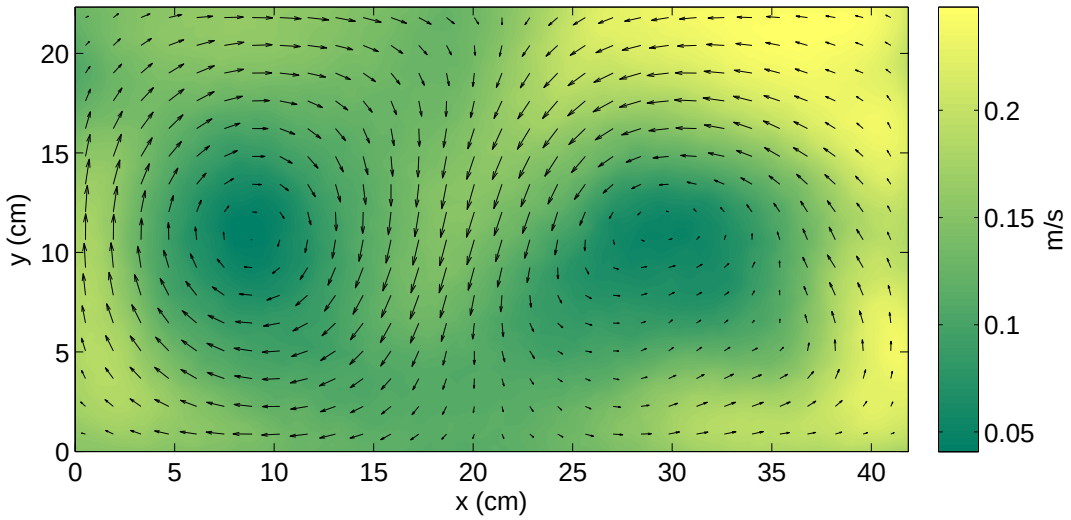

Fig. 4.29: Flow velocity for a 40° angle of attack at Plane 1

The in-plane velocity in Fig. 4.30 shows the typical two vortices. The maximum observed in-plane velocity is larger than in the Speed Study mainly due to the increase in angle of attack from 30° to 40°.

The Standard Deviation result in Fig. 4.31 shows relatively large values, even larger than the in-plane velocity. The area of maximum the SD is no longer at the vortex centers but is found in the high-velocity ring areas of the vortices. This suggests the proximity to the 180° bend causes the instantaneous vortex centers to traverse in a circular pattern around the point where their average is located.

The precision uncertainty and relative precision uncertainty in Fig. 4.32 and Fig. 4.33

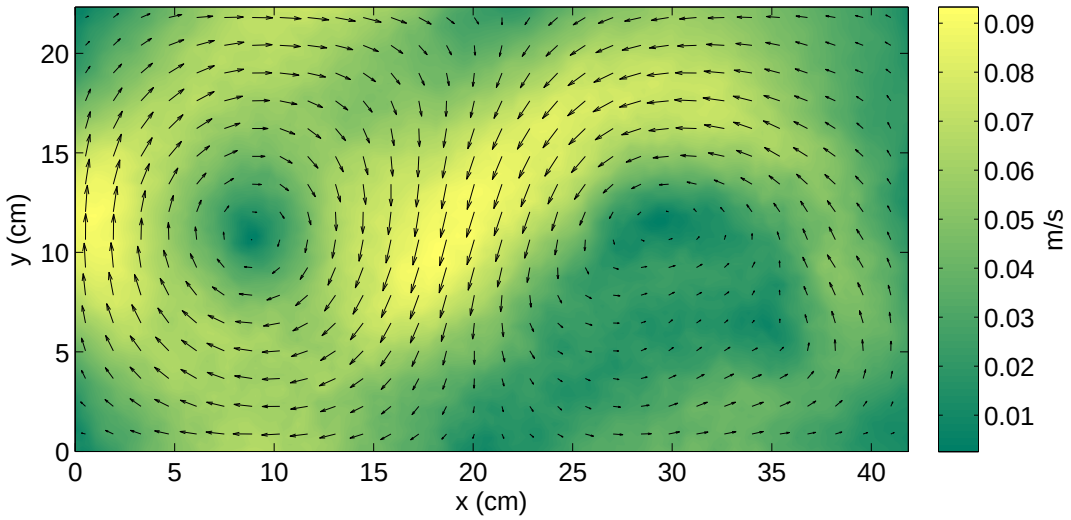

Fig. 4.30: In-plane flow velocity at Plane 1 for 40° angle of attack

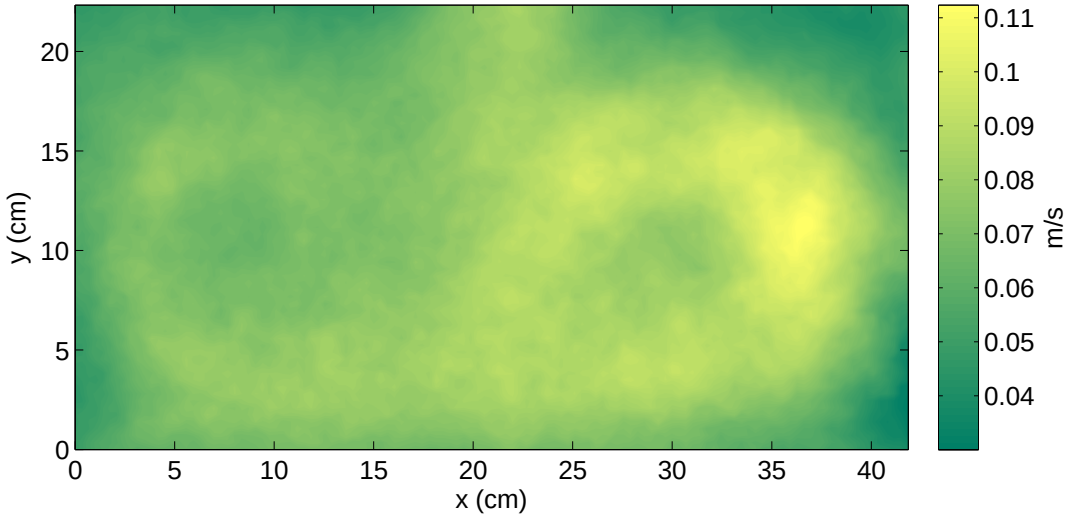

Fig. 4.31: Standard deviation of 200 instantaneous velocity fields at Plane 1 for 40° angle of attack

show areas of maximum values to be the same rings as above. The relative precision uncertainty is less than 13% everywhere. This result is higher than the previous two studies, likely due to the increased unsteadiness from the higher angle of attack and perhaps being much closer to the 180° bend.

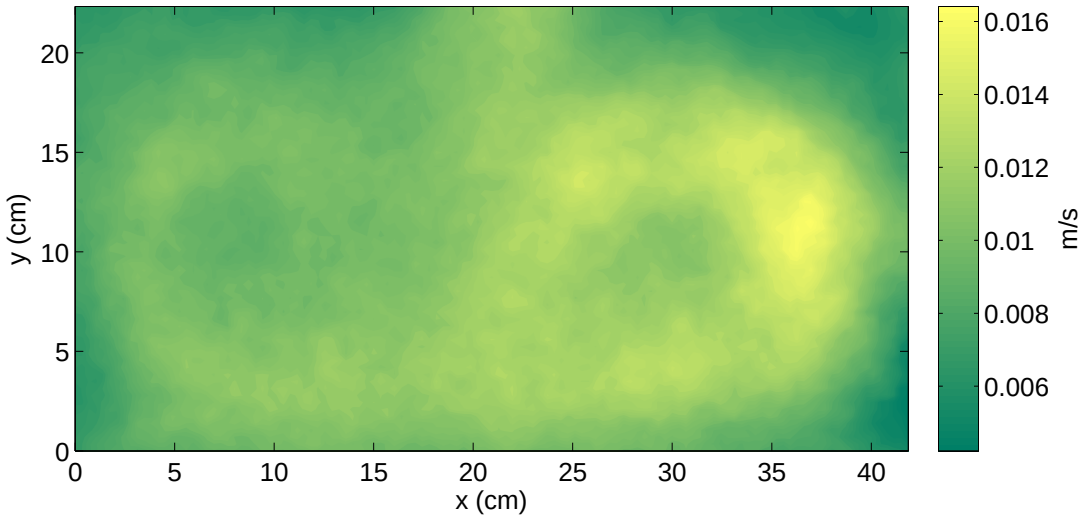

Fig. 4.32: Precision uncertainty of velocity at Plane 1 for 40° angle of attack

The turbulence kinetic energy and turbulence intensity in Fig. 4.34 and Fig. 4.35 are between the previous studies in magnitude but are relatively high since the streamwise velocity is 26% lower. The 40° angle and being near the 180° bend give significantly unsteady flow that is good for mixing, even with reduced streamwise velocity.

The two previous studies have shown clear optimal parameters. The Paddle-wheel Speed Study revealed that the VMI was not a function of the streamwise velocity, but the Cycle Time was. A choice was made to lower the speed to 7.19 RPM which is in the area of Fig. 4.4 that was at the edge of drastic reduction to Cycle Time. The Angle of Attack Study showed that 40° is optimal for both VMI and Cycle Time, both absolute and power-normalized. The Vortex Dissipation Study confirmed the expectation that the 40° angle is optimal for sustained mixing downstream. The optimal spacing from the results of this

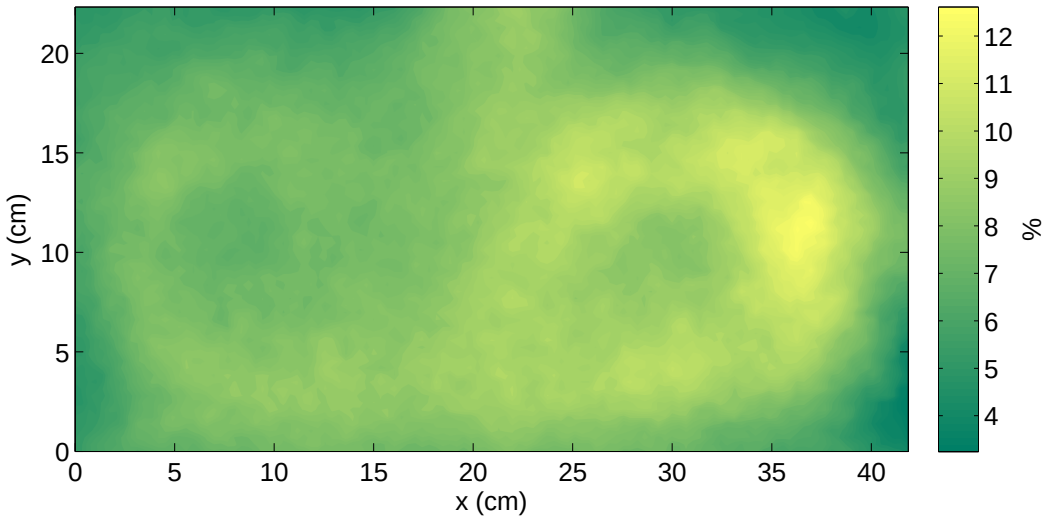

Fig. 4.33: Relative precision uncertainty of velocity at Plane 1 for 40° angle of attack

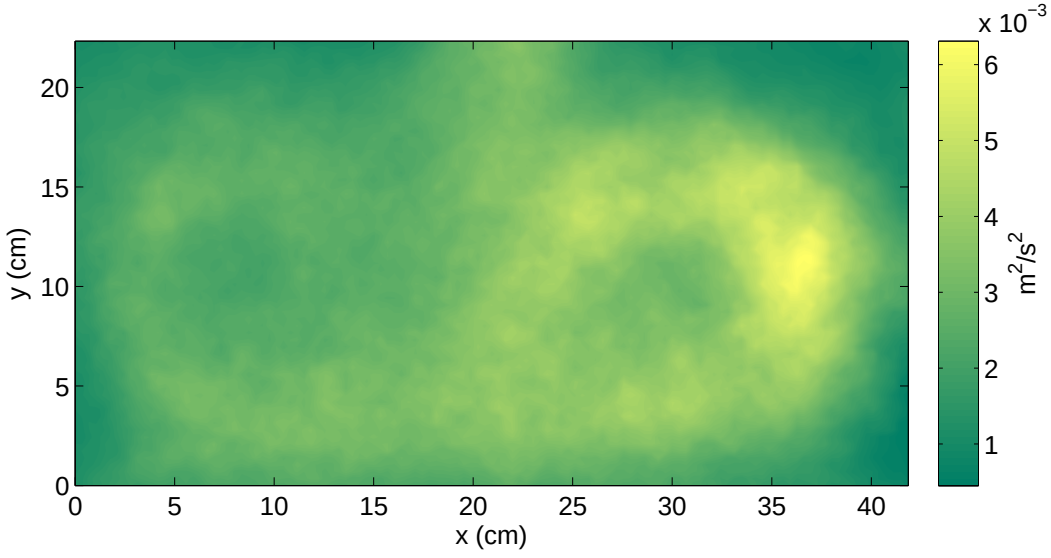

Fig. 4.34: Turbulence kinetic energy at Plane 1 for 40° angle of attack

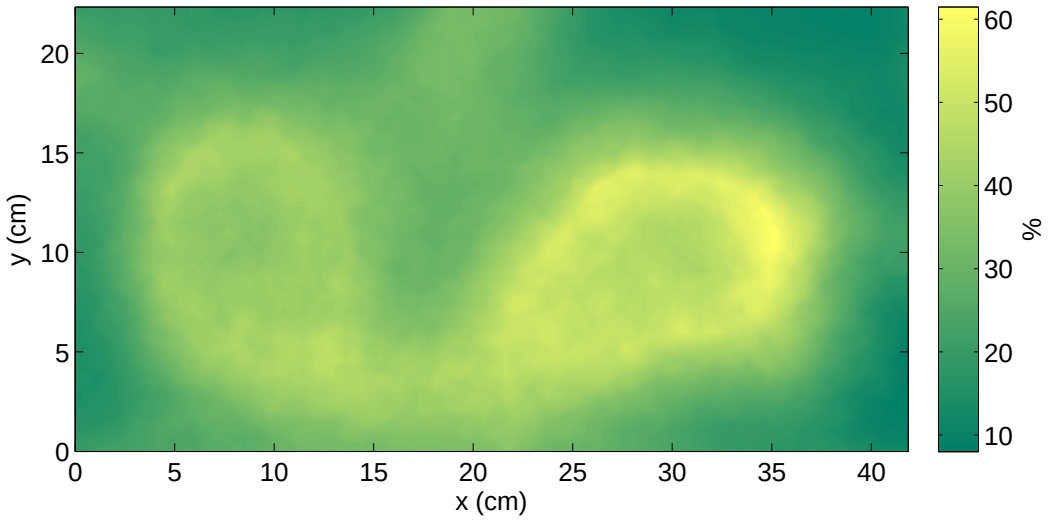

Fig. 4.35: Turbulence intensity at Plane 1 for 40° angle of attack

study is not obvious. An educated guess could be made on the results, but a quantitative study should reveal the best spacing. A more thorough study was conducted to determine the optimal spacing.

The Optimization Study on Delta Wing Spacing is found in Appendix D and determines the best DW spacing based on profit. The estimated value for dry algal biomass is $2.06/kg, assuming half is oil that can be used for biodiesel and half is protein that can be used to feed young fish. A raceway with equal dimensions to a study in [2] is used with 82 m length and 12 m width. Based on a growth experiment performed at Utah State University, it is thought that doubling the mixing with DWs may increase growth by 25%. This is very conservative compared to the study by Laws *et al.* which more than doubled algal growth by using airfoils, but is thought be more practical. Only the VMI from the optimal angle minus the baseline (no DW) VMI is considered since the raceway is likely to experience moderate VMI values without any DWs. Based on power measurements which showed using one DW added 1.5 W power at the paddle-wheel at a low-end speed, each DW is expected conservatively expected to add 2 W. Also, each DW with mounting hardware is

expected to cost $20 and should last for seven years. Since a commercial raceway is expected to have a similar depth to ours with ten inches of water, the same size of DW is expected which allows for transverse spacing of the width W of the raceway (see Fig. 4.36) of eighteen inches, or around 0.5 m. The raceway under consideration would have 12 DWs across each channel at every location, so the power and capital costs were scaled appropriately. The revenue, cost, and profit were calculated as a function of the spacing as

$$Profit(\Delta z) = Revenue(\Delta z) - Cost(\Delta z) \tag{4.1}$$

and were plotted as seen in Appendix D. The maximum profit was found at a spacing of 65 inches with an estimated increase in income of $5340/yr. The increase in VMI is nearly two-fold over the baseline, so the increase in growth and in profit could easily be 25%. This is a significant advantage in profit by the use of DWs at their optimal angle and spacing.

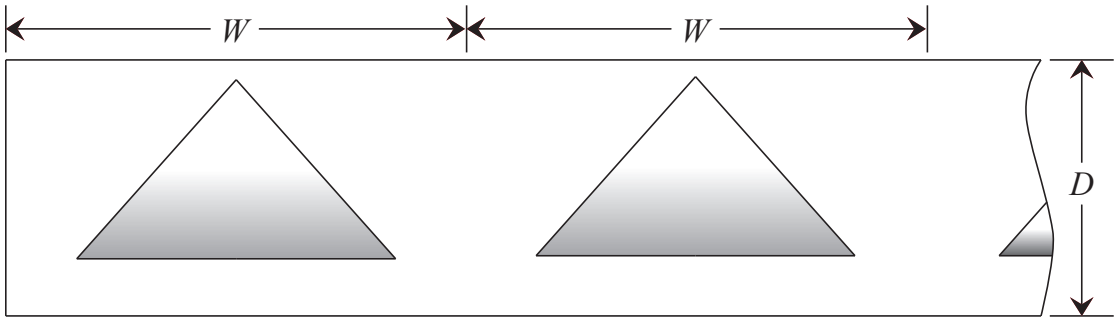

Fig. 4.36: Delta Wing transverse spacing in commercial raceways with arrays of wings

4.5 Comparison of PIV and ADV Data

The data from the PIV and ADV measurements systems are compared herein. Both measurement techniques are relatively new and require best practices for reliable results. The comparison was performed to co-validate the measurements using matched flow conditions. The results are very close when using the same measurement domain but differ significantly otherwise. The ADV data were provided by another graduate student at Utah

State University [24]. The ADV gives three components of velocity in a small measurement volume approximately two inches below the tip of the probe. Time restrictions allowed only for a 9x9 grid of measurements in each plane, compared to the approximately 128x72 measurements for PIV. The ADV is unable to acquire data near the boundaries of the domain, approximately one inch in from the sides due to its size limitations. and two inches from the top since the probe must remain submersed. The PIV data were cropped to coincide with the ADV measurement domain. This effect is represented in Fig. 4.37(a) compared with Fig. 4.37(b) and Fig. 4.38(a) compared with Fig. 4.38(b) with the ADV and PIV data for the same flow parameters. The plots are in-plane velocity about 18 inches downstream of a DW at 30° near the center of the raceway with eight inches of water. Note the absence of the high-velocity motion in the ADV domain which may cause it to underpredict the VMI and other flow characteristics. Also notice the similarities in the flow characteristics including the vortex center locations. Particle Image Velocimetry should be used over ADV when spacial resolution and data near the boundaries are important.

Though the full sampling domains are different, the PIV data were cropped to provide good agreement in the comparison study. This study was performed with matched parameters that are the same mentioned for the domain comparison. The results for Mean Velocity, standard deviation, turbulence kinetic energy, and turbulence intensity are shown in Table 4.2 & 4.3. The comparison is relatively close considering that the measurement technologies are radically different. The mean velocities are within 3%. Note that PIV over-predicts SD, TKE, and turbulence intensity in cases with and without the DW. This is likely due to PIV's susceptibility to noise that always increases SD results, and the other two quantities depend on SD. Therefore, if turbulence parameters are of high priority, the ADV should be chosen over PIV.

Contour plots for both PIV and ADV measurements are shown in Appendix E for matched parameters without and with the DW.

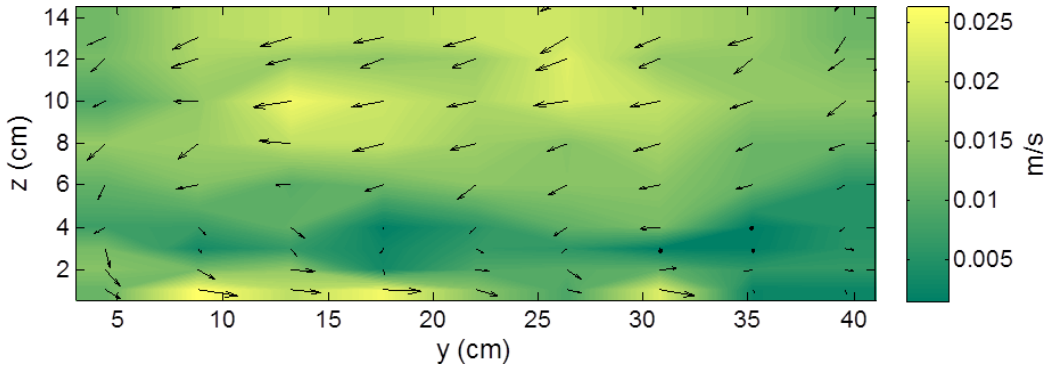

(a) Velocity plot without Delta Wing from ADV

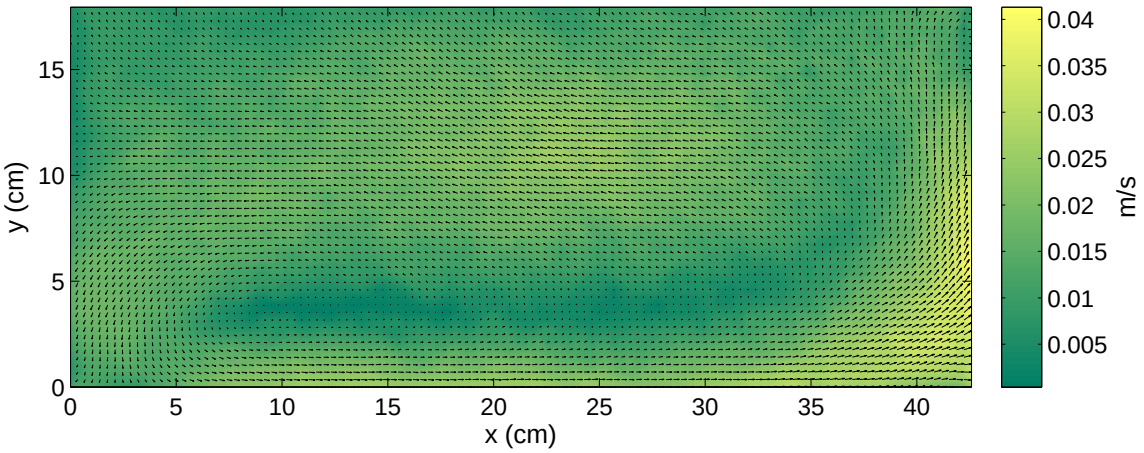

(b) Velocity plot without Delta Wing from PIV

Fig. 4.37: Plots illustrating the sample domain and spacial resolution difference between ADV and PIV. The PIV sample domain captures nearly the entire cross-section of the flow and has about 100x more velocity vectors. Plotted is the in-plane velocity in both images for flow without Delta Wing. Down-sampling of the PIV data has not been performed in this case.

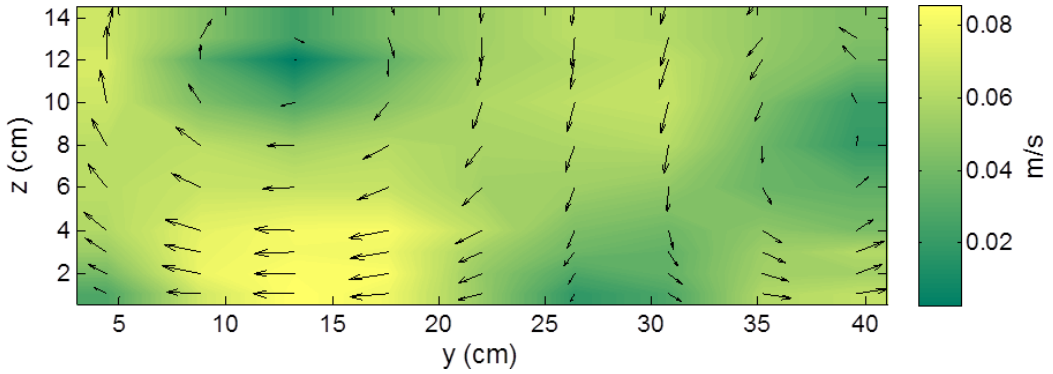

(a) Velocity plot with Delta Wing from ADV

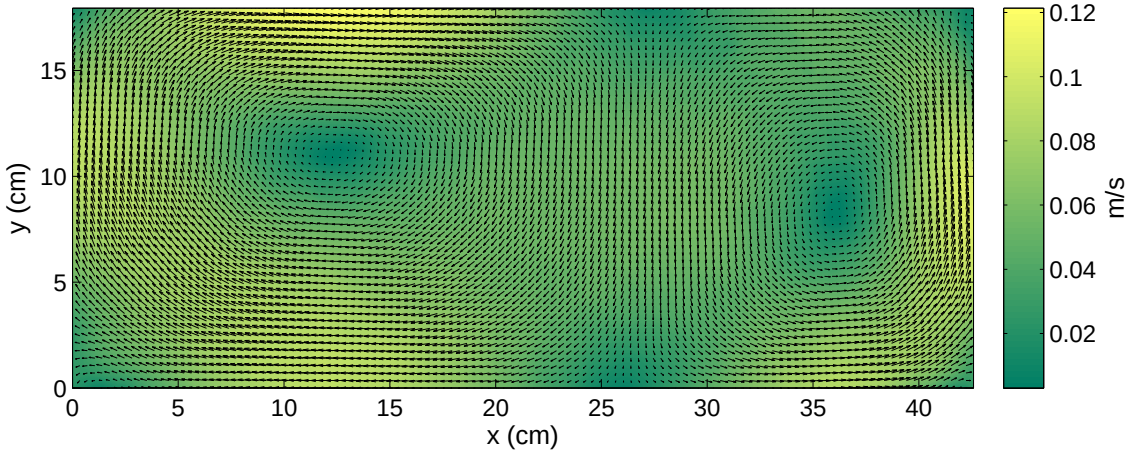

(b) Velocity plot with Delta Wing from PIV

Fig. 4.38: Plots illustrating the sample domain and spacial resolution difference between ADV and PIV. The PIV sample domain captures nearly the entire cross-section of the flow and has about 100x more velocity vectors. Plotted is the in-plane velocity in both images for flow with Delta Wing. Down-sampling of the PIV data has not been performed in this case.

Table 4.2: Summary of the PIV comparison to ADV without Delta Wing

Parameter	PIV	ADV	Difference (%)
Mean Velocity (m/s)	0.2458	0.2380	3.22
Standard Deviation (m/s)	0.0957	0.0887	7.59
In-plane Mean Velocity (m/s)	0.0152	0.0132	14.08
Turbulence Kinetic Energy (m^2/s^2)	0.0046	0.0040	13.95
Turbulence Intensity (%)	23.56	22.64	4.00

Table 4.3: Summary of the PIV comparison to ADV with Delta Wing

Parameter	PIV	ADV	Difference (%)
Mean Velocity (m/s)	0.2459	0.2493	1.37
Standard Deviation (m/s)	0.0988	0.0904	8.88
In-plane Mean Velocity (m/s)	0.0549	0.0533	2.96
Turbulence Kinetic Energy (m^2/s^2)	0.0049	0.0041	17.78
Turbulence Intensity (%)	21.40	23.73	10.33

Chapter 5

Conclusions & Future Work

5.1 Conclusions

Literature on algal growth and growth enhancements by mixing has been surveyed. Algae is a viable feedstock for biofuel production to both capture carbon from the atmosphere and help offset the use of traditional fuels. Raceway ponds are the most cost-effective means of growing algal biomass, but the process needs to be improved significantly to become competitive to traditional fuels. A common finding in literature is that an increase in the mixing of algal culture improves growth rates by up to a factor of two. Laws *et al.* have used airfoils at high angles of attack to double growth in experiments [13]. Cheng and Dugan used squares and an early form of the Delta Wing [15] and measured an increase in turbulence intensity. Some researchers have claimed that the increase in growth is due to the Flashing Light Effect, while others claim it is due to the decrease in the fluid boundary layer around cells that increases mass transfer [7]. Whatever the reason, the general consensus is that increased mixing in algal cultures increases growth.

These early studies used basic instruments that were limited to point measurements. With the increased capabilities of sensors and measurement systems today, a more thorough optimization study was performed to maximize vertical mixing by the use of DWs in an experimental algal raceway. This raceway was built in a laboratory environment for flow measurements using fresh-water. Power was also measured for each study since the addition of the DW was found to increase power consumption slightly. The power losses of the driving system were removed from consideration to isolate the power required to circulate the flow. Stereo PIV was used to measure three components of velocity in entire cross-sections of the flow. This method proved very effective at measuring flow conditions quickly, but was challenging to set-up for accurate results. Existing quantities of interest were

defined: standard deviation, turbulence kinetic energy, turbulence intensity, and precision uncertainty. New quantities were also defined for the Vertical Mixing Index and Cycle Time. The flow measurements were analyzed with a computer code for all quantities with contour plots for the field results.

Three studies were performed with these methods: The Paddle-wheel Speed Study, the Angle of Attack Study, and the Vortex Dissipation Study. The Paddle-wheel Speed Study showed VMI is not a function of streamwise velocity. It also showed the Cycle Time is a useful estimate of the time required for an alga cell to complete a cycle from the bottom, to the top, and back to the bottom of the raceway. The speed was decreased from these results, using half the power of other experiments in the same facility [24]. The Angle of Attack study revealed a clear, optimal angle of 40° for both VMI and Cycle Time considerations. From the results of these two studies, the power was found to be a strong function of paddle-wheel speed and not a strong function of angle of attack. The Vortex Dissipation Study revealed the length of enhanced mixing was sustained downstream of the DW for twelve feet for five angles of attack. As with the Angle of Attack Study, the optimal angle is 40°; but the dissipation study confirmed it remained optimal for then entire measured length downstream. The optimal spacing was not clear without a separate study, which was performed and gave 65 inches as optimal for profit considering the added power and capital costs of adding arrays of DWs to a commercial raceway.

A separate study was performed to compare results between the PIV measurement system and those acquired by another student using an Acoustic Doppler Velocimeter with matching flow conditions. The ADV makes point measurements, which often results is lower spacial resolution than PIV. Also the side and top boundary cannot be measured with this system. The results for the mean velocity were within 3% while the standard deviation, turbulence kinetic energy, and turbulence intensity were all overestimated by PIV with moderate levels. It is believed that PIV is better suited where mean velocity results and spacial resolution are desired but that the ADV gives greater accuracy for fluctuating quantities.

5.2 Future Work

The significant factor that is missing in this work is whether these optimized parameters will in fact increase algal growth in raceways. A recent growth experiment at Utah State University found that adding two DWs to a small raceway at 30° angle of attack increased growth by 25%, but it has not been successfully repeated. Nevertheless, growth studies will be performed using the optimal parameters for the paddle-wheel speed, angle of attack, and spacing.

While the optimal Angle of Attack of 40° and the DW spacing can be directly translated to the commercial scale raceways with similar geometry, the optimal paddle-wheel speed can not. Considering ways to identify the optimal speed that could scale properly is very desirable so growers could apply all of the optimal results easily. If this could be done, the real impact of the DW on algal growth could be seen in lower production costs and increased growth yields.

References

[1] Wijffels, R. H. and Barbosa, M. J., "An Outlook on Microalgal Biofuels," *Science*, Vol. 329, No. 5993, Aug. 2010, pp. 796–799.

[2] Chisti, Y., "Biodiesel from Microalgae," *Biotechnology Advances*, Vol. 25, No. 3, May-Jun. 2007, pp. 294–306.

[3] Batan, L., Quinn, J., Willson, B., and Bradley, T., "Net Energy and Greenhouse Gas Emission Evaluation of Biodiesel Derived from Microalgae," *Environmental Science & Technology*, Vol. 44, No. 20, Oct. 2010, pp. 7975–7980.

[4] Vonshak, A., Torzillo, G., and Tomaseli, L., "Use of Chlorophyll Fluorescence to Estimate the Effect of Photoinhibition in Outdoor Cultures of Spirulina-Platensis," *Journal of Applied Phycology*, Vol. 6, No. 1, Feb. 1994, pp. 31–34.

[5] Davis, R., Aden, A., and Pienkos, P. T., "Techno-economic Analysis of Autotrophic Microalgae for Fuel Production," *Applied Energy*, Vol. 88, No. 10, SI, Oct. 2011, pp. 3524–3531.

[6] Singh, R. N. and Sharma, S., "Development of Suitable Photobioreactor for Algae Production - A Review," *Renewable and Sustainable Energy Reviews*, Vol. 16, No. 4, 2012, pp. 2347 – 2353.

[7] Terry, K., "Photosynthesis in Modulated Light - Quantitative Dependence of Photosynthetic Enhancement on Flashing Rate," *Biotechnology and Bioengineering*, Vol. 28, No. 7, Jul. 1986, pp. 988–995.

[8] Quinn, J., de Winter, L., and Bradley, T., "Microalgae Bulk Growth Model with Application to Industrial Scale Systems," *Bioresource Technology*, Vol. 102, No. 8, Apr. 2011, pp. 5083–5092.

[9] Phillips, J. N. Jr., and Myers, J., "Growth Rate of Chlorella in Flashing Light," *Plant Physiology*, Vol. 29, No. 2, 1954, pp. 152–161.

[10] Seibert, M. and Lavorel, J., "Oxygen-Evolution Patterns from Oxygen-Evolving Photosystem II Particles," *Solar Energy Research Institute Biomass Program Principal Investigators' Review Meeting*, 1982, pp. 17.

[11] Miller, R. L., Fredrickson, A. G., Brown, A. H., and Tsuchiya, H. M., "Hydromechanical Method to Increase Efficiency of Algal Photosynthesis," *Industrial and Engineering Chemistry Process Design and Development*, Vol. 3, No. 2, 1964, pp. 134–143.

[12] James, S. C. and Boriah, V., "Modeling Algae Growth in an Open-Channel Raceway," *Journal of Computational Biology*, Vol. 17, No. 7, Jul. 2010, pp. 895–906.

[13] Laws, E., Terry, K., Wickman, J., and Chalup, M., "A Simple Algal Production System Designed to Utilize the Flashing Light Effect," *Biotechnology and Bioengineering*, Vol. 25, No. 10, 1983, pp. 2319–2335.

[14] Biswas, G., Chattopadhyay, H., and Sinha, A., "Augmentation of Heat Transfer by Creation of Streamwise Longitudinal Vortices Using Vortex Generators," *Heat Transfer Engineering*, Vol. 33, No. 4-5, 2012, pp. 406–424.

[15] Cheng, E. and Dugan, G., "Low-Energy Mixing in Algal Culture Raceways," *Journal of Energy Engineering-ASCE*, Vol. 121, No. 3, Dec. 1995, pp. 100–107.

[16] Grobbelaar, J., "The Influence of Light/Dark Cycles in Mixed Algal Cultures on Their Productivity," *Bioresource Technology*, Vol. 38, No. 2-3, 1991, pp. 189–194.

[17] Elgerd, O. I., *Basic Electric Power Engineering*, Addison-Wesley Publishing Company, Reading, Massachusetts, 1977.

[18] LaVision, *DaVis® version 7.2*, Goettingen, Germany, http://www.lavision.de/en/techniques/piv.php.

[19] Cengel, Y. A., Cimbala, J. M., and Kanoglu, M., *Fluid Mechanics: Fundamentals and Applications*, Vol. 6, McGraw-Hill Higher Education New York, 2006.

[20] Scheimpflug, T., "Improved Method and Apparatus for the Systematic Alteration or Distortion of Plane Pictures and Images by Means of Lenses and Mirrors for Photography and for Other Purposes," British Patent 1196, 1904.

[21] Raffel, M., Willert, C., Wereley, S., and Kompenhans, J., *Particle Image Velocimetry: A Practical Guide*, Springer, New York, NY, 2007.

[22] Coleman, H. W. and Steele, W. G., *Experimentation, Validation, and Uncertainty Analysis for Engineers*, John Wiley and Sons, Hoboken, NJ, 2009.

[23] Kays, W. M., Crawford, M. E., and Weigand, B., *Convective Heat and Mass Transfer*, Vol. 4, McGraw-Hill Higher Education New York, 2005.

[24] Voleti, R., *Experimental Studies of Vertical Mixing in an Open Channel Raceway for Algae Biofuel Production*, Master's thesis, Mechanical & Aerospace Engineering, Utah State University, Logan UT, 2012.

[25] Janna, W. S., *Design of Fluid Thermal Systems*, Cengage Learning, Stamford, Connecticut, 2011.

Appendices

Appendix A

FORTRAN Code to Reorganize Data

```
PROGRAM ReadDATWriteVxVyVzProgram

! This program will take the processed PIV data from a TecPlot .dat file, ...
    arrange it into arrays
!   Vx, Vy, Vz and write to individual files
!       Revision: the program will also calculate the pixel scale and output ...
    to another file
!
! Author:  Blake Lance
! Date:  9 March 2012
!   **Some code structure was taken from TecplotReadWrite codes

IMPLICIT NONE

! Data Dictionary
INTEGER :: n = 0        ! Count of Lines in Tecplot File
INTEGER :: NN           ! Number of .dat files to tranform
INTEGER :: i, j, k, m   ! Do-loop indeces
INTEGER :: sizeX        ! Count Number of X vectors
INTEGER :: sizeY        ! Count Number of Y vectors
INTEGER :: header = 3   ! Number of Header Lines
INTEGER :: x, y, comma
INTEGER :: error1       ! IOSTAT error for opening existing file
INTEGER :: error2       ! IOSTAT error for opening file
INTEGER :: error3       ! IOSTAT error for opening file
INTEGER :: error4       ! IOSTAT error for opening file
INTEGER :: error5       ! IOSTAT error for opening file
INTEGER :: readerror    ! Read Error
CHARACTER(len=40)  :: filein            ! user-defined filename
CHARACTER(len=100) :: dummy             ! dummy variable to allow data to be ...
    read
CHARACTER(len=10)  :: xdum, ydum        ! mode dummies
CHARACTER(len=5)   :: kstring           ! the value of k in a string
REAL :: PixScale    ! the pixel scale (pixels/mm)
REAL, DIMENSION(:,:), ALLOCATABLE :: Vx ! velocity in x-direction
REAL, DIMENSION(:,:), ALLOCATABLE :: Vy ! velocity in y-direction
REAL, DIMENSION(:,:), ALLOCATABLE :: Vz ! velocity in y-direction
REAL, DIMENSION(:), ALLOCATABLE :: xstore, ystore, ustore, vstore, wstore
!-----------------------------------------------------------------------------------------------

! Explanation to the user
WRITE (*,*)
WRITE (*,*) 'This program will take the processed PIV data from a set of ...
    TecPlot .dat'
```

```
41 WRITE (*,*) 'files, arrange them into arrays Vx, Vy, Vz and write to ...
       individual files.'
42 WRITE (*,*)
43
44 ! Ask user for file
45 WRITE (*,*) 'Please enter the name of the TecPlot data folder not including ...
       the subfolder DATfiles'
46 WRITE (*,*)
47 READ (*,*) filein
48 WRITE (*,*)
49
50 ! Ask user for number of files
51 WRITE (*,*) 'Please enter the number of the TecPlot data files in the batch'
52 WRITE (*,*)
53 READ (*,*) NN
54 WRITE (*,*)
55 !-----------------------------------------------------------------------------------------------
56
57 ! Size the first file, and all others in the batch should have the same size.
58 OPEN(UNIT=10, file=TRIM(filein)//'\DATfiles\B00001.dat', STATUS='OLD', ...
       ACTION='READ', IOSTAT=error1)
59 OPEN(UNIT=50, file=TRIM(filein)//'\DATfiles\'//TRIM(filein)//'_PixScale.dat',&
60      STATUS='REPLACE', ACTION='WRITE', IOSTAT=error5)
61
62 DO  ! Get File Size
63   READ(10,*,IOSTAT=readerror) dummy
64   IF ( readerror /= 0) EXIT
65   n = n + 1
66 END DO
67 REWIND(10)
68
69 n = n - header  ! Subtract Header Lines
70 ALLOCATE( xstore(n), ystore(n), ustore(n), vstore(n), wstore(n) )
71
72 !-----------------------------------------------------------------------------------------------
73 ! Obtain the size of the data
74 ! Info is Located on Last Line of Headers
75 ! Example: <ZONE T="Frame 0", I=116, J=137, K=1>
76
77 DO m = 1, (header-1)    !Skip middle of header
78   READ(10,*) dummy
79   WRITE(*,*) dummy
80 END DO
81
82 READ(10,'(A)') dummy
83 x = INDEX(dummy,'I')
84 y = INDEX(dummy,'J')
85 xdum = dummy(x:x+10)
86 ydum = dummy(y:y+10)
87 comma = INDEX(xdum, ',')
88 xdum = xdum(3:comma-1)
89 comma = INDEX(ydum, ',')
90 IF (comma == 0) THEN
91   comma = 10
92 END IF
93 ydum = ydum(3:comma-1)
```

```
94
95  READ(xdum,*) sizeX
96  READ(ydum,*) sizeY
97
98  ! Now that we know the size of the data, we can allocate arrays to store the ...
        data
99  ALLOCATE( Vx(sizeX, sizeY) )
100 ALLOCATE( Vy(sizeX, sizeY) )
101 ALLOCATE( Vz(sizeX, sizeY) )
102
103 WRITE (*,110) sizeX, sizeY
104 110 FORMAT(1x, 'The data has ', I5, ' vectors in a row and ', I5, ' in a ...
        column.')
105 WRITE (*,*)
106
107 !-----------------------------------------------------------------------------------------
108
109 DO i = 1,2  ! Read first two rows of data
110   READ(10,*, IOSTAT=readerror) xstore(i)
111 END DO
112
113 ! Calculate the pixel scale by the difference in the first two x-coordinates
114 PixScale = ABS( xstore(1) - xstore(2) )
115 WRITE(50,*) PixScale
116
117 CLOSE(10); CLOSE(50)
118
119 !-----------------------------------------------------------------------------------------
120
121 DO k = 1,NN ! Repeat for each file
122   ! Open files
123   IF (k < 10) THEN  ! pad kstring with leading zeros
124     WRITE( kstring,'(I1)' ) k
125     kstring = '0000'//TRIM(kstring)
126   ELSE IF (k < 100) THEN
127     WRITE( kstring,'(I2)' ) k
128     kstring = '000'//TRIM(kstring)
129   ELSE IF (k < 1000) THEN
130     WRITE( kstring,'(I3)' ) k
131     kstring = '00'//TRIM(kstring)
132   ELSE IF (k < 10000) THEN
133     WRITE( kstring,'(I4)' ) k
134     kstring = '0'//TRIM(kstring)
135   ELSE IF (k < 100000) THEN
136     WRITE( kstring,'(I5)' ) k
137     kstring = TRIM(kstring)
138   ELSE
139     WRITE(*,*) "k > 99999"
140   END IF
141
142   WRITE(*,*) kstring
143
144   OPEN(UNIT=10, file=TRIM(filein)//'\DATfiles\B'//TRIM(kstring)//'.dat', ...
          STATUS='OLD', ACTION='READ', IOSTAT=error1)
145   OPEN(UNIT=20, ...
          file=TRIM(filein)//'\DATfiles\'//TRIM(filein)//'_Vx_'//TRIM(kstring)//'.dat',&
```

```
146       STATUS='REPLACE', ACTION='WRITE', IOSTAT=error2)
147     OPEN(UNIT=30, ...
            file=TRIM(filein)//'\DATfiles\'//TRIM(filein)//'_Vy_'//TRIM(kstring)//'.dat',&
148       STATUS='REPLACE', ACTION='WRITE', IOSTAT=error3)
149     OPEN(UNIT=40, ...
            file=TRIM(filein)//'\DATfiles\'//TRIM(filein)//'_Vz_'//TRIM(kstring)//'.dat',&
150       STATUS='REPLACE', ACTION='WRITE', IOSTAT=error4)
151
152     !-------------------------------------------------------------------------------------------
153
154     IF ( error1 == 0 .AND. error2 == 0 .AND. error3 == 0 .AND. error4 == 0 ) ...
            THEN ! files opened properly
155       DO m=1,header   ! Skip the header
156         READ(10,*,IOSTAT=readerror) dummy
157       END DO
158
159       DO i = 1,n  ! Read Data
160         READ(10,*, IOSTAT=readerror) xstore(i), dummy, dummy, ustore(i), ...
                vstore(i), wstore(i)
161       END DO
162
163       ! Fill Up 2D Arrays
164       n = 1
165       DO j = 1, sizeY
166         DO i = 1, sizeX   ! The Tecplot file from DaVis begins at upper left ...
              writing row by row (like reading)
167           Vx(i,j) = ustore(n)
168           Vy(i,j) = vstore(n)
169           Vz(i,j) = wstore(n)
170           n = n + 1
171         END DO
172       END DO
173       !-------------------------------------------------------------------------------------------
174
175       DO j=1,sizeY
176         WRITE(20,*) Vx(:,j)
177         WRITE(30,*) Vy(:,j)
178         WRITE(40,*) Vz(:,j)
179       END DO
180
181       CLOSE (10); CLOSE (20); CLOSE (30); CLOSE (40)
182     ELSE
183       WRITE (*,*) 'An error occured opening the file(s)'
184       WRITE (*,*)
185     END IF
186   END DO
187
188   WRITE(*,*)
189   WRITE(*,*) 'The files are written for ', TRIM(filein)
190   WRITE(*,*)
191
192   END PROGRAM ReadDATWriteVxVyVzProgram
```

Appendix B

Matlab Code to Analyze and Plot PIV Data

```
tic;    close all;   clear all;   clc;

%% Raceway.m program
% This code will perform all the data analysis on the Raceway data sets
% including Average, RMS, Turbulence Kinetic Energy, Turbulence Intensity,
% Precision Uncertainty fields as well as the VMI and Cycle Time
% quantities.  It will also perform plotting for the field results and
% uses the TrimToMask function.  The Average and RMS portions of the code
% are modified from Ben Timmins' uncertainty_check.m code.

% Author:   Blake Lance
% Date:     30 July 2012

%% Code Parameters
project = 'Plane02';
input = '50deg';  % The input data
N = 200;     % Number of files to read
Depth = 0.254;  % Water depth for CycleTime calculation in meters
TrimType = 0;    % 0 for PIV and 1 for ADV
Plotting = 0;    % 0 for no plots and 1 for plots
SavePlot = 0;    % 0 to not save and 1 to save plots
Format = '.pdf';% file format to save data
ReduceFactor = 4;   % the factor by which in-plane velocity vectors should be
                        % reduced in each dimension (use integers, can be 1)
if strcmp(project,'Plane7')  % Since Plane7 had only 8" of water, use ...
    shorter paper
    PaperHeight = 3.5;
else
    PaperHeight = 4.5;
end

%% Initialize
Vz_mean = zeros(N,1);   VMI = zeros(N,1);   CycleTime = zeros(N,1);

%% Adaptive trimming of masked areas using TrimToMask Function
temp = ...
    importdata([pwd,'\',project,'\',input,'\','DATfiles','\',input,'_Vx_00001.dat']);

nx = size(temp,2);
ny = size(temp,1);
[imin,imax,jmin,jmax] = TrimToMask( temp );

% Set Scales
```

```
PixScale = ...
    importdata([pwd,'\',project,'\',input,'\','DATfiles','\',input,'_PixScale.dat']);
PixScale = 0.1*PixScale;  %Scale from the default mm to cm
x = 0.:PixScale:PixScale*(nx-1.);
y = PixScale*(ny-1.):-PixScale:0.;  % Define y and i origins to be at bottom

% Trim the boundaries
if TrimType == 0    % Trim to fit PIV domain
    TrimTop = 4;
    TrimBottom = 4;
    TrimWidth = 4;
    xAxisShift = 0;
    yAxisShift = 0;
elseif TrimType == 1    % Trim to fit ADV domain
    TrimTop = 15;
    TrimBottom = 4;
    TrimWidth = 10;
    xAxisShift = 3;
    yAxisShift = 0.5;
end

% iupper is the y index at the upper boundary (lowest index)
ilower = imin - TrimBottom;

% ilower is the y index at the lower boundary (highest index)
iupper = imax + TrimTop;

jlower = jmin + TrimWidth;
jupper = jmax - TrimWidth;

xlower = x(jlower);
xupper = x(jupper);
ylower = y(ilower);
yupper = y(iupper);

x = x - xlower + xAxisShift; % Shift to have origin at corner of plot
y = y - ylower + yAxisShift;

%% Allocate new 3D arrays
Vx(1:ny,1:nx,1:N) = NaN;
Vy(1:ny,1:nx,1:N) = NaN;
Vz(1:ny,1:nx,1:N) = NaN;

%% Run through outer loop and read in the data files
for k=1:N   % Start outer loop at beginning

    if( k < 10 )
        istring = ['0000',int2str(k)];
    elseif( k < 100 )
        istring = ['000',int2str(k)];
    elseif( k < 1000 )
        istring = ['00',int2str(k)];
    elseif( k < 10000 )
        istring = ['0',int2str(k)];
    elseif( k < 100000 )
        istring = int2str(k);
```

```
97      else
98          fprintf(' i > 99999');
99      end
100
101     Vx(:,:,k) = ...
            importdata([pwd,'\',project,'\',input,'\','DATfiles','\',input,'_Vx_',istring,'.dat']);
102     Vy(:,:,k) = ...
            importdata([pwd,'\',project,'\',input,'\','DATfiles','\',input,'_Vy_',istring,'.dat']);
103     Vz(:,:,k) = ...
            importdata([pwd,'\',project,'\',input,'\','DATfiles','\',input,'_Vz_',istring,'.dat']);
104 end
105
106 %% Compute the average velocity field
107 n(1:ny,1:nx) = 0;
108 Vx_ave(1:ny,1:nx) = 0;
109 Vy_ave(1:ny,1:nx) = 0;
110 Vz_ave(1:ny,1:nx) = 0;
111
112 for k = 1:N
113     for j = 1:nx
114         for i = 1:ny
115             if (Vx(i,j,k) ~= 0 && Vy(i,j,k) ~= 0 && Vz(i,j,k) ~= 0)
116                 Vx_ave(i,j) = Vx_ave(i,j) + Vx(i,j,k);
117                 Vy_ave(i,j) = Vy_ave(i,j) + Vy(i,j,k);
118                 Vz_ave(i,j) = Vz_ave(i,j) + Vz(i,j,k);
119                 n(i,j) = n(i,j) + 1;    % denife n as the array of valid vectors
120             end
121         end
122     end
123 end
124 Vx_ave = Vx_ave./n;
125 Vy_ave = Vy_ave./n;
126 Vz_ave = Vz_ave./n;
127
128 %% Down-sample Vx_ave and Vy_ave if ReduceFactor > 1
129 if ReduceFactor > 1
130     TrimmedWindowsX = floor((jupper-jlower+1.)/ReduceFactor);
131     TrimmedWindowsY = floor((ilower-iupper+1.)/ReduceFactor);
132     x_lim_vectors = zeros(1,TrimmedWindowsX);
133     y_lim_vectors = zeros(1,TrimmedWindowsY);
134     Vx_ave_lim_vectors = zeros(TrimmedWindowsY,TrimmedWindowsX);
135     Vy_ave_lim_vectors = zeros(TrimmedWindowsY,TrimmedWindowsX);
136     for i = 1:TrimmedWindowsY
137         for j = 1:TrimmedWindowsX
138             x_lim_vectors(j) = ...
139                 mean(x((jlower+(j-1)*ReduceFactor):(jlower+j*ReduceFactor-1)));
140             y_lim_vectors(i) = ...
141                 mean(y((iupper+(i-1)*ReduceFactor):(iupper+i*ReduceFactor-1)));
142             Vx_ave_lim_vectors(i,j) = ...
143                 mean(mean(Vx_ave((iupper+(i-1)*ReduceFactor):(iupper+i*ReduceFactor-1),...
144                 (jlower+(j-1)*ReduceFactor):(jlower+j*ReduceFactor-1))));
145             Vy_ave_lim_vectors(i,j) = ...
146                 mean(mean(Vy_ave((iupper+(i-1)*ReduceFactor):(iupper+i*ReduceFactor-1),...
147                 (jlower+(j-1)*ReduceFactor):(jlower+j*ReduceFactor-1))));
148         end
149     end
```

```
150 end
151
152 %% Calculate the RMS field
153 RMSx(1:ny,1:nx) = 0;
154 RMSy(1:ny,1:nx) = 0;
155 RMSz(1:ny,1:nx) = 0;
156 for k = 1:N
157     for j = 1:nx
158         for i = 1:ny
159             if (Vx(i,j,k) ~= 0 && Vy(i,j,k) ~= 0 && Vz(i,j,k) ~= 0)
160                 RMSx(i,j) = RMSx(i,j) + (Vx(i,j,k) - Vx_ave(i,j))^2;
161                 RMSy(i,j) = RMSy(i,j) + (Vy(i,j,k) - Vy_ave(i,j))^2;
162                 RMSz(i,j) = RMSz(i,j) + (Vz(i,j,k) - Vz_ave(i,j))^2;
163             end
164         end
165     end
166 end
167 RMSx = sqrt((RMSx./(n-1)));
168 RMSy = sqrt((RMSy./(n-1)));
169 RMSz = sqrt((RMSz./(n-1)));
170
171 %% Calculate V
172 Vxy = sqrt( Vx_ave.^2 + Vy_ave.^2 );    % 2-component in-plane velocity ...
    magnitude
173 V = sqrt( Vx_ave.^2 + Vy_ave.^2 + Vz_ave.^2 );  % 3-component velocity magnitude
174
175 %% Calculate RMS
176 RMS = sqrt( RMSx.^2 + RMSy.^2 + RMSz.^2);
177
178 %% Calculate the precision uncertainty
179 Ux = 1.96*RMSx./sqrt(n);
180 Uy = 1.96*RMSy./sqrt(n);
181 Uz = 1.96*RMSz./sqrt(n);
182
183 U = sqrt( Ux.^2 + Uy.^2 + Uz.^2 );
184
185 %% Calculate the relative precision uncertainty
186 Vz_ave_mean = mean(mean(Vz_ave(iupper:ilower,jlower:jupper)));
187
188 Urel_x = Ux./Vz_ave_mean;
189 Urel_y = Uy./Vz_ave_mean;
190 Urel_z = Uz./Vz_ave_mean;
191
192 Urel = 100.*sqrt( Urel_x.^2 + Urel_y.^2 + Urel_z.^2 );
193
194 %% Calculate the Turbulence Kinetic Energy
195 TKE = 0.5*RMS.^2;
196
197 %% Calculate Turbulence Intensity
198 Uprime = sqrt(1./3.)*RMS;
199 TurbIntens = zeros(size(V,1),size(V,2));
200 for i=1:ny   % Calculate Turbulent Intensity, but don't divide by 0.
201     for j=1:nx
202         if V(i,j) >= 0.1    % Average isn't zero or near zero
203             TurbIntens(i,j) = 100.*Uprime(i,j)/V(i,j);
204         else   % Average is small, normalize by small velocity
```

```
205             TurbIntens(i,j) = 100.*Uprime(i,j)/0.1;
206         end
207     end
208 end
209
210 %% Calculate means of quantities of interest
211 Vxy_mean = mean(mean(Vxy(iupper:ilower,jlower:jupper)));
212 V_mean = mean(mean(V(iupper:ilower,jlower:jupper)));
213 RMS_mean = mean(mean(RMS(iupper:ilower,jlower:jupper)));
214 U_mean = mean(mean(U(iupper:ilower,jlower:jupper)));
215 Urel_mean = mean(mean(Urel(iupper:ilower,jlower:jupper)));
216 TurbIntens_mean = mean(mean(TurbIntens(iupper:ilower,jlower:jupper)));
217 TKE_mean = mean(mean(TKE(iupper:ilower,jlower:jupper)));
218
219 for k=1:N
220     Vy_mean = mean(mean(abs(Vy(iupper:ilower,jlower:jupper,k))));
221     Vz_mean(k) = mean(mean(Vz(iupper:ilower,jlower:jupper,k)));
222     VMI(k) = Vy_mean/Vz_mean(k);
223     CycleTime(k) = 2.*Depth/Vy_mean;
224 end
225
226 mean(VMI)
227 % std(VMI)
228 mean(CycleTime)
229 % std(CycleTime)
230
231 %% Plotting
232 if Plotting == 1    % Create new plots on average data
233
234     figure;
235     contourf(x,y,V,200,'edgecolor','none'); hold on;
236     if ReduceFactor == 1
237         quiver(x,y,Vx_ave,Vy_ave,2,'k');
238     elseif ReduceFactor > 1
239         quiver(x_lim_vectors,y_lim_vectors,10*Vx_ave_lim_vectors,10*Vy_ave_lim_vectors,0,'k');
240     end
241     axis equal; axis([xAxisShift,xupper-xlower+xAxisShift,...
242         yAxisShift,yupper-ylower+yAxisShift])
243     Vmax = max(max(V(iupper:ilower,jlower:jupper)));    % Max value in ...
        plotted domain
244     Vmin = min(min(V(iupper:ilower,jlower:jupper)));    % Min value in ...
        plotted domain
245     colormap(summer); h1 = colorbar('EastOutside');
246     set(get(h1,'ylabel'),'String','m/s','FontSize',13)
247     set(gca,'FontSize',13)
248     caxis([Vmin Vmax]); %shading interp
249     xlabel('x (cm)','FontSize',13); ylabel('y (cm)','FontSize',13)
250 %     title('Mean Velocity','FontSize',13)
251     set(gcf,'papersize',[8,PaperHeight]); ...
        set(gcf,'paperposition',[0,0,8,PaperHeight])
252
253     if TrimType == 0    % Use for PIV (not trimmed)
254         set(gca,'Position',...
255             get(gca,'OuterPosition') - get(gca,'TightInset') * ...
256             [-1 0 1 0; 0 -1 0 1; 0 0 50 0; 0 0 0 1])
257     elseif TrimType ==1 % Use for ADV (trimmed)
```

```
258         set(gca,'Position',...
259             get(gca,'OuterPosition') - get(gca,'TightInset') * ...
260             [-1.3 0 1 0; 0 -1 0 1; 0 0 30 0; 0 0 0 1])
261     end
262
263     if SavePlot == 1
264         saveas(gcf,[pwd,'plots\',project,'\',input,'_V',Format]);
265     end
266
267     %%%%%%%%%%%%%%%%%%%%%%%%%%%%%%%%%%%%%%%%%%%%%%%%
268     figure;
269     contourf(x,y,Vxy,200,'edgecolor','none'); hold on;
270     if ReduceFactor == 1
271         quiver(x,y,Vx_ave,Vy_ave,2,'k');
272     elseif ReduceFactor > 1
273         quiver(x_lim_vectors,y_lim_vectors,10*Vx_ave_lim_vectors,10*Vy_ave_lim_vectors,0,'k');
274     end
275     axis equal; axis([xAxisShift,xupper-xlower+xAxisShift,...
276         yAxisShift,yupper-ylower+yAxisShift])
277     Vxymax = max(max(Vxy(iupper:ilower,jlower:jupper)));    % Max value in ...
        plotted domain
278     Vxymin = min(min(Vxy(iupper:ilower,jlower:jupper)));    % Min value in ...
        plotted domain
279     % hcb=colorbar; set(hcb,'YTick',[0 .01 0.02 0.03 0.04])
280     colormap(summer); h0 = colorbar('EastOutside');
281     set(get(h0,'ylabel'),'String','m/s','FontSize',13)
282     set(gca,'FontSize',13)
283     caxis([Vxymin Vxymax]); %shading interp
284     xlabel('x (cm)','FontSize',13); ylabel('y (cm)','FontSize',13)
285     set(gcf,'papersize',[8,PaperHeight]); ...
            set(gcf,'paperposition',[0,0,8,PaperHeight])
286
287     if TrimType == 0    % Use for PIV (not trimmed)
288         set(gca,'Position',...
289             get(gca,'OuterPosition') - get(gca,'TightInset') * ...
290             [-1 0 1 0; 0 -1 0 1; 0 0 50 0; 0 0 0 1])
291     elseif TrimType ==1 % Use for ADV (trimmed)
292         set(gca,'Position',...
293             get(gca,'OuterPosition') - get(gca,'TightInset') * ...
294             [-1.3 0 1 0; 0 -1 0 1; 0 0 30 0; 0 0 0 1])
295     end
296
297 %     set(gcf,'color','g');
298 %     set(gcf, 'InvertHardCopy', 'off');
299
300     if SavePlot == 1
301         saveas(gcf,[pwd,'plots\',project,'\',input,'_Vxy',Format]);
302     end
303
304     %%%%%%%%%%%%%%%%%%%%%%%%%%%%%%%%%%%%%%%%%%%%%%%%
305     figure;
306     contourf(x,y,RMS,200,'edgecolor','none');
307     axis equal; axis([xAxisShift,xupper-xlower+xAxisShift,...
308         yAxisShift,yupper-ylower+yAxisShift])
309     RMSmax = max(max(RMS(iupper:ilower,jlower:jupper)));    % Max value in ...
        plotted domain
```

```
310     RMSmin = min(min(RMS(iupper:ilower,jlower:jupper)));    % Min value in ...
            plotted domain
311     colormap(summer); h2 = colorbar('EastOutside');
312     set(get(h2,'ylabel'),'String','m/s','FontSize',13);
313     set(gca,'FontSize',13)
314     caxis([RMSmin RMSmax]);
315     xlabel('x (cm)','FontSize',13); ylabel('y (cm)','FontSize',13)
316 %     title('Root Mean Square of Velocity','FontSize',13);
317     set(gcf,'papersize',[8,PaperHeight]); ...
            set(gcf,'paperposition',[0,0,8,PaperHeight])
318
319     if TrimType == 0    % Use for PIV (not trimmed)
320         set(gca,'Position',...
321             get(gca,'OuterPosition') - get(gca,'TightInset') * ...
322             [-1 0 1 0; 0 -1 0 1; 0 0 50 0; 0 0 0 1])
323     elseif TrimType ==1 % Use for ADV (trimmed)
324         set(gca,'Position',...
325             get(gca,'OuterPosition') - get(gca,'TightInset') * ...
326             [-1.3 0 1 0; 0 -1 0 1; 0 0 30 0; 0 0 0 1])
327     end
328
329     if SavePlot == 1
330         saveas(gcf,[pwd,'plots\',project,'\',input,'_RMS',Format]);
331     end
332
333     %%%%%%%%%%%%%%%%%%%%%%%%%%%%%%%%%%%%%%%%%%%%%%%
334     figure;
335     contourf(x,y,U,200,'edgecolor','none')
336     axis equal; axis([xAxisShift,xupper-xlower+xAxisShift,...
337         yAxisShift,yupper-ylower+yAxisShift])
338     Umax = max(max(U(iupper:ilower,jlower:jupper)));    % Max value in ...
            plotted domain
339     Umin = min(min(U(iupper:ilower,jlower:jupper)));    % Min value in ...
            plotted domain
340     % hcb=colorbar; set(hcb,'YTick',[0 .01 0.02 0.03 0.04])
341     colormap(summer); h0 = colorbar('EastOutside');
342     set(get(h0,'ylabel'),'String','m/s','FontSize',13)
343     set(gca,'FontSize',13)
344     caxis([Umin Umax]); %shading interp
345     xlabel('x (cm)','FontSize',13); ylabel('y (cm)','FontSize',13)
346 %     title('Precision Uncertainty');
347     set(gcf,'papersize',[8,PaperHeight]); ...
            set(gcf,'paperposition',[0,0,8,PaperHeight])
348
349     if TrimType == 0    % Use for PIV (not trimmed)
350         set(gca,'Position',...
351             get(gca,'OuterPosition') - get(gca,'TightInset') * ...
352             [-1 0 1 0; 0 -1 0 1; 0 0 50 0; 0 0 0 1])
353     elseif TrimType ==1 % Use for ADV (trimmed)
354         set(gca,'Position',...
355             get(gca,'OuterPosition') - get(gca,'TightInset') * ...
356             [-1.3 0 1 0; 0 -1 0 1; 0 0 30 0; 0 0 0 1])
357     end
358
359     if SavePlot == 1
360         saveas(gcf,[pwd,'plots\',project,'\',input,'_U',Format]);
```

```
361     end
362
363     %%%%%%%%%%%%%%%%%%%%%%%%%%%%%%%%%%%%%%%%%%%%%%%%
364     figure;
365     contourf(x,y,Urel,200,'edgecolor','none')
366     axis equal; axis([xAxisShift,xupper-xlower+xAxisShift,...
367         yAxisShift,yupper-ylower+yAxisShift])
368     Urel_max = max(max(Urel(iupper:ilower,jlower:jupper)));    % Max value ...
        in plotted domain
369     Urel_min = min(min(Urel(iupper:ilower,jlower:jupper)));    % Min value ...
        in plotted domain
370     colormap(summer); h0 = colorbar('EastOutside');
371     set(get(h0,'ylabel'),'String','%','FontSize',13)
372     set(gca,'FontSize',13)
373     caxis([Urel_min Urel_max]); %shading interp
374     xlabel('x (cm)','FontSize',13); ylabel('y (cm)','FontSize',13)
375 %     title('Relative Precision Uncertainty');
376     set(gcf,'papersize',[8,PaperHeight]); ...
        set(gcf,'paperposition',[0,0,8,PaperHeight])
377
378     if TrimType == 0    % Use for PIV (not trimmed)
379         set(gca,'Position',...
380             get(gca,'OuterPosition') - get(gca,'TightInset') * ...
381             [-1 0 1 0; 0 -1 0 1; 0 0 50 0; 0 0 0 1])
382     elseif TrimType ==1 % Use for ADV (trimmed)
383         set(gca,'Position',...
384             get(gca,'OuterPosition') - get(gca,'TightInset') * ...
385             [-1.3 0 1 0; 0 -1 0 1; 0 0 30 0; 0 0 0 1])
386     end
387
388     if SavePlot == 1
389         saveas(gcf,[pwd,'plots\',project,'\',input,'_Urel',Format]);
390     end
391
392     %%%%%%%%%%%%%%%%%%%%%%%%%%%%%%%%%%%%%%%%%%%%%%%%
393     figure;
394     contourf(x,y,TKE,200,'edgecolor','none')
395     axis equal; axis([xAxisShift,xupper-xlower+xAxisShift,...
396         yAxisShift,yupper-ylower+yAxisShift])
397     TKEmax = max(max(TKE(iupper:ilower,jlower:jupper)));    % Max value in ...
        plotted domain
398     TKEmin = min(min(TKE(iupper:ilower,jlower:jupper)));    % Min value in ...
        plotted domain
399     colormap(summer); h4 = colorbar('EastOutside');
400     set(get(h4,'ylabel'),'String','m^2/s^2','FontSize',13)
401     set(gca,'FontSize',13)
402     caxis([TKEmin TKEmax])
403     xlabel('x (cm)','FontSize',13); ylabel('y (cm)','FontSize',13)
404 %     title('Turbulence Kinetic Energy','FontSize',13)
405     set(gcf,'papersize',[8,PaperHeight]); ...
        set(gcf,'paperposition',[0,0,8,PaperHeight])
406
407     if TrimType == 0    % Use for PIV (not trimmed)
408         set(gca,'Position',...
409             get(gca,'OuterPosition') - get(gca,'TightInset') * ...
410             [-1 0 1 0; 0 -1 0 1; 0 0 50 0; 0 0 0 1])
```

```
411     elseif TrimType ==1 % Use for ADV (trimmed)
412         set(gca,'Position',...
413             get(gca,'OuterPosition') - get(gca,'TightInset') * ...
414             [-1.3 0 1 0; 0 -1 0 1; 0 0 30 0; 0 0 0 1])
415     end
416
417     if SavePlot == 1
418         saveas(gcf,[pwd,'plots\',project,'\',input,'_TKE',Format]);
419     end
420
421     %%%%%%%%%%%%%%%%%%%%%%%%%%%%%%%%%%%%%%%%%%%%%%%
422     figure;
423     contourf(x,y,TurbIntens,200,'edgecolor','none')
424     axis equal; axis([xAxisShift,xupper-xlower+xAxisShift,...
425         yAxisShift,yupper-ylower+yAxisShift])
426     TurbIntensmax = max(max(TurbIntens(iupper:ilower,jlower:jupper)));    % ...
            Max value in plotted domain
427     TurbIntensmin = min(min(TurbIntens(iupper:ilower,jlower:jupper)));    % ...
            Min value in plotted domain
428     colormap(summer); h3 = colorbar('EastOutside');
429     set(get(h3,'ylabel'),'String','%','FontSize',13)
430     set(gca,'FontSize',13)
431     caxis([TurbIntensmin TurbIntensmax])
432     xlabel('x (cm)','FontSize',13); ylabel('y (cm)','FontSize',13)
433 %     title('Turbulence Intensity','FontSize',13)
434     set(gcf,'papersize',[8,PaperHeight]); ...
            set(gcf,'paperposition',[0,0,8,PaperHeight])
435
436     if TrimType == 0    % Use for PIV (not trimmed)
437         set(gca,'Position',...
438             get(gca,'OuterPosition') - get(gca,'TightInset') * ...
439             [-1 0 1 0; 0 -1 0 1; 0 0 50 0; 0 0 0 1])
440     elseif TrimType ==1 % Use for ADV (trimmed)
441         set(gca,'Position',...
442             get(gca,'OuterPosition') - get(gca,'TightInset') * ...
443             [-1.3 0 1 0; 0 -1 0 1; 0 0 30 0; 0 0 0 1])
444     end
445
446     if SavePlot == 1
447         saveas(gcf,[pwd,'plots\',project,'\',input,'_TurbIntens',Format]);
448     end
449
450 end
451
452 toc
```

Appendix C

Matlab Function to Trim Masked Area

```
function [imin,imax,jmin,jmax] = TrimToMask( U )

% This subroutine takes any 2D velocity field U and finds the i and j
  % indeces of the last zeros around the perimeter of the masked area.
  %     Remember:   the i axis is aligned with x increasing to right
  %                 the j axis is reverse with y increasing to bottom

% Determine left-hand mask boundary
jmin = zeros(1,size(U,1));
for i=1:size(U,1)    % Run through rows
    trigger = 0;     % Reset trigger for every new row
    for j=1:size(U,2)   % Run through columns from left to right
        if trigger == 0 % The first non-zero hasn't been found
            if U(i,j) == 0.
                jmin(i) = j;    % x-index of last 0.
            else
                trigger = 1;    % set trigger for first non-zero
            end
        end
    end
end

% Determine right-hand mask boundary
jmax = ones(1,size(U,1))*size(U,1);
for i=1:size(U,1)    % Run through rows
    trigger = 0;     % Reset trigger for every new row
    for j=size(U,2):-1:1   % Run through columns from right to left
        if trigger == 0 % The first non-zero hasn't been found
            if U(i,j) == 0.
                jmax(i) = j;  % x-index of last 0.
            else
                trigger = 1;    % set trigger for first non-zero
            end
        end
    end
end

% Determine top mask boundary
imax = zeros(1,size(U,2));
for j=1:size(U,2)    % Run through columns
    trigger = 0;     % Reset trigger for every new column
    for i=1:size(U,1)   % Run through rows from top to bottom
        if trigger == 0 % The first non-zero hasn't been found
            if U(i,j) == 0.
```

```
45                  imax(j) = i;  % y-index of last 0.
46              else
47                  trigger = 1;    % set trigger for first non-zero
48              end
49          end
50      end
51  end
52
53  % Determine bottom mask boundary
54  imin = zeros(1,size(U,2));
55  for j=1:size(U,2)   % Run through columns
56      trigger = 0;    % Reset trigger for every new column
57      for i=size(U,1):-1:1   % Run through rows from bottom to top
58          if trigger == 0 % The first non-zero hasn't been found
59              if U(i,j) == 0.
60                  imin(j) = i;  % y-index of last 0.
61              else
62                  trigger = 1;    % set trigger for first non-zero
63              end
64          end
65      end
66  end
67
68  imin = max(imin);
69  imax = min(imax);
70  jmin = min(jmin);
71  jmax = max(jmax);
```

Appendix D

Optimization Study on Delta Wing Spacing

Optimization Study Performed on Delta Wing Spacing

Determine the value of algae biomass (50% is oil, 50% can be used for aquaculture)

$\rho_{lipid} := 950 \frac{kg}{m^3}$ $\quad Value_{Oil} := \frac{¤.\frac{2}{gal}}{\rho_{lipid}} = 0.556 \frac{¤}{kg}$ $\quad Value_{aqua\_cult} := ¤.\frac{1.50}{kg}$

$Value := Value_{Oil} + Value_{aqua\_cult} = 2.056 \frac{¤}{kg}$ Value of algae biomass in dollars

Consider a raceway $\quad Length := 82m \quad Width := 12m \quad Area := Length \cdot Width = 984\,m^2$

Income potential

$G_0 := 15 \frac{gm}{m^2 \cdot day}$ A typical growth rate for raceways

$VMI_0 := 0.1$ The measured baseline VMI in raceway

$n := 0.322$ This gives the relationship that doubling the VMI gives 25% better growth

$C_G := \frac{G_0}{VMI_0^{\,n}} = 31.484 \cdot \frac{gm}{m^2 \cdot day}$ Growth Constant

$\Delta VMI(z) := \frac{0.0215}{m^2} z^2 - \frac{0.1476}{m} z + 0.2676$ Curve fit from experimental data for VMI increase over case without Delta Wing (DW)

Average VMI as a function of DW spacing

$\Delta VMI_{ave}(\Delta z) := \frac{1}{\Delta z} \cdot \int_0^{\Delta z} \Delta VMI(\Delta z)\, dz \rightarrow \frac{0.0001 \cdot \left(2676.0 \cdot m^2 + 215.0 \cdot \Delta z^2 + -1476.0 \cdot m \cdot \Delta z\right)}{m^2}$

$Growth(\Delta z) := C_G \cdot \Delta VMI_{ave}(\Delta z)^n$ Growth model as a function of VMI

$Revenue(\Delta z) := Value \cdot Growth(\Delta z) \cdot Area$

Cost for each Delta Wing

$N_{streamwise}(\Delta z) := \frac{Length}{\Delta z}$ Number of DWs

$N_{across} := 24$ There will be 24 DWs across, spaced every 0.5m.

$Cost_{Power}(\Delta z) := 2W \cdot N_{across} \cdot \left(\frac{¤ \cdot 0.08}{kW \cdot hr}\right) \cdot N_{streamwise}(\Delta z)$ Each DW will likely place 2W load on paddle-wheel

$Cost_{Capital}(\Delta z) := ¤ \cdot 2.857 \cdot N_{across} \cdot \frac{N_{streamwise}(\Delta z)}{yr}$ This is considering each DW and mounting hardware costs $20 and will last 7 years.

$Cost(\Delta z) := Cost_{Power}(\Delta z) + Cost_{Capital}(\Delta z)$

Revenue Optimization

$Profit(\Delta z) := Revenue(\Delta z) - Cost(\Delta z)$

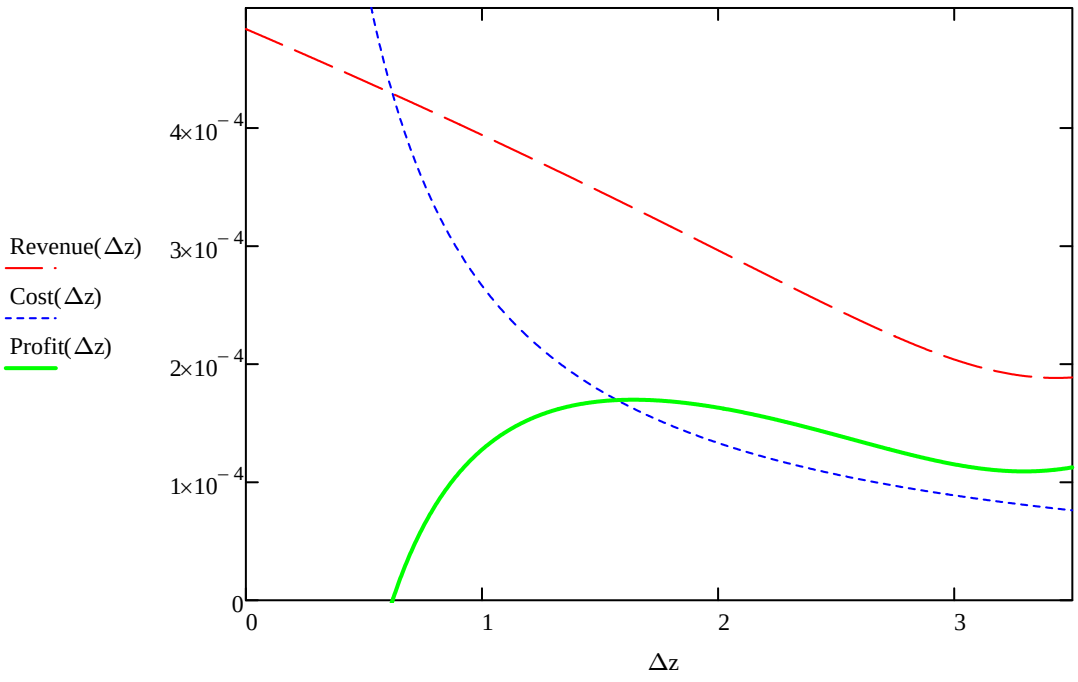

Solve for optimal spacing

$\Delta z := 1m$ Given $\Delta z \geq 0m$

$OptimalSpacing := Maximize(Profit, \Delta z) = 64.609 \cdot in$ This is the optimal DW spacing for revenue.

$Profit(OptimalSpacing) = 5.342 \times 10^{3} \cdot \frac{¤}{yr}$ This is an approximate gain in revenue from using the DW. It is a gain because the ΔVMI curve fit was the VMI from using the DW minus the VMI without any DW.

What is the increase in profit?

$\Delta VMI_{ave}(OptimalSpacing) = 0.083$ This much is added to the baseline.

$VMI_0 = 0.1$ is the baseline VMI for raceways

We have nearly doubled the mixing, so the growth has increased by nearly 25% and so should the profit.

Appendix E

Comparison of PIV and ADV Data

This appendix contains the PIV and ADV plots for a study performed near the center of the raceway with eight inches of water. Cases without the DW and with the DW at 30° angle of attack are given. Quantities that are represented include velocity, in-plane velocity, standard deviation, turbulence kinetic energy, and turbulence intensity. The PIV data were trimmed to match the ADV domain for direct comparison.

E.1 Results without Delta Wing

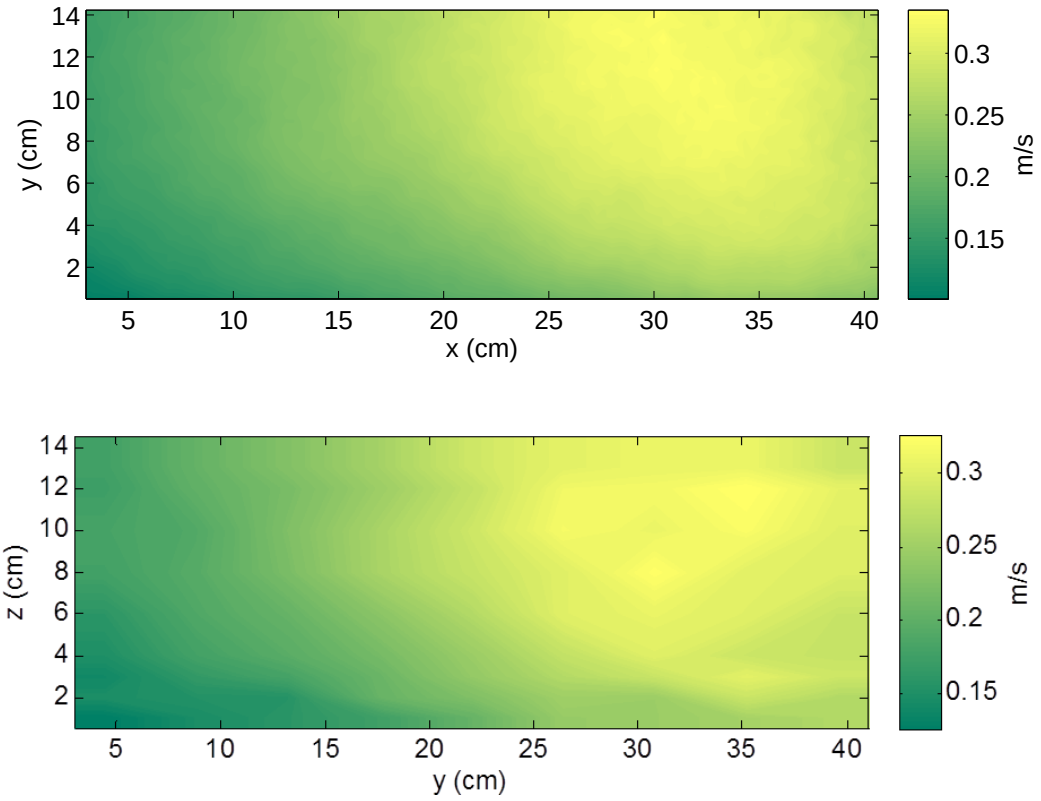

Fig. E.1: Contour plots of velocity magnitude with PIV on top and ADV on bottom without Delta Wing

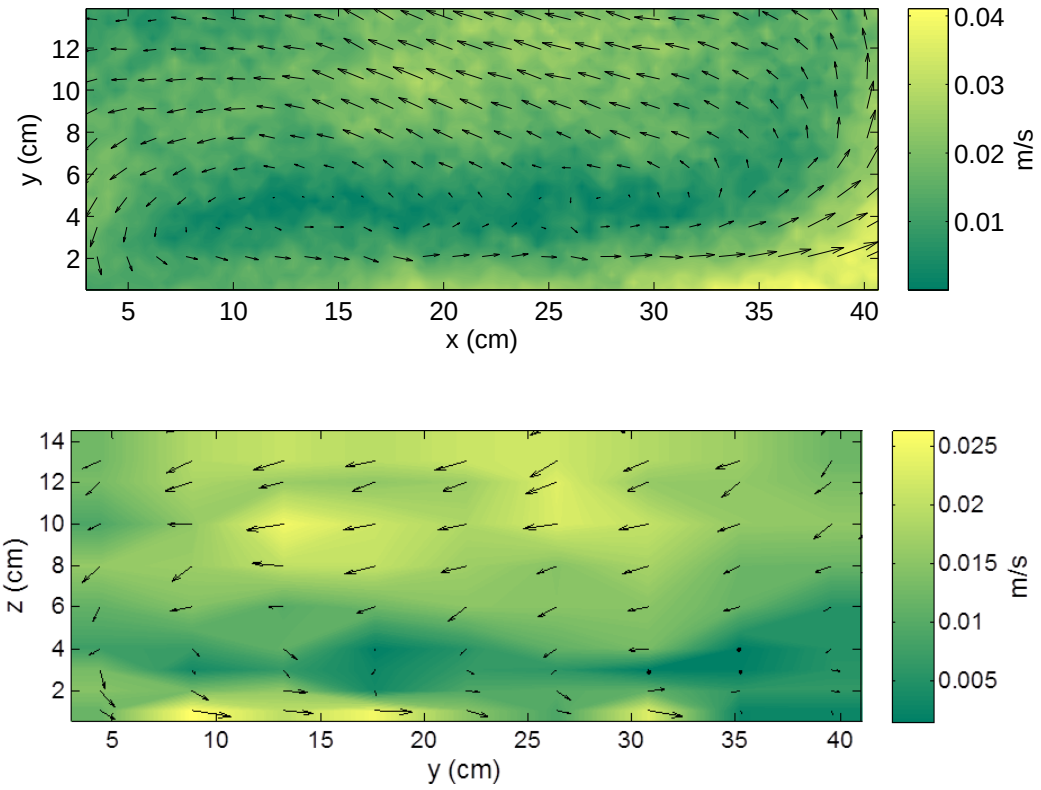

Fig. E.2: Contour and vector plots of in-plane velocity magnitude with PIV on top and ADV on bottom without Delta Wing

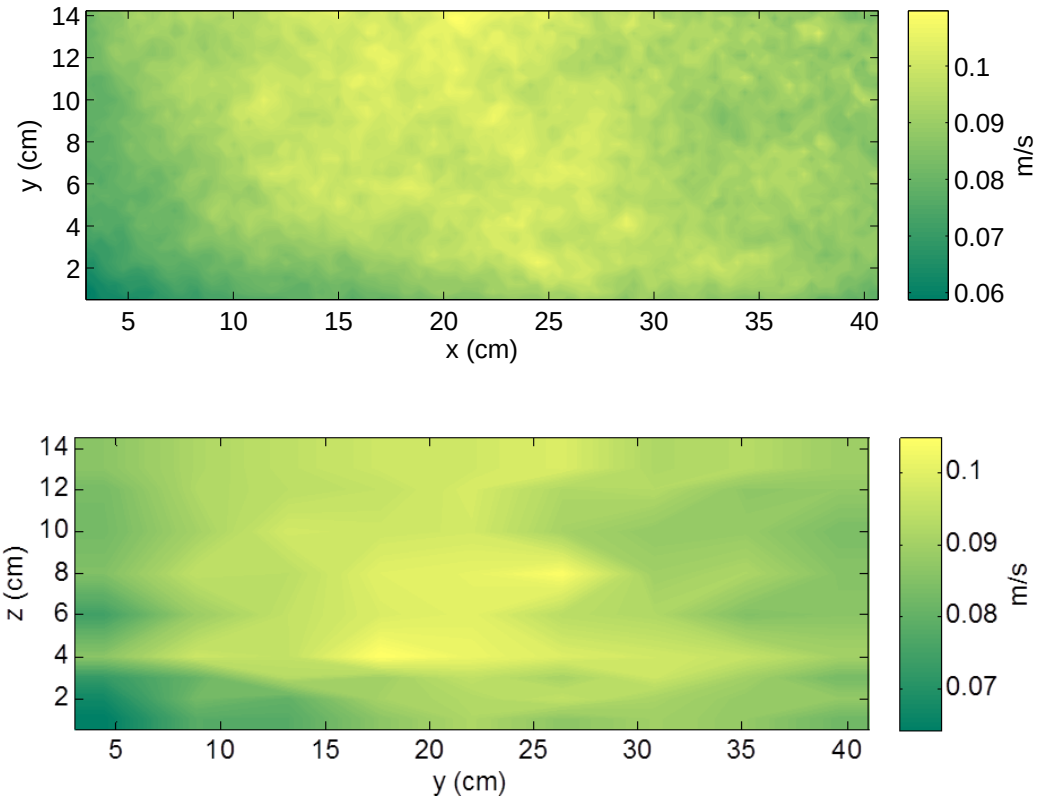

Fig. E.3: Contour plots of velocity standard deviation of 200 instantaneous velocity fields. The PIV result is on top and ADV on bottom; without Delta Wing.

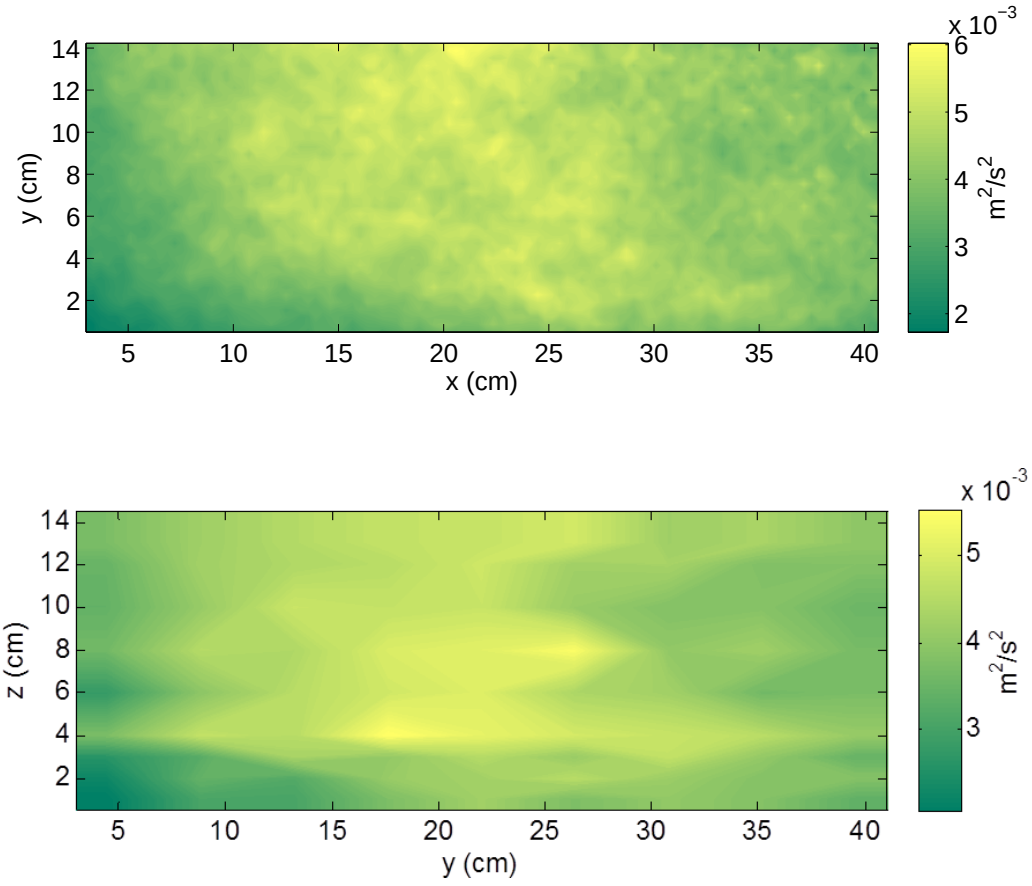

Fig. E.4: Contour plots of turbulence kinetic energy with PIV on top and ADV on bottom without Delta Wing

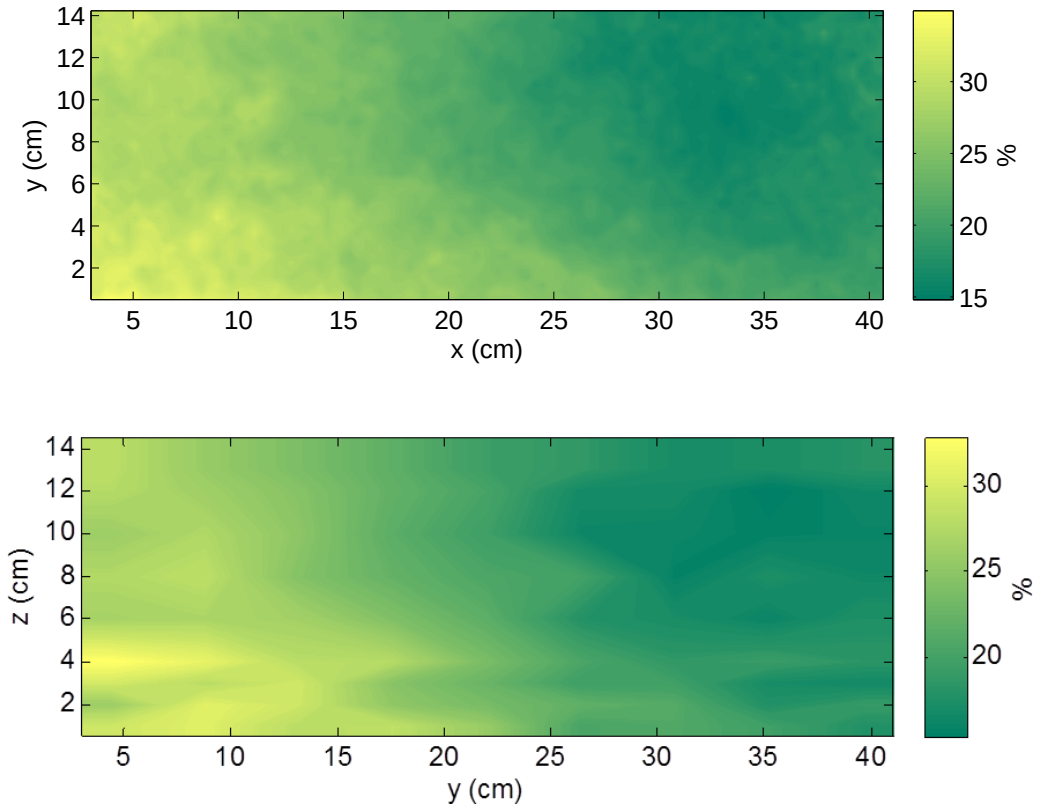

Fig. E.5: Contour plots of turbulence intensity with PIV on top and ADV on bottom without Delta Wing

E.2 Results with Delta Wing

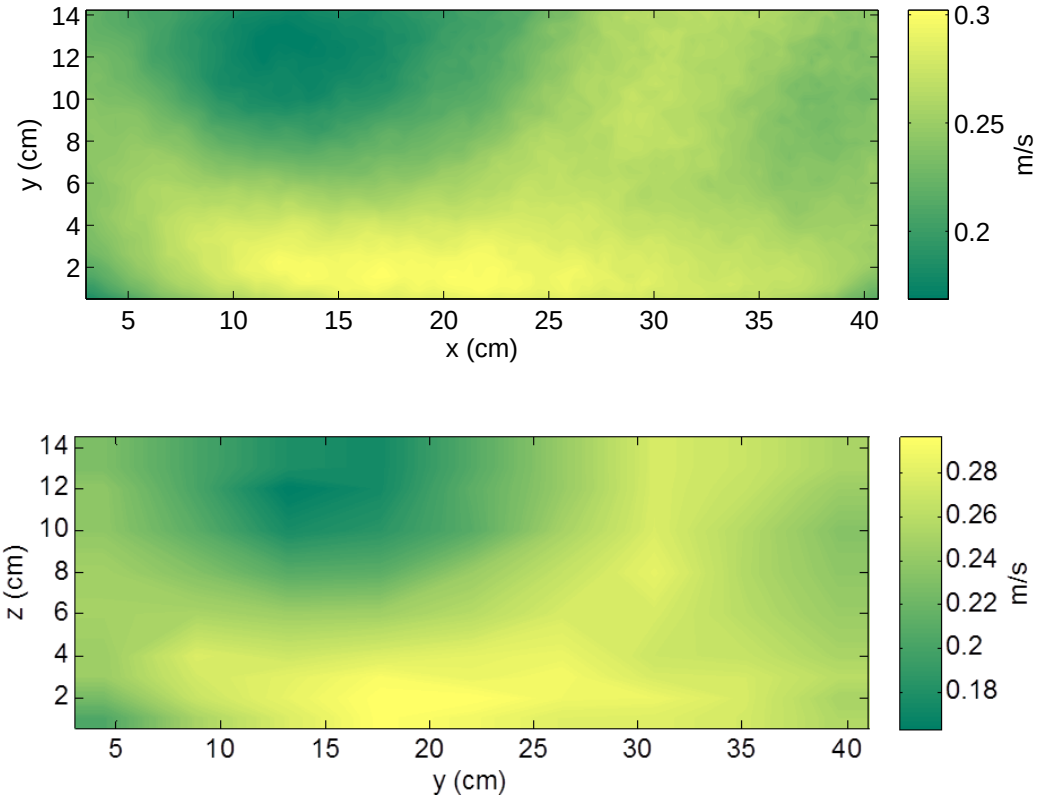

Fig. E.6: Contour plots of velocity magnitude with PIV on top and ADV on bottom with Delta Wing

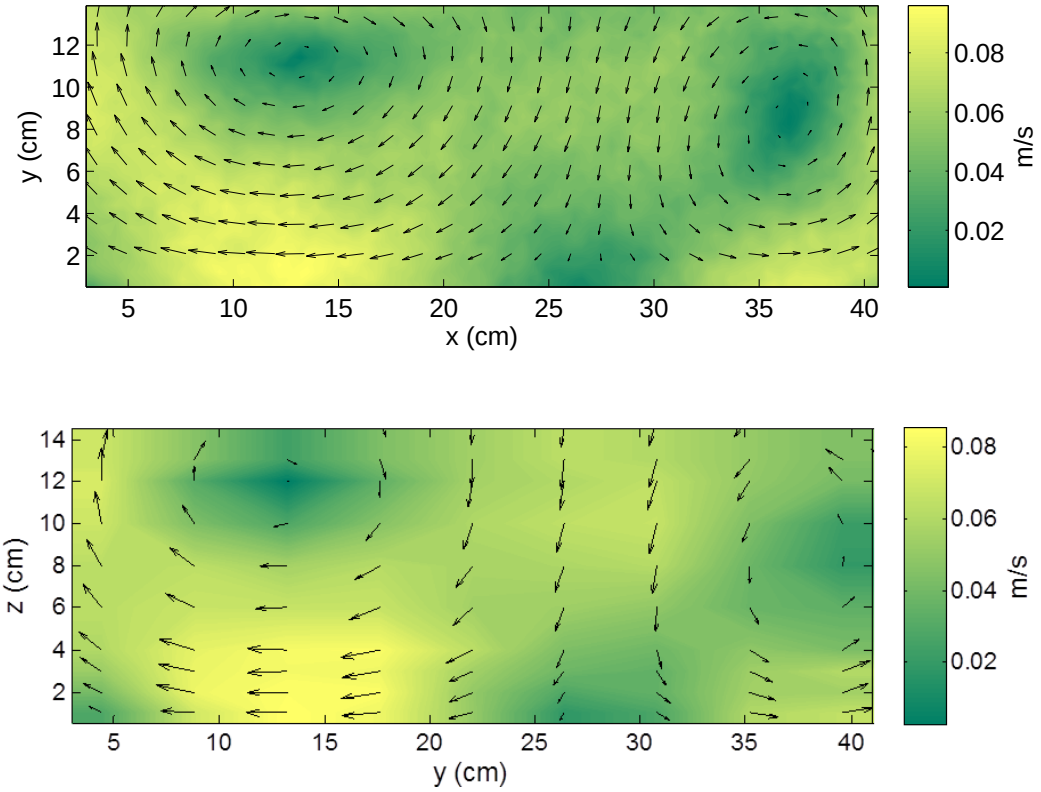

Fig. E.7: Contour and vector plots of in-plane velocity magnitude with PIV on top and ADV on bottom with Delta Wing

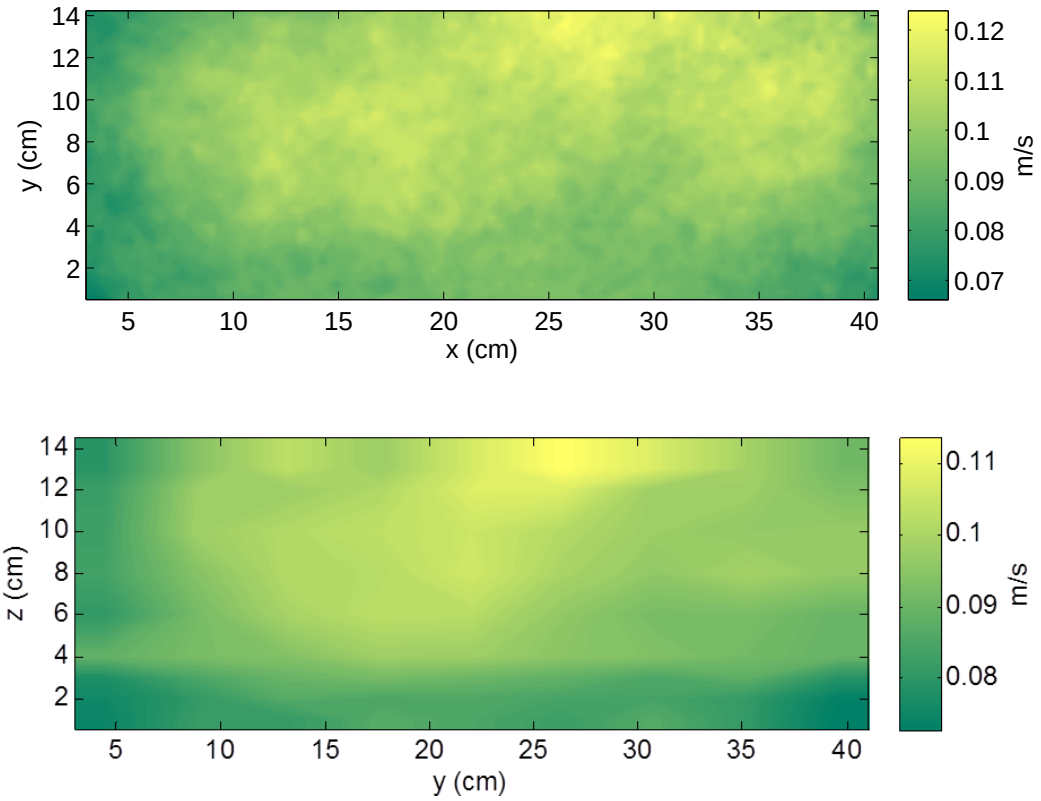

Fig. E.8: Contour plots of velocity standard deviation of 200 instantaneous velocity fields. The PIV result is on top and ADV on bottom; with Delta Wing.

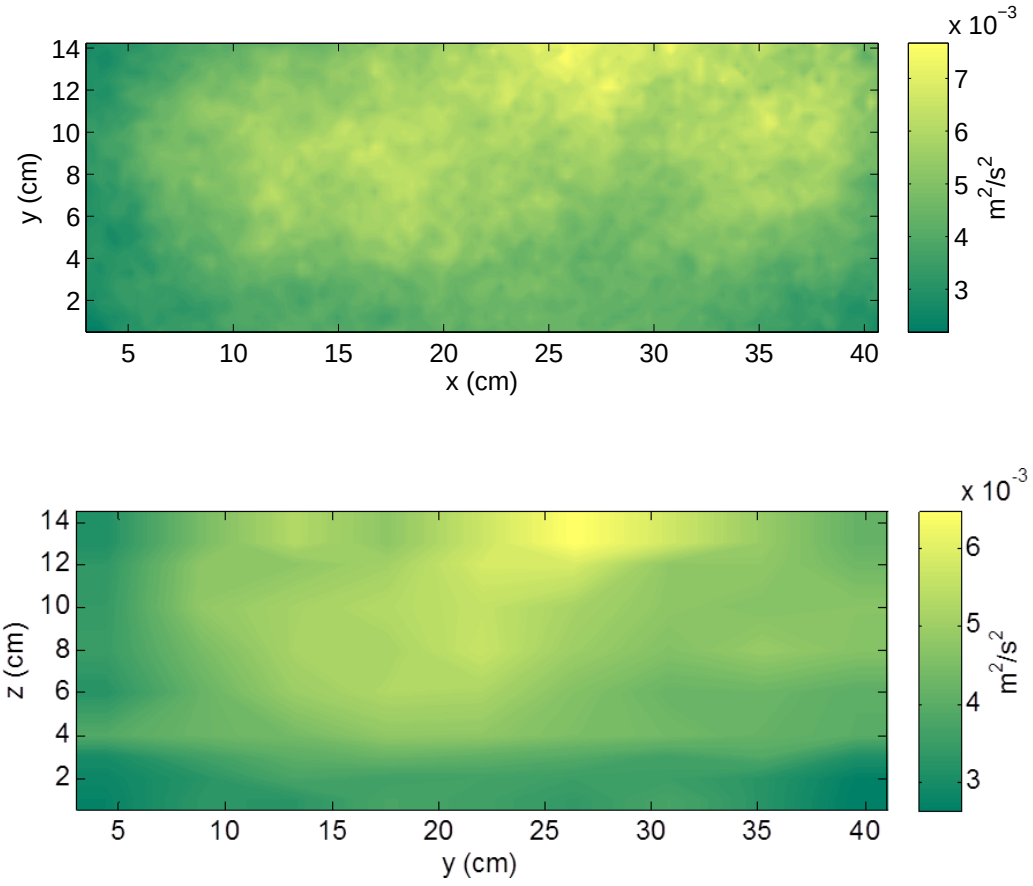

Fig. E.9: Contour plots of turbulence kinetic energy with PIV on top and ADV on bottom with Delta Wing

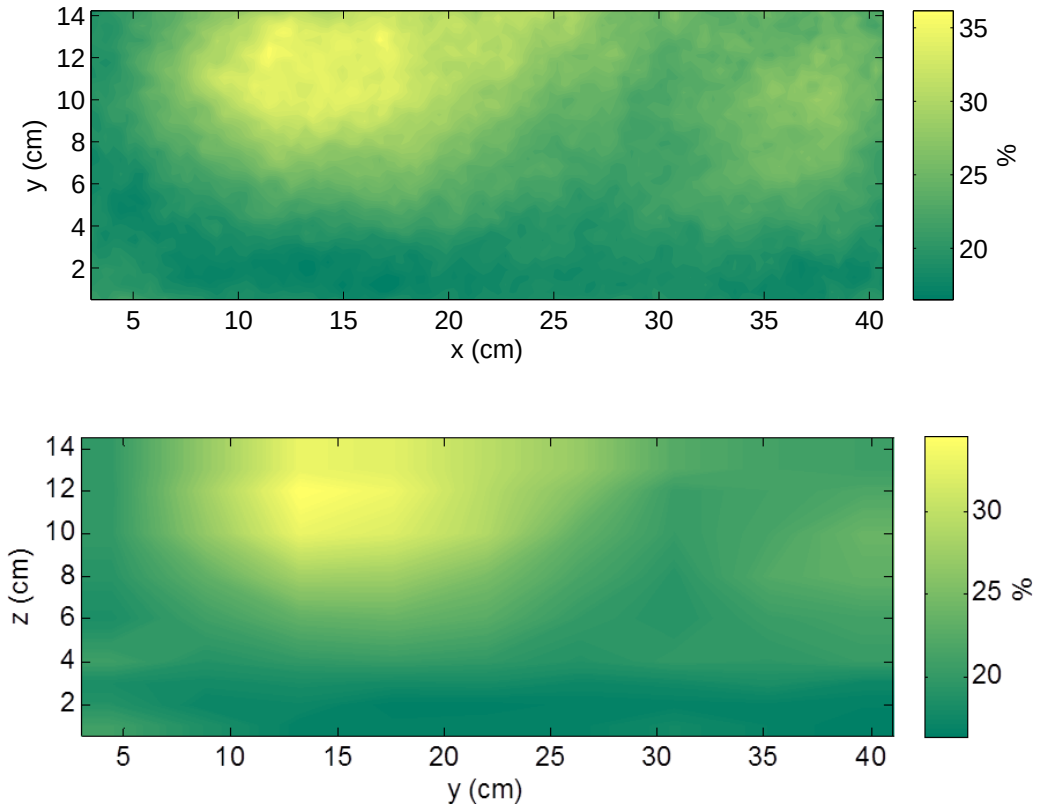

Fig. E.10: Contour plots of turbulence intensity with PIV on top and ADV on bottom with Delta Wing

Appendix F

Permission to Use Fig. 1 from Chisti [2]

ELSEVIER LICENSE
TERMS AND CONDITIONS

Jul 25, 2012

This is a License Agreement between Blake Lance ("You") and Elsevier ("Elsevier") provided by Copyright Clearance Center ("CCC"). The license consists of your order details, the terms and conditions provided by Elsevier, and the payment terms and conditions.

All payments must be made in full to CCC. For payment instructions, please see information listed at the bottom of this form.

Supplier	Elsevier Limited The Boulevard,Langford Lane Kidlington,Oxford,OX5 1GB,UK
Registered Company Number	1982084
Customer name	Blake Lance
Customer address	29 Aggie Vlg Apt G Logan, UT 84341
License number	2956041051529
License date	Jul 25, 2012
Licensed content publisher	Elsevier
Licensed content publication	Biotechnology Advances
Licensed content title	Biodiesel from microalgae
Licensed content author	Yusuf Chisti
Licensed content date	May–June 2007
Licensed content volume number	25
Licensed content issue number	3
Number of pages	13
Start Page	294
End Page	306
Type of Use	reuse in a thesis/dissertation
Portion	figures/tables/illustrations
Number of figures/tables /illustrations	1
Format	both print and electronic
Are you the author of this Elsevier article?	No
Will you be translating?	No
Order reference number	

Title of your thesis/dissertation	Using Stereo Particle Image Velocimetry to Quantify and Optimize Mixing in an Algae Raceway Using Delta Wings
Expected completion date	Aug 2012
Estimated size (number of pages)	60
Elsevier VAT number	GB 494 6272 12
Permissions price	0.00 USD
VAT/Local Sales Tax	0.0 USD / 0.0 GBP
Total	0.00 USD
Terms and Conditions	

INTRODUCTION

1. The publisher for this copyrighted material is Elsevier. By clicking "accept" in connection with completing this licensing transaction, you agree that the following terms and conditions apply to this transaction (along with the Billing and Payment terms and conditions established by Copyright Clearance Center, Inc. ("CCC"), at the time that you opened your Rightslink account and that are available at any time at http://myaccount.copyright.com).

GENERAL TERMS

2. Elsevier hereby grants you permission to reproduce the aforementioned material subject to the terms and conditions indicated.

3. Acknowledgement: If any part of the material to be used (for example, figures) has appeared in our publication with credit or acknowledgement to another source, permission must also be sought from that source. If such permission is not obtained then that material may not be included in your publication/copies. Suitable acknowledgement to the source must be made, either as a footnote or in a reference list at the end of your publication, as follows:

“Reprinted from Publication title, Vol /edition number, Author(s), Title of article / title of chapter, Pages No., Copyright (Year), with permission from Elsevier [OR APPLICABLE SOCIETY COPYRIGHT OWNER].” Also Lancet special credit - “Reprinted from The Lancet, Vol. number, Author(s), Title of article, Pages No., Copyright (Year), with permission from Elsevier.”

4. Reproduction of this material is confined to the purpose and/or media for which permission is hereby given.

5. Altering/Modifying Material: Not Permitted. However figures and illustrations may be altered/adapted minimally to serve your work. Any other abbreviations, additions, deletions and/or any other alterations shall be made only with prior written authorization of Elsevier Ltd. (Please contact Elsevier at permissions@elsevier.com)

6. If the permission fee for the requested use of our material is waived in this instance, please be advised that your future requests for Elsevier materials may attract a fee.

Appendix G

Permission to Use Fig. 5 from Singh and Sharma [6]

ELSEVIER LICENSE
TERMS AND CONDITIONS

Sep 07, 2012

This is a License Agreement between Blake Lance ("You") and Elsevier ("Elsevier") provided by Copyright Clearance Center ("CCC"). The license consists of your order details, the terms and conditions provided by Elsevier, and the payment terms and conditions.

All payments must be made in full to CCC. For payment instructions, please see information listed at the bottom of this form.

Supplier	Elsevier Limited The Boulevard,Langford Lane Kidlington,Oxford,OX5 1GB,UK
Registered Company Number	1982084
Customer name	Blake Lance
Customer address	29 Aggie Vlg Apt G Logan, UT 84341
License number	2983810096870
License date	Sep 07, 2012
Licensed content publisher	Elsevier
Licensed content publication	Renewable and Sustainable Energy Reviews
Licensed content title	Development of suitable photobioreactor for algae production – A review
Licensed content author	R.N. Singh,Shaishav Sharma
Licensed content date	May 2012
Licensed content volume number	16
Licensed content issue number	4
Number of pages	7
Start Page	2347
End Page	2353
Type of Use	reuse in a thesis/dissertation
Intended publisher of new work	other
Portion	figures/tables/illustrations
Number of figures/tables /illustrations	1
Format	both print and electronic
Are you the author of this Elsevier article?	No
Will you be translating?	No

Order reference number	
Title of your thesis/dissertation	Using Stereo Particle Image Velocimetry to Quantify and Optimize Mixing in an Algae Raceway Using Delta Wings
Expected completion date	Sep 2012
Estimated size (number of pages)	115
Elsevier VAT number	GB 494 6272 12
Permissions price	0.00 USD
VAT/Local Sales Tax	0.0 USD / 0.0 GBP
Total	0.00 USD
Terms and Conditions	

INTRODUCTION

1. The publisher for this copyrighted material is Elsevier. By clicking "accept" in connection with completing this licensing transaction, you agree that the following terms and conditions apply to this transaction (along with the Billing and Payment terms and conditions established by Copyright Clearance Center, Inc. ("CCC"), at the time that you opened your Rightslink account and that are available at any time at http://myaccount.copyright.com).

GENERAL TERMS

2. Elsevier hereby grants you permission to reproduce the aforementioned material subject to the terms and conditions indicated.

3. Acknowledgement: If any part of the material to be used (for example, figures) has appeared in our publication with credit or acknowledgement to another source, permission must also be sought from that source. If such permission is not obtained then that material may not be included in your publication/copies. Suitable acknowledgement to the source must be made, either as a footnote or in a reference list at the end of your publication, as follows:

“Reprinted from Publication title, Vol /edition number, Author(s), Title of article / title of chapter, Pages No., Copyright (Year), with permission from Elsevier [OR APPLICABLE SOCIETY COPYRIGHT OWNER].” Also Lancet special credit - “Reprinted from The Lancet, Vol. number, Author(s), Title of article, Pages No., Copyright (Year), with permission from Elsevier.”

4. Reproduction of this material is confined to the purpose and/or media for which permission is hereby given.

5. Altering/Modifying Material: Not Permitted. However figures and illustrations may be altered/adapted minimally to serve your work. Any other abbreviations, additions, deletions and/or any other alterations shall be made only with prior written authorization of Elsevier Ltd. (Please contact Elsevier at permissions@elsevier.com)

Appendix H

Permission to Use Fig. 7 from Laws *et al.* [13]

JOHN WILEY AND SONS LICENSE TERMS AND CONDITIONS

Jul 25, 2012

This is a License Agreement between Blake Lance ("You") and John Wiley and Sons ("John Wiley and Sons") provided by Copyright Clearance Center ("CCC"). The license consists of your order details, the terms and conditions provided by John Wiley and Sons, and the payment terms and conditions.

All payments must be made in full to CCC. For payment instructions, please see information listed at the bottom of this form.

License Number	2956030072966
License date	Jul 25, 2012
Licensed content publisher	John Wiley and Sons
Licensed content publication	Biotechnology & Bioengineering
Licensed content title	A simple algal production system designed to utilize the flashing light effect
Licensed content author	E. A. Laws,K. L. Terry,J. Wickman,M. S. Chalup
Licensed content date	Feb 18, 2004
Start page	2319
End page	2335
Type of use	Dissertation/Thesis
Requestor type	University/Academic
Format	Print and electronic
Portion	Figure/table
Number of figures/tables	1
Number of extracts	
Original Wiley figure/table number(s)	Figure 7
Will you be translating?	No
Order reference number	
Total	0.00 USD
Terms and Conditions	

TERMS AND CONDITIONS

This copyrighted material is owned by or exclusively licensed to John Wiley & Sons, Inc. or one of its group companies (each a "Wiley Company") or a society for whom a Wiley Company has exclusive publishing rights in relation to a particular journal (collectively WILEY"). By clicking "accept" in connection with completing this licensing transaction, you agree that the following terms and conditions apply to this transaction (along with the billing and payment terms and conditions established by the Copyright Clearance Center Inc., ("CCC's Billing and Payment terms and conditions"), at the time that you opened your Rightslink account (these are available at any time at http://myaccount.copyright.com)

Appendix I

Permission to Use Animation from LaVision Website [18]

aggiemail **Blake Lance <b.lance@aggiemail.usu.edu>**

Permission to Use Animation

2 messages

Blake Lance <b.lance@aggiemail.usu.edu> Fri, Sep 7, 2012 at 3:03 PM
To: Steve Anderson <sanderson@lavisioninc.com>

Steve,

Can you give permission to use the attached animation from LaVision's website in my thesis? It would be included as seen with the LaVision logo intact and will not be used for commercial purposes. Thanks for any help you can give.

--

Blake Lance
Graduate Research Assistant
Utah State University
Mechanical & Aerospace Engineering
4130 Old Main Hill
Logan UT 84322
435-797-8147

PIVAnimation.mp4
531K

Steve Anderson <sanderson@lavisioninc.com> Mon, Sep 10, 2012 at 4:44 AM
To: Blake Lance <b.lance@aggiemail.usu.edu>

Blake,

No problem – go ahead and use it.

Thanks for asking.

Kind regards,

Steve

From: Blake Lance [mailto:b.lance@aggiemail.usu.edu]
Sent: Friday, September 07, 2012 4:04 PM
To: Steve Anderson
Subject: Permission to Use Animation